

AD _____

Award Number: DAMD17-98-1-8141

TITLE: Quantitative Three-Dimensional Ultrasonic Mammography

PRINCIPAL INVESTIGATOR: T. Douglas Mast, Ph.D.

CONTRACTING ORGANIZATION: The Pennsylvania State University
State College, Pennsylvania
16804-0030

REPORT DATE: July 2000

TYPE OF REPORT: Annual

PREPARED FOR: U.S. Army Medical Research and Materiel Command
Fort Detrick, Maryland 21702-5012

DISTRIBUTION STATEMENT: Approved for Public Release;
Distribution Unlimited

The views, opinions and/or findings contained in this report are those of the author(s) and should not be construed as an official Department of the Army position, policy or decision unless so designated by other documentation.

20010509 039

REPORT DOCUMENTATION PAGEForm Approved
OMB No. 074-0188

Public reporting burden for this collection of information is estimated to average 1 hour per response, including the time for reviewing instructions, searching existing data sources, gathering and maintaining the data needed, and completing and reviewing this collection of information. Send comments regarding this burden estimate or any other aspect of this collection of information, including suggestions for reducing this burden to Washington Headquarters Services, Directorate for Information Operations and Reports, 1215 Jefferson Davis Highway, Suite 1204, Arlington, VA 22202-4302, and to the Office of Management and Budget, Paperwork Reduction Project (0704-0188), Washington, DC 20503

1. AGENCY USE ONLY (Leave blank)		2. REPORT DATE July 2000	3. REPORT TYPE AND DATES COVERED Annual (1 Jul 99 - 30 Jun 00)	
4. TITLE AND SUBTITLE Quantitative Three-Dimensional Ultrasonic Mammography			5. FUNDING NUMBERS DAMD17-98-1-8141	
6. AUTHOR(S) T. Douglas Mast, Ph.D.				
7. PERFORMING ORGANIZATION NAME(S) AND ADDRESS(ES) The Pennsylvania State University Applied Research Laboratory State College, Pennsylvania 16804-0030 E-MAIL: mast@sabine.acs.psu.edu			8. PERFORMING ORGANIZATION REPORT NUMBER	
9. SPONSORING / MONITORING AGENCY NAME(S) AND ADDRESS(ES) U.S. Army Medical Research and Materiel Command Fort Detrick, Maryland 21702-5012			10. SPONSORING / MONITORING AGENCY REPORT NUMBER	
11. SUPPLEMENTARY NOTES Report contains color photos				
12a. DISTRIBUTION / AVAILABILITY STATEMENT Approved for public release; distribution unlimited			12b. DISTRIBUTION CODE	
13. ABSTRACT (Maximum 200 Words) The goal of this research, improved diagnosis of breast cancer by quantitative, high-resolution two- and three-dimensional ultrasonic imaging, is being reached by a thorough program that synthesizes recent advances in tissue modeling, adaptive imaging, instrumentation, and signal processing. The goal of three-dimensional quantitative imaging is currently being achieved using novel time-domain inverse scattering methods invented by the Principal Investigator and coworkers. Nonlinear forms of these methods provide a robust and efficient approach to adaptive imaging, based on compensation for three-dimensional scattering from actual breast tissue structure. A crucial aspect of the research is the use of realistic tissue models for ultrasonic propagation through breast tissue. Tissue modeling techniques employ tissue maps obtained from specimen cross sections as well as from newly available high-resolution volume photographic data. Calculated scattering from these tissue models provides accurate characterization of ultrasonic propagation within breast tissue and realistic data for testing of quantitative imaging algorithms. Synthesis of these breakthroughs will make possible new mammographic applications of ultrasound that will provide clinicians with previously unavailable quantitative information and image detail. The end result will be a lower-cost, more effective, and safer modality for diagnosis, detection, and monitoring of breast cancer.				
14. SUBJECT TERMS Breast Cancer, Ultrasound, Three-Dimensional, Imaging, Scattering, Diagnosis			15. NUMBER OF PAGES 95	
			16. PRICE CODE	
17. SECURITY CLASSIFICATION OF REPORT Unclassified	18. SECURITY CLASSIFICATION OF THIS PAGE Unclassified	19. SECURITY CLASSIFICATION OF ABSTRACT Unclassified	20. LIMITATION OF ABSTRACT Unlimited	

NSN 7540-01-280-5500

Standard Form 298 (Rev. 2-89)
Prescribed by ANSI Std. Z39-18
298-102

FOREWORD

Opinions, interpretations, conclusions and recommendations are those of the author and are not necessarily endorsed by the U.S. Army.

TDM Where copyrighted material is quoted, permission has been obtained to use such material.

TDM Where material from documents designated for limited distribution is quoted, permission has been obtained to use the material.

TDM Citations of commercial organizations and trade names in this report do not constitute an official Department of Army endorsement or approval of the products or services of these organizations.


NA In conducting research using animals, the investigator(s) adhered to the "Guide for the Care and Use of Laboratory Animals," prepared by the Committee on Care and use of Laboratory Animals of the Institute of Laboratory Resources, national Research Council (NIH Publication No. 86-23, Revised 1985).

TDM For the protection of human subjects, the investigator(s) adhered to policies of applicable Federal Law 45 CFR 46.

NA In conducting research utilizing recombinant DNA technology, the investigator(s) adhered to current guidelines promulgated by the National Institutes of Health.

NA In the conduct of research utilizing recombinant DNA, the investigator(s) adhered to the NIH Guidelines for Research Involving Recombinant DNA Molecules.

NA In the conduct of research involving hazardous organisms, the investigator(s) adhered to the CDC-NIH Guide for Biosafety in Microbiological and Biomedical Laboratories.

 14 July 2000

PI - Signature Date

IV. Table of Contents

I. Title Page	1
II. Report Documentation Page (SF 298)	2
III. Foreword	3
IV. Table of Contents	4
V. Introduction	5
VI. Body of Report	6
A. Quantitative Imaging Algorithm Development	6
B. Tissue Modeling	7
C. Quantitative Imaging Algorithm Implementation	9
D. Evaluation and Comparison of Results	10
VII. Key Research Accomplishments	11
VIII. Reportable Outcomes	12
IX. Conclusions	13
X. References	14
XI. Appendices	15
A. Wideband quantitative ultrasonic imaging by time-domain diffraction tomography	15
B. Time-domain ultrasound diffraction tomography	27
C. Simulation of ultrasonic pulse propagation, distortion, and attenuation in the human chest wall	33
D. Validation of FFT-based algorithms for large-scale modeling of wave propagation in tissue	46
E. A k -space method for large-scale models of wave propagation in tissue	53
F. Abstracts	87
G. Curriculum Vitae	91

V. Introduction

An investigation of three-dimensional ultrasonic mammography is underway. The goal of the research is improved diagnosis of breast cancer by quantitative, high-resolution three-dimensional ultrasonic imaging. This goal is being reached by a thorough program that synthesizes recent advances in tissue modeling, adaptive imaging, instrumentation, and signal processing. The final result of the research will be a major advance in quantitative three-dimensional ultrasonic mammography. Improved resolution, accurate quantitative information on tissue properties, and precise determination of three-dimensional breast structure will provide crucial new information for detection, diagnosis, and monitoring of breast cancer. The goal of three-dimensional quantitative imaging is currently being achieved using novel inverse scattering methods invented by the Principal Investigator and coworkers. Use of full time-domain scattering information provides images with high point resolution, contrast resolution, and quantitative accuracy without significant artifacts. Nonlinear forms of these methods provide a robust approach to adaptive imaging that is based on compensation for three-dimensional scattering from actual tissue structure. Unlike previous adaptive imaging methods based on assumptions of phase-screen aberrators and point scatterers, these methods provide aberration correction ideally suited to distributed inhomogeneous tissue like the breast. A unique and innovative aspect of the research is the use of realistic tissue models for ultrasonic propagation through breast tissue. Such models have been shown to realistically model wavefront distortion in the human abdominal wall, but have not to date been applied to the human breast. Tissue modeling techniques employ tissue maps obtained from specimen cross sections as well as from newly available high-resolution volume photographic data. Calculated scattering from these tissue models provides accurate characterization of ultrasonic propagation within breast tissue and realistic data for quantitative imaging algorithms. The above studies will facilitate the application of breakthroughs from tissue modeling, inverse scattering, and signal processing to the critical application of ultrasonic mammography. Completion of the proposed research will make possible new mammographic applications of ultrasound that will provide clinicians with previously unavailable information and detail. The end result will be a lower-cost, more effective, and safer modality for diagnosis, detection, and monitoring of breast cancer.

VI. Body of Report

Below, the accomplishments of the second year for this project are summarized under the four categories of the approved Statement of Work. Details are given for how accomplishments to date fit into the overall research plan. Where applicable, brief descriptions of planned research indicate how the remainder of the Statement of Work will be fulfilled.

A. Quantitative Imaging Algorithm Development

A new method for ultrasonic imaging, specifically tailored to ultrasonic mammography, has also been developed. This method allows quantitative, high-resolution images to be obtained using direct synthetic-aperture processing of time-domain scattered fields. An archival manuscript regarding the method was completed, revised, and published during the second year of this project and is included as Appendix A of this report [1]. Additional results, including the reconstructions from experimentally measured ultrasonic scattering data, were presented at the 1999 IEEE Ultrasonics Symposium in November 1999; a published manuscript from the Symposium Proceedings [2] is included as Appendix B. The experimental reconstructions show considerable promise for breast cancer detection. Particularly encouraging is the fact that sub-resolvable structures appear as smoothed variations rather than as speckle.

Work has continued on the new time-domain imaging method with implementation non-linear aberration correction. Such correction provides improved synthetic focusing capability based on medium models determined from quantitative image data. In one approach, improved images are reconstructed using numerical propagation of wavefields into estimates of the unknown medium [3, 4]. In another, much more efficient approach, the quantitative sound-speed reconstruction obtained by the time-domain imaging method is employed to determine time shifts that, when applied to the measured scattering data, compensate for focus aberration caused by inhomogeneous breast tissue. An efficient implementation, in which the necessary line integrals are performed using a DDA (digital differential analyzer) method, allows each iteration to be performed as rapidly as the initial linear reconstruction. Results obtained using this method were presented at the DoD Era of Hope meeting [5] (abstracts provided in the Appendices) and are described below in this report.

The capabilities of the new time-domain imaging method are exciting for several reasons. First, the images are both higher in quality and more efficiently computed than conventional single-frequency quantitative images. The high point and contrast resolution, as well as absence of artifacts usually associated with diffraction tomography, suggests that this method will be very useful for detection and characterization of breast lesions. Second, because of the close analogy between the new method and delay-and-sum imaging, the new method could be implemented in hardware using beamforming technology already present on digital ultrasound scanners. Third, the quantitative reconstructions provided by the new method allow aberration correction to be implemented much more robustly than possible in conventional pulse-echo imaging. The new time-domain method also has the capability to incorporate other imaging techniques (*e.g.*, time-gain compensation and harmonic imaging) currently used in clinical and experimental B-scan systems.

B. Tissue Modeling

Progress toward improved scattering models for ultrasound-breast tissue interaction has been made in several studies.

Work on improved scattering models for ultrasound-tissue interaction continued. A paper on simulation of ultrasonic propagation through cross-sectional models of chest wall tissue was revised and published in JASA [6] and is included here as Appendix C. This work expands upon previous models by including tissue-dependent absorption effects and by analysis of the frequency dependence of ultrasonic wavefront distortion.

Work on k -space methods for measurements of ultrasonic scattering also continued, and significant new progress was made. A collaborative project with Weidlinger Associates and the University of Rochester provided detailed quantitative comparisons between a new k -space method and a state-of-the-art pseudospectral solver. This study showed that the k -space method has strong advantages for large-scale simulations of propagation through soft tissue, which is precisely the simulation problem of interest for the USAMRMC-funded breast cancer study. The comparison was presented at the 1999 IEEE Ultrasonics Symposium and has been published in the proceedings of that symposium; a copy of that publication is included here as Appendix D [7].

Knowledge gained from the abovementioned comparison project led to a number of improvements in the k -space method, including improved computational efficiency, more accurate interpolation of simulated pressure signals, and more effective methods to compute scattering from media including discontinuities. These improvements were reported in a presentation to the Acoustical Society of America [4], (abstract provided in the Appendices). These comparisons, as well as new analysis that explains the remarkable stability and accuracy of the k -space method, greatly improved the extensively revised version of a manuscript accepted for publication [8] that is provided here as Appendix E.

Now that a robust, efficient three-dimensional method for computation of ultrasonic propagation is available, work on mapping of breast tissue has begun in earnest. In collaboration with colleagues at the University of Rochester, cross-sectional breast tissue specimens have been sectioned and stained for high-resolution segmentation by tissue type. One such tissue cross section is shown, together with a computed ultrasonic pulse propagating within the tissue, in Fig. 1. The ultrasonic propagation was computed using the k -space method, which provides much greater efficiency and accuracy than the finite-difference method used in previous simulation studies of propagation through tissue [6, 9, 10].

During the second year of the project, photographic image data from the Visible Woman data set [11] was also analyzed to obtain quantitative maps of breast tissue for simulation studies and testing of imaging algorithms. A method in which hue, saturation, and value are mapped to tissue type was applied; this method also incorporates nonlinear processing to enforce uniformity among multiple layers in three-dimensional breast models. An example two-dimensional simulation, using the k -space method and a Visible Woman breast model, is shown in Fig. 2.

During the third year of the project, the new automatic segmentation method will be applied to three-dimensional photographic data from the Visible Woman data set to obtain definitive three-dimensional models of breast tissue structure for studies of ultrasonic

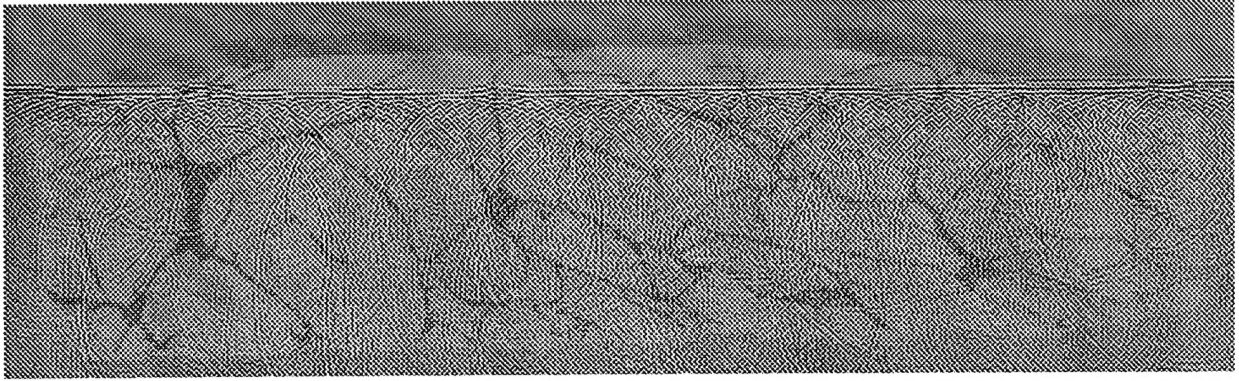


Figure 1: Ultrasonic propagation of a 2.5 MHz pulse through a two-dimensional breast cross-sectional model obtained from a segmented, stained breast tissue cross section. An area of $167 \times 50 \text{ mm}^2$ is shown.

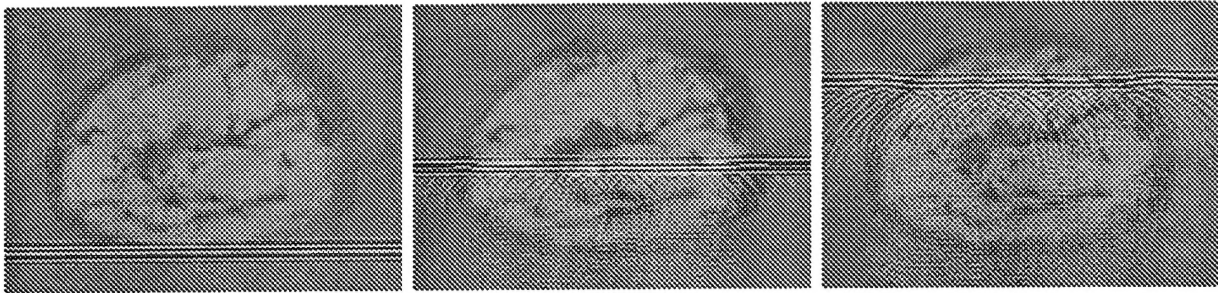


Figure 2: Three frames showing ultrasonic propagation of a 1 MHz pulse through a two-dimensional breast cross-sectional model obtained from the Visible Woman data set. Each panel shows an area of $97 \times 69 \text{ mm}^2$.

propagation and imaging.

C. Quantitative Imaging Algorithm Implementation

Quantitative reconstructions performed using the time-domain diffraction tomography method are shown in Refs. [1] (Appendix A) and [2] (Appendix B) for simulated two-dimensional and three-dimensional scattering data. These results are promising for ultrasonic mammography. As discussed below in section D (Evaluation and Comparison of Results), time-domain quantitative images show parametric accuracy, high resolution, and few artifacts. Effects of limited scattering data, shown in Fig. 3 of Appendix A for the 2D case, indicate that accurate images can be obtained without the necessity of apertures that entirely enclose the breast.

Reconstructions employing experimentally measured scattering data have also been performed in collaboration with colleagues at the University of Rochester. Tissue-mimicking phantoms composed of agar gel with glass spheres have been constructed and their scattering has been measured using a 2048-element ring transducer. Reconstructions using the new time-domain diffraction tomography method are shown in Ref. [2] (Appendix B). These

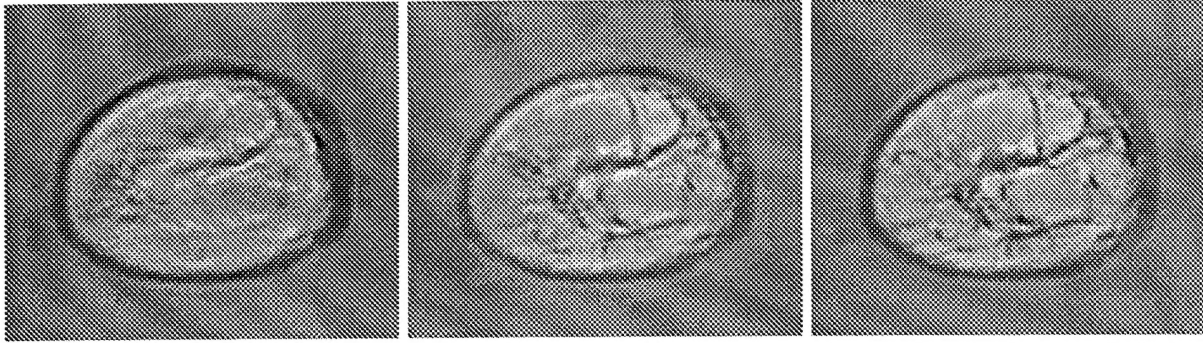


Figure 3: Aberration correction applied to time-domain quantitative imaging of a breast tissue model. From left to right: unaberrated image; first iteration; second iteration. Each panel shows the reconstructed sound speed as a linear grayscale image, with black indicating the maximum sound speed (*e.g.*, connective tissue) and white indicating minimum speed (*e.g.*, fat).

reconstructions show great promise for practical implementation of the new time-domain diffraction tomography method for breast imaging *in vivo*.

An anthropomorphic breast-mimicking phantom, developed in collaboration between General Electric, University of Wisconsin, and University of Rochester, is also available for testing. Time-domain scattering data, to be taken with the 2048-element University of Rochester ring transducer [12] will be used as input for testing of the new time-domain quantitative imaging method. Both 2D and 3D reconstructions will be performed.

As described above, a nonlinear, aberration-corrected version of the new time-domain inverse scattering method has been implemented and tested with simulated data (from the breast tissue models described above in section B, Tissue Modeling). Preliminary results, as seen in Figure 3, indicate that the aberration correction scheme will allow accurate ultrasonic images of whole breasts to be obtained. During the third year of the project, aberration-corrected time-domain diffraction tomography will also be applied to imaging of large phantoms, such as the GE breast phantom, from experimentally measured scattering data.

D. Evaluation and Comparison of Results

Analysis of the time-domain imaging results for simulated data is given in Ref. [1] (Appendix A). These results indicate that high quantitative accuracy can be achieved. Computations of point-spread functions (Fig. 2 in Appendix A) show that the time-domain method yields higher point and contrast resolution than single-frequency diffraction tomography. For the 3D case, the level of the first sidelobe is reduced by 13 dB, while the second sidelobe is reduced by 18 dB. Because of the broadband scattering information employed, the width of the main lobe indicates point resolution of features smaller than one-half wavelength at the center frequency.

Evaluation of quantitative accuracy (Fig. 4 in Appendix A) shows that the time-domain diffraction tomography method provides parametric accuracy similar to established single-

frequency methods while showing much more immunity from artifacts. The new aberration correction method, described above and illustrated in Fig. 1, provides high quantitative accuracy even for imaging of large inhomogeneities for which the Born approximation does not hold.

Two-dimensional and three-dimensional reconstructions performed using the new time-domain quantitative imaging method will be directly compared to analogous images from other modalities such as x-ray computed tomography and conventional B-scan ultrasound. Consultants Dr. Jonathan Meilstrup and Dr. Claudia Kasales will help with this portion of evaluation and comparison of results. This evaluation task will take place during the third year of the project.

Quantitative evaluation of the k -space method for simulation of ultrasonic propagation has been performed and is reported in Refs. [7] (Appendix D) and [8] (Appendix E). These results show that the k -space method provides much higher accuracy than finite-difference or pseudospectral methods. A particularly striking result is that simulated ultrasonic waves can propagate many thousands of wavelengths without distortion [4].

Regarding the task of publishing results in archival journals, the second year of the project has resulted in two published articles, one accepted article, and two articles in a peer-reviewed conference proceedings volume. Further publications planned to be prepared during the next year will be based on aberration-corrected time-domain diffraction tomography, modeling of breast tissue based on the Visible Woman data set, and scattering computations employing realistic breast tissue models.

VII. Key Research Accomplishments

The key research accomplishments to date in this project can be summarized as follows:

- Development of a new time-domain quantitative imaging method designed specifically for ultrasonic mammography.
- Numerical implementation and testing of the new time-domain imaging method, showing that this method provides high accuracy with greater efficiency than previous inverse scattering methods.
- Testing of the time-domain imaging method using scattering data measured by a 2048-element ring transducer.
- Implementation of aberration correction to the time-domain quantitative imaging method.
- Implementation of a tissue-dependent absorption model for simulations of scattering and propagation.
- Characterization of the frequency dependence of ultrasonic scattering from human soft tissues.
- Exact computation of time-domain scattering from simple objects for testing of quantitative imaging methods.
- Implementation and testing of a new k -space method for computation of scattering, indicating that the method is accurate and extremely efficient, and therefore ideal for the proposed 3D computations of scattering from breast tissue.
- Extension of the new k -space method to include tissue-dependent absorption, absorbing boundary layers, and three-dimensional scattering.
- Development of realistic breast tissue models using stained tissue cross sections and photographic data from the Visible Woman data set.
- Use of the k -space method to compute time-domain scattering data from realistic breast tissue models, for analysis of wavefront distortion and testing of quantitative imaging algorithms.
- Quantitative analysis of inverse scattering results, indicating that time-domain reconstructions provide much higher point resolution, contrast resolution, and freedom from artifacts than single-frequency reconstructions.

VIII. Reportable Outcomes

Reportable outcomes for the second year of this project research have included two papers published in archival journals [1, 6], one additional accepted paper [8], two papers published in the 2000 IEEE Ultrasonics Symposium Proceedings [2, 7], and two published abstracts presented at scientific meetings [5, 4]. All of these publications, as well as a current Curriculum Vitae for the Principal Investigator, are included below in the Appendices.

Accomplishments performed under the USAMRMC-funded project have facilitated applications for other funding support. The proposal "High-Resolution Breast Tissue Mapping using Pulse-Echo Ultrasonography" (T. Douglas Mast, Principal Investigator) was submitted to the Concept Award program of the USAMRMC. This study was not funded. An additional proposal, "Optimized Intracavitary Ultrasound Array for Uniform Hyperthermia Treatment of Prostate Cancer" (Nadine B. Smith, Principal Investigator; T. Douglas Mast, Co-Principal Investigator; funding notification pending) was submitted to the DoD Prostate Cancer Research Program. Although not a direct extension of the present ultrasonic mammography project, the proposed project would leverage the advanced tissue modeling techniques developed for the current USAMRMC-funded research.

The Principal Investigator of this project has been appointed to the position of Assistant Professor in the Pennsylvania State University Graduate Program in Acoustics. During the Spring of 2000, he taught a well-received upper-level graduate course on acoustic scattering. This course included a comprehensive treatment of ultrasonic scattering by human tissues, and was greatly enriched by the Principal Investigator's research performed for the present USAMRMC-funded project.

A student, James F. Kelly, has recently been added to the project team. Mr. Kelly is not directly funded by the USAMRMC, but instead is supported by the Mathematics Honor Student program of the Applied Research Laboratory. He is currently exploring aspects of the time-domain inverse scattering problem, including deconvolution of scattered wavefields, that extend the present Statement of Work (some of this includes research into ideas discussed in the abovementioned Concept Award proposal). If successful, these exploratory studies will allow the imaging methods developed under the USAMRMC-funded research to achieve practical application even more rapidly.

IX. Conclusions

The second year of this USAMRMC-funded project has yielded considerable progress toward the goal of improved diagnosis of breast cancer by three-dimensional ultrasonic imaging. Several breakthroughs have been made which will provide a solid foundation for the continued tissue modeling and quantitative imaging research planned for the last year of the project.

Breakthroughs in the area of quantitative imaging have included successful imaging of tissue-mimicking phantoms using measured scattering data as well as implementation of a new aberration correction method for quantitative ultrasonic mammography. The present method is potentially of very great importance for breast cancer diagnosis for several reasons: (1) images have higher quality than that achievable by conventional inverse scattering methods or by current ultrasound scanners, (2) tissue parameters are computed and quantitatively imaged with high accuracy, and (3) the close analogy between the new method and conventional synthetic-aperture imaging will allow rapid implementation of the new method on hardware similar to currently used beamformers. The additional improvement of aberration correction increases the value of this method even more, because the strong scattering inherent to breast tissue [13] is an important limiting factor to existing ultrasonic imaging methods.

In the area of breast tissue modeling, simulation methods have been developed that will allow efficient computation of scattering from fully three-dimensional models of breast tissue. A new k -space method has been implemented, rigorously tested, and extended to include absorbing boundary conditions as well as tissue-dependent ultrasonic absorption. The method has been shown to provide the accuracy and efficiency needed for large-scale computations of ultrasonic propagation within the human breast. A three-dimensional implementation of this method is already in place. Breast tissue models have been developed using both stained cross sections of human breast tissue and photographic image data from the Visible Woman project of the National Library of Medicine.

Future work based on these breakthroughs will follow the approved Statement of Work. Plans for the final year of research include detailed simulation of ultrasound interaction with breast tissue for two- and three-dimensional tissue models. Definitive aberration-corrected reconstructions will be computed both for measured scattering data from breast-mimicking phantoms and for simulated scattering data using detailed breast models. These results will be carefully evaluated for accuracy and clinical utility, in collaboration with the named clinical consultants.

The final outcome of the successfully completed project will be a novel method for early detection, characterization, and treatment monitoring of breast cancer lesions. Results to date indicate that the final method will provide image quality and diagnostic information greatly superior to current 2D and 3D ultrasonic mammography methods. The finally resulting method is expected to be competitive with magnetic resonance imaging and x-ray computed tomography as a tool for breast cancer diagnosis, while maintaining inherent advantages of ultrasound such as lower cost, ability to characterize cystic and solid lesions, and safe nonionizing radiation.

X. References

- [1] Mast, T. D., "Wideband quantitative ultrasonic imaging by time-domain diffraction tomography," *J. Acoust. Soc. Am.* **106**, 3061-3071 (1999).
- [2] Mast, T. D., Lin, F., and Waag, R. C., "Time-domain ultrasound diffraction tomography," *1999 IEEE Ultrasonics Symposium Proceedings*, Vol. 2, pp. 1617-1620.
- [3] Mast, T. D., Nachman, A. I., and Waag, R. C., "Focusing and imaging using eigenfunctions of the scattering operator," *J. Acoust. Soc. Am.* **102**, 715-725 (1997).
- [4] T. D. Mast, D.-L. D. Liu, L. P. Souriau, A. I. Nachman, and R. C. Waag, "A new k -space method for simulation of ultrasonic propagation in tissue," *J. Acoust. Soc. Am.* **106**, 2135 (1999).
- [5] Mast, T. D., "Time-domain inverse scattering for quantitative ultrasonic mammography," in *Era of Hope: Proceedings of the Department of Defense Breast Cancer Research Program Meeting*, Vol. 1, p. 224 (2000).
- [6] Mast, T. D., Hinkelman, L. M., Metlay, L. A., Orr, M. J., and Waag, R. C., "Simulation of ultrasonic pulse propagation, distortion, and attenuation in the human chest wall," *J. Acoust. Soc. Am.* **106**, 3665-3677 (1999).
- [7] Mould, J. C. Wojcik, G. L., Carcione, L. M., Tabei, M., Mast, T. D., and Waag, R. C., "Validation of FFT-based algorithms for large-scale modeling of wave propagation in tissue," *1999 IEEE Ultrasonics Symposium Proceedings*, Vol. 2, pp. 1551-1556.
- [8] Mast, T. D., Souriau, L. P., Liu, D.-L. D., Tabei, M., Nachman, A. I., and Waag, R. C., "A k -space method for large-scale models of wave propagation in tissue," to appear in *IEEE Trans. Ultrason. Ferroelect. Freq. Control* (2000).
- [9] Mast, T. D., Hinkelman, L. M., Orr, M. J., Sparrow, V. W., and Waag, R. C., "Simulation of ultrasonic pulse propagation through abdominal wall," *J. Acoust. Soc. Am.* **102**, 1177-1190 (1997).
- [10] Mast, T. D., Hinkelman, L. M., Orr, M. J., and Waag, R. C., "The effect of abdominal wall morphology on ultrasonic pulse distortion. Part II: Simulations," *J. Acoust. Soc. Am.* **104**, 3650-3664 (1998).
- [11] National Library of Medicine (US) Board of Regents, "Electronic Imaging: Report of the Board of Regents," NIH Publication 90-2197 (1990).
- [12] Jansson, T. T., Mast T. D., and Waag, R. C., "Measurements of differential scattering cross-section using a ring transducer," *J. Acoust. Soc. Am.* **103**, 3169-3179 (1998).
- [13] Hinkelman, L. M., Liu, D.-L., Waag, R. C., Zhu, Q., and Steinberg, B. D., "Measurement and correction of ultrasonic pulse distortion produced by the human breast," *J. Acoust. Soc. Am.* **97**, 1958-1969 (1995).

XI. Appendices

Appendix A

Wideband Quantitative Ultrasonic Imaging
by Time-Domain Diffraction Tomography

Journal of the Acoustical Society of America **106**, 3061–3171 (1999)

Annual Report for DAMD17-98-1-8141, July 2000

Pages 16–26

Wideband quantitative ultrasonic imaging by time-domain diffraction tomography

T. Douglas Mast

Applied Research Laboratory, The Pennsylvania State University, University Park, Pennsylvania 16802

(Received 3 April 1999; revised 27 August 1999; accepted 30 August 1999)

A quantitative ultrasonic imaging method employing time-domain scattering data is presented. This method provides tomographic images of medium properties such as the sound speed contrast; these images are equivalent to multiple-frequency filtered-backpropagation reconstructions using all frequencies within the bandwidth of the incident pulse employed. However, image synthesis is performed directly in the time domain using coherent combination of far-field scattered pressure waveforms, delayed and summed to numerically focus on the unknown medium. The time-domain method is more efficient than multiple-frequency diffraction tomography methods, and can, in some cases, be more efficient than single-frequency diffraction tomography. Example reconstructions, obtained using synthetic data for two- and three-dimensional scattering of wideband pulses, show that the time-domain reconstruction method provides image quality superior to single-frequency reconstructions for objects of size and contrast relevant to medical imaging problems such as ultrasonic mammography. The present method is closely related to existing synthetic-aperture imaging methods such as those employed in clinical ultrasound scanners. Thus, the new method can be extended to incorporate available image-enhancement techniques such as time-gain compensation to correct for medium absorption and aberration correction methods to reduce error associated with weak scattering approximations. © 1999 Acoustical Society of America.

[S0001-4966(99)04612-3]

PACS numbers: 43.20.Fn, 43.60.Rw, 43.80.Vj, 43.20.Px [ANN]

INTRODUCTION

Quantitative imaging of tissue properties is a potentially useful technique for diagnosis of cancer and other pathological conditions. Inverse scattering methods such as diffraction tomography can provide quantitative reconstruction of tissue properties including sound speed, density, and absorption. However, although previous inverse scattering methods have achieved high resolution and quantitative accuracy, such methods have not yet been incorporated into commercially successful medical ultrasound imaging systems.

Current inverse scattering methods are lacking in several respects with respect to conventional B-scan and synthetic aperture imaging techniques. Previous methods of diffraction tomography, including methods based on the Born and Rytov approximations,^{1,2} and higher-order nonlinear approaches,^{3,4} have usually been based on single-frequency scattering, while current diagnostic ultrasound scanners employ wideband time-domain signals. The use of wideband information in image reconstruction is known to provide increased point and contrast resolution,^{5,6} both of which are important for medical diagnosis.^{5,7,8}

Several approaches have been used to incorporate wideband scattering information into quantitative ultrasonic imaging. One group of methods employs time-domain tomography based on Radon-transform relationships that hold (under the assumption of weak scattering) between scattered acoustic fields and the reflectivity or scattering strength of the medium. Pioneering work in this area^{9,10} employed measurements of reflectivity in pulse-echo mode, while later studies have incorporated aberration correction^{11,12} and multiple-angle scattering measurements.^{13,14} A limitation of

these methods, however, is that the Radon transform relationship strictly holds only when the medium is insonified by an impulsive (infinite bandwidth) wave. When pulses of finite bandwidth are employed, image quality can degrade significantly.¹⁵

A number of linear and nonlinear diffraction tomography methods have been implemented using scattering data for a number of discrete frequencies (e.g., Refs. 16–19). Although use of multiple-frequency data provides improvements in image quality, computational requirements for multiple-frequency imaging are typically large because the computational cost is proportional to the number of frequencies employed. To achieve image quality competitive with present diagnostic scanners, together with quantitative imaging of tissue properties, present frequency-domain methods may require solution of the inverse scattering problem for many frequencies within the bandwidth of the transducer employed. This approach thus demands a high computational cost, so that high-quality real-time imaging may not be presently feasible using current frequency-domain inverse scattering methods.

Very few previous workers have investigated direct use of time-domain waveform data for inverse scattering methods analogous to frequency-domain diffraction tomography. Several methods^{20,21} have used frequency decomposition of scattered pulses to construct a wideband estimate of the spatial Fourier transform of an unknown medium; after appropriate averaging and interpolation, this transform can be inverted to obtain a wideband Born reconstruction of the medium. A study reported in Ref. 22 has showed that broadband synthetic aperture imaging using linear arrays is closely

related to inverse scattering using filtered backpropagation. A related method, suggested in Ref. 23, provides a time-domain reconstruction algorithm that employs filtered backpropagation of scattered waveforms measured on a circular boundary. However, the time domain reconstruction formula of Ref. 23 yields reconstructions that are less general than multiple-frequency reconstructions obtained using the same signal bandwidth.

Another approach, related both to multiple-frequency methods and direct time-domain methods, has recently been presented.²⁴ This work extends the eigenfunction method of Ref. 19 to use the full bandwidth of the incident pulse waveform. In the extended method, eigenfunctions and eigenvalues of a scattering operator are computed to obtain a frequency-dependent representation of the scattering medium. Fourier synthesis is then applied to obtain a time-dependent estimate of the medium. A cross-correlation operation removes the time dependence of the estimate as well as its dependence on the waveform employed.

The present paper offers a new approach to wideband quantitative imaging: a time-domain inverse scattering method that overcomes some of the limitations of previous frequency-domain and time-domain quantitative imaging methods. The new method provides tomographic reconstructions of unknown scattering media using the entire available bandwidth of the signals employed. Reconstructions are performed using scattering data measured on a surface surrounding the region of interest, so that the method is well suited to ultrasonic mammography. The reconstruction algorithm is derived as a simple delay-and-sum formula similar to synthetic-aperture algorithms employed in conventional clinical scanners. However, unlike current clinical scanners, the present method can provide quantitative images of tissue properties such as the spatially dependent sound speed. Reconstructions obtained in this manner are equivalent to reconstructions obtained by combining conventional frequency-domain diffraction tomography reconstructions for all frequencies within the signal bandwidth of interest. The current method, however, can be even more efficient than single-frequency diffraction tomography. The method is applicable both to two-dimensional and three-dimensional image reconstruction. The direct time-domain nature of the reconstruction algorithm allows straightforward incorporation of depth- and frequency-dependent amplitude correction to compensate for medium absorption as well as aberration correction methods to overcome limitations of the Born approximation.

I. THEORY

A. The time-domain reconstruction algorithm

An inverse scattering algorithm, applicable to quantitative imaging of tissue and other inhomogeneous media, is derived below. For simplicity of derivation, the medium is modeled as a fluid medium defined by the sound speed contrast function

$$\gamma(\mathbf{r}) = \frac{c_0^2}{c(\mathbf{r})^2} - 1, \quad (1)$$

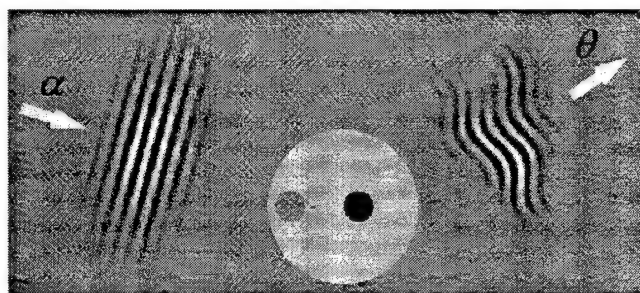


FIG. 1. Scattering configuration. An incident pressure pulse $f(t - \mathbf{r} \cdot \boldsymbol{\alpha}/c)$ is scattered by an inhomogeneous medium and the time-domain scattered pressure $p_s(\boldsymbol{\theta}, \mathbf{r}, t)$ is measured at a radius R in the far field.

where c_0 is a background sound speed and $c(\mathbf{r})$ is the spatially dependent sound speed defined at all points \mathbf{r} . For the scope of the initial derivation, the medium is assumed to have constant density, no absorption, and weak scattering characteristics; extensions to the reconstruction algorithm that overcome these limiting assumptions are discussed in the following section.

For the model of the scattering medium represented by Eq. (1), the time-domain scattered acoustic pressure $p_s(\mathbf{r}, t)$ obeys the wave equation²⁵

$$\nabla^2 p_s(\mathbf{r}, t) - \frac{1}{c_0^2} \frac{\partial^2 p_s(\mathbf{r}, t)}{\partial t^2} = \frac{\gamma(\mathbf{r})}{c_0^2} \frac{\partial^2 p(\mathbf{r}, t)}{\partial t^2}, \quad (2)$$

where $p(\mathbf{r}, t)$ is the total acoustic pressure in the medium.

The scattering configuration considered here is sketched in Fig. 1. The medium is subjected to a pulsatile plane wave propagating in the direction of the unit vector $\boldsymbol{\alpha}$,

$$p_{\text{inc}}(\mathbf{r}, \boldsymbol{\alpha}, t) = f(t - \mathbf{r} \cdot \boldsymbol{\alpha}/c_0), \quad (3)$$

where f is the time-domain waveform and c_0 is the background sound speed. The scattered wavefield $p_s(\boldsymbol{\theta}, \mathbf{r}, t)$ is measured at a fixed radius R in the far field, where $\boldsymbol{\theta}$ corresponds to the direction unit vector of a receiving transducer element. (Alternatively, if scattering measurements are made in the near field, the far-field acoustic pressure can be computed using exact transforms that represent propagation through a homogeneous medium.¹⁶)

A general time-domain solution for the wave equation (2), valid for two-dimensional (2D) or three-dimensional (3D) scattering, is then

$$p_s(\boldsymbol{\theta}, \mathbf{r}, t) = \int_{-\infty}^{\infty} \hat{p}_s(\boldsymbol{\theta}, \mathbf{r}, \omega) e^{-i\omega t} d\omega, \quad (4)$$

where $\hat{p}_s(\boldsymbol{\theta}, \mathbf{r}, \omega)$ is a single frequency component of the scattered wavefield,

$$\hat{p}_s(\boldsymbol{\theta}, \mathbf{r}, \omega) = \frac{1}{2\pi} \int_{-\infty}^{\infty} p_s(\boldsymbol{\theta}, \mathbf{r}, t) e^{i\omega t} dt, \quad (5)$$

given exactly by²⁵

$$\begin{aligned} \hat{p}_s(\boldsymbol{\theta}, \mathbf{r}, \omega) = & k^2 \hat{f}(\omega) \int G_0(R\boldsymbol{\theta} - \mathbf{r}_0, \omega) \\ & \times \gamma(\mathbf{r}_0) \hat{p}(\mathbf{r}, \boldsymbol{\alpha}, \omega) dV_0. \end{aligned} \quad (6)$$

In Eq. (6), k is the wave number ω/c_0 and $\hat{p}(\mathbf{r}_0, \boldsymbol{\alpha}, \omega)$ is the total acoustic pressure associated with the unit-amplitude incident plane wave $e^{ik\boldsymbol{\alpha} \cdot \mathbf{r}_0}$. The integral in Eq. (6) is taken over the entire support of γ in \mathbb{R}^2 for 2D scattering or in \mathbb{R}^3

for 3D scattering. The free-space Green's function, represented by G_0 in Eq. (6), is²⁶

$$G_0(\mathbf{r}, \omega) = \frac{i}{4} H_0^{(1)}(kr) \quad \text{for 2D scattering}$$

and

$$G_0(\mathbf{r}, \omega) = \frac{e^{ikr}}{4\pi r} \quad \text{for 3D scattering,}$$

where $H_0^{(1)}$ is the zeroth-order Hankel function of the first kind and r is the magnitude of the vector \mathbf{r} .

The far-field scattered pressure, when specified for all incident-wave directions α , measurement directions θ , and times t , comprises the data set to be used for reconstruction of the unknown medium. The inverse scattering problem, specified by Eq. (6) for a single frequency component, is to reconstruct the unknown medium contrast $\gamma(\mathbf{r})$ using the measured data $\hat{p}_s(\theta, \alpha, \omega)$.

The starting point for the present time-domain inverse scattering method is conventional single-frequency diffraction tomography. Under the assumption of weak scattering, one can make the Born approximation, in which the total pressure $\hat{p}(\alpha, \omega)$ in Eq. (6) is replaced by the plane wave $e^{ikr \cdot \alpha}$. For scattering measurements made at a radius R in the far field, the linearized inverse problem of Eq. (6) can be then solved for any frequency component using filtered backpropagation,^{2,16,27} i.e.,

$$\gamma_B(\mathbf{r}, \omega) = \frac{\hat{\mu}(\omega) e^{-ikR}}{\hat{f}(\omega)} \int \int \Phi(\theta, \alpha) \times \hat{p}_s(\theta, \alpha, \omega) e^{ik(\theta - \alpha) \cdot \mathbf{r}} dS_\alpha dS_\theta, \quad (8)$$

where

$$\hat{\mu}(\omega) = -\sqrt{\frac{kR}{8i\pi^3}},$$

$$\Phi(\theta, \alpha) = |\sin(\theta - \alpha)| \quad \text{in 2D,}$$

and

$$\hat{\mu}(\omega) = \frac{kR}{4\pi^3}, \quad \Phi(\theta, \alpha) = |\theta - \alpha| \quad \text{in 3D.} \quad (9)$$

Each surface integral in Eq. (8) is performed over the entire measurement circle for the 2D case and over the entire measurement sphere for the 3D case. Equation (8) provides an exact solution to the linearized inverse scattering problem for a single frequency component of the scattered wavefield $p_s(\theta, \alpha, t)$. The resulting reconstruction, $\gamma_B(\mathbf{r}, \omega)$, has spatial frequency content limited by the "Ewald sphere" of radius $2k$ in wavespace.¹

To improve upon the single-frequency formulas specified by Eq. (8), one can extend the spatial-frequency content of reconstructions by exploiting wideband scattering information. The method outlined here synthesizes a "multiple-frequency" reconstruction $\gamma_M(\mathbf{r})$ by formally integrating single-frequency reconstructions $\gamma_B(\mathbf{r}, \omega)$ over a range of frequencies ω . A generalized formula for this approach can be written

$$\gamma_M(\mathbf{r}) = \frac{\int_0^\infty \hat{g}(\omega) \gamma_B(\mathbf{r}, \omega) d\omega}{\int_0^\infty \hat{g}(\omega) d\omega}, \quad (10)$$

where $\hat{g}(\omega)$ is an appropriate frequency-dependent weighting function. In practice, the weighting function $\hat{g}(\omega)$ is chosen to be bandlimited because (for a given set of physical scattering measurements) the frequency-dependent contrast $\gamma_B(\mathbf{r}, \omega)$ can only be reliably reconstructed for a finite range of frequencies ω associated with the spectra of the incident waves employed. Thus, the integrands in Eq. (10) are non-zero only over the support of $\hat{g}(\omega)$ and the corresponding integrals are finite.

Using Eq. (8), and making the definition

$$N \equiv 2 \int_0^\infty \hat{g}(\omega) d\omega, \quad (11)$$

Eq. (10) can be written in the form

$$\gamma_M(\mathbf{r}) = \frac{2}{N} \int_0^\infty \hat{g}(\omega) \frac{\hat{\mu}(\omega) e^{-ikR}}{\hat{f}(\omega)} \int \int \Phi(\theta, \alpha) \times \hat{p}_s(\theta, \alpha, \omega) e^{ik(\theta - \alpha) \cdot \mathbf{r}} dS_\alpha dS_\theta d\omega. \quad (12)$$

If the frequency weight $\hat{g}(\omega)$ is now specified to incorporate the incident-pulse spectrum $\hat{f}(\omega)$ and to compensate for the frequency- and dimension-dependent coefficient $\hat{\mu}(\omega)$,

$$\hat{g}(\omega) = \frac{\hat{f}(\omega)}{\hat{\mu}(\omega)}, \quad (13)$$

Eq. (12) reduces to the form

$$\gamma_M(\mathbf{r}) = \frac{2}{N} \int \int \Phi(\theta, \alpha) \int_0^\infty \hat{p}_s(\theta, \alpha, \omega) \times e^{-ik[R + (\alpha - \theta) \cdot \mathbf{r}]} d\omega dS_\alpha dS_\theta. \quad (14)$$

The choice of frequency weight from Eq. (13) allows the multiple-frequency reconstruction formula of Eq. (12) to be greatly simplified. Specifically, the inner integral of Eq. (14) resembles a weighted inverse Fourier transform of the frequency-domain scattered field $\hat{p}(\theta, \alpha, \omega)$. To obtain an explicit time-domain expression for $\gamma_M(\mathbf{r})$, Eq. (14) can be rewritten using the definition of $\hat{p}_s(\theta, \alpha, \omega)$ from Eq. (5) to yield

$$\gamma_M(\mathbf{r}) = \frac{1}{N} \int \int \Phi(\theta, \alpha) \times \mathbf{L} \left[p_s \left(\theta, \alpha, R/c_0 + \frac{(\alpha - \theta) \cdot \mathbf{r}}{c_0} \right) \right] dS_\alpha dS_\theta, \quad (15)$$

where \mathbf{L} denotes the linear operator

$$\mathbf{L}[\psi(t)] = 2 \int_0^\infty \hat{\psi}(\omega) e^{-i\omega t} d\omega \quad (16)$$

and $\hat{\psi}(\omega)$ is the Fourier transform of $\psi(t)$ using the definition from Eq. (5).

Using the conjugate symmetry of $\hat{\psi}(\omega)$ [i.e., $\hat{\psi}(\theta, \alpha, \omega) = \hat{\psi}^*(\theta, \alpha, -\omega)$ for any real $\psi(t)$], the real part of

$\mathbf{L}[\psi(t)]$ is shown to be simply $\psi(t)$. Similarly, using the convolution theorem as well as the conjugate symmetry of $\psi(t)$, the imaginary part of $\mathbf{L}[\psi(t)]$ is seen to be an inverse Hilbert transform²⁸ of $\psi(t)$,

$$\text{Im}[\mathbf{L}[\psi(t)]] = -\frac{1}{\pi} \int_{-\infty}^{\infty} \frac{\psi(\tau)}{t-\tau} d\tau = \mathbf{H}^{-1}[\psi(t)]. \quad (17)$$

This transform, also known as a quadrature filter, applies a phase shift of $\pi/2$ to each frequency component of the input signal.

Thus, the time-domain reconstruction formula can finally be written

$$\gamma_M(\mathbf{r}) = \frac{1}{N} \iint \Phi(\boldsymbol{\theta}, \boldsymbol{\alpha}) \left(p_s(\boldsymbol{\theta}, \boldsymbol{\alpha}, \tau) + i\mathbf{H}^{-1}[p_s(\boldsymbol{\theta}, \boldsymbol{\alpha}, \tau)] \right) dS_{\boldsymbol{\alpha}} dS_{\boldsymbol{\theta}}, \quad (18)$$

where

$$\tau = R/c_0 + \frac{(\boldsymbol{\alpha} - \boldsymbol{\theta}) \cdot \mathbf{r}}{c_0}. \quad (19)$$

The direction-dependent weight $\Phi(\boldsymbol{\theta}, \boldsymbol{\alpha})$, which is the same as the "filter" employed in single-frequency filtered back-propagation, is given for the 2D and 3D cases by Eq. (9).

Equation (18) is notable in several respects. First, it provides a linearized reconstruction that employs scattering information from the entire signal bandwidth without any frequency decomposition of the scattered wavefield. Second, the delay term τ corresponds exactly to the delay required to construct a focus at the point \mathbf{r} by delaying and summing the scattered wavefield $p_s(\boldsymbol{\theta}, \boldsymbol{\alpha}, t)$ for all measurement directions $\boldsymbol{\theta}$ and incident-wave directions $\boldsymbol{\alpha}$. Thus, the time-domain reconstruction formula given by Eq. (18) can be regarded as a quantitative generalization of confocal time-domain synthetic aperture imaging, in which signals are synthetically delayed and summed for each transmit/receive pair to focus at the image point of interest.^{22,29,30}

A reconstruction formula similar to, although less general than, Eq. (18) was independently derived in Ref. 23 for the two-dimensional inverse scattering problem. In view of the present derivation, the method of "probing by plane pulses" in Ref. 23 can be regarded to yield a multiple-frequency reconstruction of $\text{Re}[\gamma_M(\mathbf{r})]$, while the present method yields the complex function $\gamma_M(\mathbf{r})$. In Ref. 23, this method was proposed as a more convenient way to implement narrow-band diffraction tomography. However, the numerical results given below show that the reconstruction formula of Eq. (18), when directly implemented using wideband signals, provides considerable improvement in image quality over narrow-band reconstructions.

Reconstructions using Eq. (18) can be performed using any pulse waveform. However, the frequency compounding defined by Eq. (10) is most straightforwardly interpreted if the frequency weight $\hat{g}(\omega)$ has a phase that is independent of frequency. This criterion can be met, for instance, if the incident pulse waveform $f(t)$ is even in time,

$$f(t) = f(-t), \quad (20)$$

so that $\hat{f}(\omega)$ is purely real. [Similarly, if the incident pulse waveform is odd in time, $\hat{f}(\omega)$ is purely imaginary and Eq. (18) can still be employed.]

However, supposition of a frequency-independent phase for $\hat{f}(\omega)$ does not result in any loss of generality. For any linear-phase signal, such that the Fourier transform has the form

$$\hat{f}(\omega) = |\hat{f}(\omega)| e^{i\omega\zeta}, \quad \omega > 0, \quad (21)$$

an additional delay term of magnitude ζ can be applied to all scattered signals to obtain the signals associated with the purely-real spectrum $|\hat{f}(\omega)|$. In general, the scattered field associated with a desired waveform $f(t)$ can be determined for an arbitrary waveform $u(t)$ from the deconvolution operation

$$[p_s(\boldsymbol{\theta}, \boldsymbol{\alpha}, t)]_{f(t)} = \mathbf{F}^{-1} \left[\frac{\hat{f}(\omega)}{\hat{u}(\omega)} [p_s(\boldsymbol{\theta}, \boldsymbol{\alpha}, t)]_{u(t)} \right]. \quad (22)$$

For stable deconvolution using Eq. (22), the desired $\hat{f}(\omega)$ should not have significant frequency components outside the bandwidth of $\hat{u}(\omega)$.

B. Extensions to the reconstruction algorithm

For large tissue structures at high ultrasonic frequencies, weak scattering approximations such as the Born approximation are of limited validity. Thus, for problems of interest to medical ultrasonic imaging, reconstructed image quality can be improved by aberration correction methods that incorporate higher-order scattering and propagation effects. The present time-domain reconstruction formula (18) provides a natural framework for quantitative imaging with aberration correction. In general, if the background medium is known or can be estimated, the received scattered signals can be processed to provide an estimate of the scattered field that would be measured for the same scatterer within a homogeneous background medium. This approach essentially removes higher-order scattering effects from the measured far field scattering, so that a Born inversion can be performed on the modified data; similar processes occur implicitly in many nonlinear inverse scattering methods.³¹

For example, a simple implementation of aberration correction can be derived if one makes the assumption that background inhomogeneities result only in cumulative delays (or advances) of the incident and scattered wavefronts. This crude model does not include many propagation and scattering effects important to ultrasonic aberration, but has been shown to provide a reasonable first approximation of local delays in wavefronts propagating through large-scale tissue models.^{32,33} Given this approximation, the total delay for an angle ϕ and a point position \mathbf{r} is given by

$$\delta\tau(\phi, \mathbf{r}) = \int_{\xi} c(\xi)^{-1} d\xi - \frac{R}{c_0}, \quad (23)$$

where the integral is performed along the line that joins the spatial points \mathbf{r} and $R\phi$. Aberration-corrected reconstructions can then be performed using Eq. (18) with τ replaced by the corrected delay term

$$\tau \rightarrow R/c_0 + \frac{(\alpha - \theta) \cdot \mathbf{r}}{c_0} + \delta\tau(\alpha, \mathbf{r}) + \delta\tau(\theta, \mathbf{r}). \quad (24)$$

Improved approximations could be obtained by application of the delay function $\delta\tau(\phi, \mathbf{r})$ after numerical backpropagation of the far-field scattered wavefronts through a homogeneous medium^{34,35} or by compensation for both delay and amplitude variations.^{36,37} More general, although much more computationally expensive, aberration correction could also be performed by synthetic focusing using full-wave numerical computation of acoustic fields within an estimated realization of the unknown medium. A method of this kind has been implemented, within the context of a frequency-domain diffraction tomography method, in Ref. 19.

The present imaging method has been derived using simplifying assumptions including zero absorption and constant density for the scattering medium. However, these assumptions do not substantially restrict the validity of the method. For example, the effect of absorption can be reduced using time-gain compensation, with or without frequency-dependent corrections,³⁸ of received scattered signals for each transmit/receive pair. Such time-gain compensation could be performed either using an estimated bulk attenuation for the medium (as with current clinical ultrasound scanners), or by implementation of an adaptive attenuation model in a manner similar to the time-shift compensation scheme discussed above.

Inclusion of density variations as well as sound speed variations adds additional complication to the time-domain diffraction tomography algorithm derived here. For single-frequency diffraction tomography in the presence of sound speed and density variations, the quantity $\gamma_B(\mathbf{r}, \omega)$ reconstructed by Eq. (8) can be shown³⁹ to provide an estimate of a physical quantity that depends both on sound speed variations and density variations. In the notation used here, this quantity can be written

$$\gamma'(\mathbf{r}) = \gamma(\mathbf{r}) - \gamma(\mathbf{r})\gamma_\rho(\mathbf{r}) + \frac{1}{2k^2} \nabla^2 \gamma_\rho(\mathbf{r}), \quad (25)$$

where the density variation is defined $\gamma_\rho = 1 - \rho_0/\rho(\mathbf{r})$. Thus, for time-domain reconstructions of media with density variations, the reconstruction formula of Eq. (18) will provide the estimate

$$\gamma_M(\mathbf{r}) \approx \gamma(\mathbf{r}) - \gamma(\mathbf{r})\gamma_\rho(\mathbf{r}) + \frac{1}{2k_0^2} \nabla^2 \gamma_\rho(\mathbf{r}), \quad (26)$$

where k_0 is the wave number corresponding to the center frequency of the pulse employed. For media such as human tissue, where density variations are fairly small and abrupt density transitions are rare, the last two terms of Eq. (26) are small compared to $\gamma(\mathbf{r})$, so that the reconstruction algorithm derived above can still be regarded to provide an image of the sound-speed variation function $\gamma(\mathbf{r})$. However, if desired, a reconstruction employing pulses with two distinct center frequencies could allow separation of sound speed and density variations by techniques similar to those described in Ref. 16 or 39.

II. COMPUTATIONAL METHODS

The time-domain inverse scattering method described above has been tested with 2D and 3D synthetic data prepared using three numerical methods: a Born approximation method for point scatterers and 3D slabs, an exact series solution for cylindrical inhomogeneities, and a k -space method for arbitrary 2D inhomogeneous media.

The time-domain waveform employed for all the computations reported here was

$$f(t) = \cos(\omega_0 t) e^{-t^2/(2\sigma^2)}, \quad (27)$$

where $\omega_0 = 2\pi f_0$ for a center frequency of f_0 and σ is the temporal Gaussian parameter. This waveform has the real, even Fourier transform

$$\hat{f}(\omega) = \sqrt{\frac{\sigma^2}{8\pi}} (e^{-\sigma^2(\omega - \omega_0)^2/2} + e^{-\sigma^2(\omega + \omega_0)^2/2}). \quad (28)$$

Values used for the computations reported here were $f_0 = 2.5$ MHz and $\sigma = 0.25$ μ s, so that the -6 dB bandwidth of the signal was 1.5 MHz. These parameters correspond closely to those of an existing 2048-element ring transducer.⁴⁰

For the case of point scatterers, the contrast function γ was assumed to take the form

$$\gamma(\mathbf{r}) = \sum_j^M \mu_j \delta(\mathbf{r} - \mathbf{r}_j). \quad (29)$$

Using the far-field form of the 2D Green's function and neglecting multiple scattering, Eq. (6) for the scattered far field can be rewritten as

$$\hat{p}_s(\theta, \alpha, \omega) = -k^2 \sqrt{\frac{i}{8\pi k R}} \hat{f}(\omega) \sum_j \mu_j e^{ik(\alpha - \theta) \cdot \mathbf{r}_j} \quad (30)$$

for each frequency component of interest. Time-domain waveforms were synthesized by using Eq. (30) for each frequency with $\hat{f}(\omega) > 10^{-3}$ and inverting the frequency-domain scattered wavefield by a fast Fourier transform (FFT) implementation of Eq. (4). The temporal sampling rate employed was 10 MHz. An analogous formula, with a different multiplicative constant, was also employed for the 3D case.

The Born approximation was also used to compute three-dimensional scattering for slab-shaped objects defined by the equation

$$\gamma(\mathbf{r}) = \gamma_0 H(a_x - |x|) H(a_y - |y|) H(a_z - |z|). \quad (31)$$

For this object, the linearized forward problem can be solved analytically. Under the Born approximation, the frequency-domain scattered far field has the form

$$\begin{aligned} \hat{p}_s(\theta, \alpha, \omega) = & 2\hat{f}(\omega) \gamma_0 a_x a_y a_z e^{ikR}/(\pi R) \\ & \times \frac{\sin[kL_x(\alpha - \theta) \cdot \mathbf{e}_x]}{kL_x(\alpha - \theta) \cdot \mathbf{e}_x} \frac{\sin[kL_y(\alpha - \theta) \cdot \mathbf{e}_y]}{kL_y(\alpha - \theta) \cdot \mathbf{e}_y} \\ & \times \frac{\sin[kL_z(\alpha - \theta) \cdot \mathbf{e}_z]}{kL_z(\alpha - \theta) \cdot \mathbf{e}_z}, \end{aligned} \quad (32)$$

where \mathbf{e}_x , \mathbf{e}_y , and \mathbf{e}_z represent unit vectors in the x , y , and z directions. The time domain scattered pressure $p_s(\theta, \alpha, t)$ is

obtained, as for the point scatterer case described above, by inverse transformation of the frequency-domain wavefield for all frequencies within the bandwidth of interest.

For 2D cylindrical inhomogeneities, an analogous procedure was followed, except that the frequency-domain scattered wavefield $\hat{p}_s(\theta, \alpha, \omega)$ was computed using an exact series solution²⁵ for each frequency component of interest. In implementation of the series solution, summations were truncated when the magnitude of a single coefficient dropped below 10^{-12} times the sum of all coefficients.

Solutions were also obtained for arbitrary 2D inhomogeneous media using a time-domain k -space method.⁴¹ Grid sizes of 256×256 points, a spatial step of 0.0833 mm, and a time step of 0.02734 μ s were employed. Scattered acoustic pressure signals on a circle of virtual receivers were recorded at a sampling rate of 9.144 MHz. The receiver circle, which had a radius of 3.0 mm in these computations, completely contained the inhomogeneities used. Far-field waveforms were computed by Fourier transforming the time-domain waveforms on the near-field measurement circle, transforming these to far-field waveforms for each frequency using a numerically exact transformation method,¹⁶ and performing inverse Fourier transformation to yield time-domain far-field waveforms. All forward and inverse temporal Fourier transforms, as well as angular transforms occurring in the near-field-far-field transformation,¹⁶ were performed by FFT.

The time-domain imaging method was directly implemented using Eq. (18), evaluated using straightforward numerical integration over all incident-wave and measurement directions employed. The reconstruction formula employed can be explicitly written as

$$\gamma_M(\mathbf{r}) = \frac{1}{N_{2D}} \int_0^{2\pi} \int_0^{2\pi} |\sin(\alpha - \theta)| \left(p_s(\theta, \alpha, \tau) + i\mathbf{H}^{-1}[p_s(\theta, \alpha, \tau)] \right) d\alpha d\theta, \quad (33)$$

$$\tau = R/c_0 + \frac{(\cos \alpha - \cos \theta) \cdot x + (\sin \alpha - \sin \theta) \cdot y}{c_0}$$

for the 2D case, where α and θ are the angles corresponding to the direction vectors α and θ , and as

$$\gamma_M(\mathbf{r}) = \frac{1}{N_{3D}} \int_0^{2\pi} \int_0^\pi \int_0^{2\pi} \int_0^\pi |\alpha - \theta| \left(p_s(\theta, \alpha, \tau) + i\mathbf{H}^{-1}[p_s(\theta, \alpha, \tau)] \right) \sin(\Phi_\alpha) \sin(\Phi_\theta) d\Phi_\alpha$$

$$\times d\Theta_\alpha d\Phi_\theta d\Theta_\theta,$$

$$\tau = R/c_0 + \frac{(\alpha - \theta) \cdot \mathbf{r}}{c_0}, \quad (34)$$

$$\alpha - \theta = (\cos \Theta_\alpha \sin \Phi_\alpha - \cos \Theta_\theta \sin \Phi_\theta) \cdot \mathbf{e}_x$$

$$+ (\sin \Theta_\alpha \sin \Phi_\alpha - \sin \Theta_\theta \sin \Phi_\theta) \cdot \mathbf{e}_y$$

$$+ (\cos \Phi_\alpha - \cos \Phi_\theta) \cdot \mathbf{e}_z$$

for the 3D case, where Θ_α and Φ_α are direction angles for the incident-wave direction α and Θ_θ and Φ_θ are direction

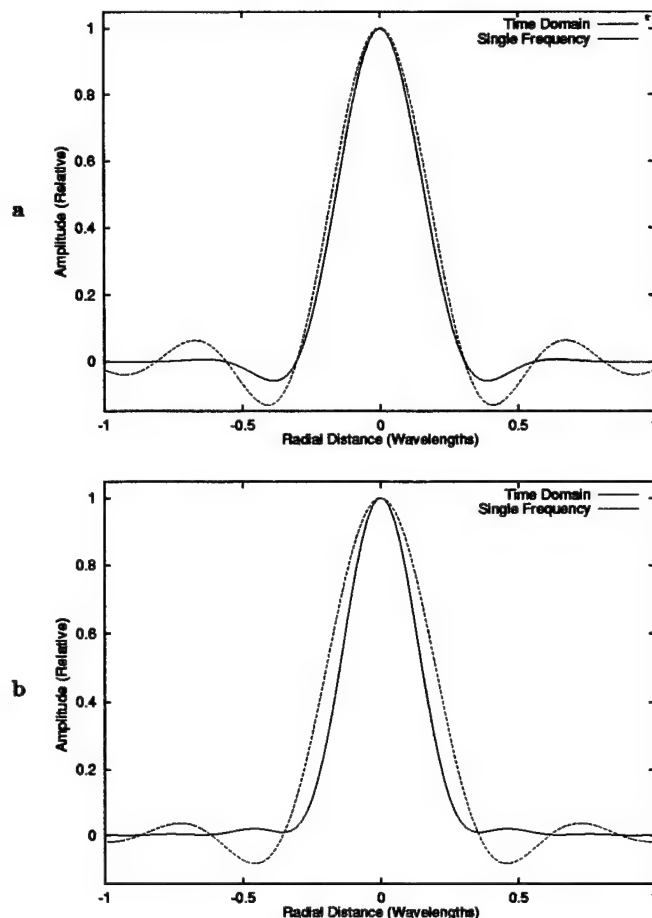


FIG. 2. Point-spread functions for time-domain and single-frequency diffraction tomography methods. In each panel, the vertical scale corresponds to the relative amplitude of the reconstructed contrast $\gamma(\mathbf{r})$, while the horizontal scale corresponds to number of wavelengths at the center frequency. (a) Two-dimensional case. (b) Three-dimensional case.

angles for the measurement direction θ . For each case, the normalization factor N was determined from Eq. (11) with $\hat{g}(\omega) = \hat{f}(\omega)/\hat{\mu}(\omega)$ and $\mu(\omega)$ given by Eq. (9). Before evaluation of the argument τ for each signal, the time-domain waveforms were resampled at a sampling rate of 16 times the original rate. This resampling was performed using FFT-based Fourier interpolation. The inverse Hilbert transform was performed for each signal using an FFT implementation of Eq. (16). Values of the pressure signals at the time τ were then determined using linear interpolation between samples of the resampled waveforms. The integrals of Eqs. (33) and (34) were implemented using discrete summation over all transmission and measurement directions employed.

Computations were also performed using the time-domain diffraction tomography algorithm for limited-aperture data. For these reconstructions, the integrals of Eq. (33) were evaluated only for angles corresponding to transmitters and receivers within a specified aperture of angular width ϕ_{ap} , i.e.,

$$|\alpha| \leq \phi_{ap}/2, \quad |\theta - \pi| \leq \phi_{ap}/2. \quad (35)$$

Use of a small value for ϕ_{ap} corresponds to use of a small aperture in pulse-echo mode.

III. NUMERICAL RESULTS

Two-dimensional and three-dimensional point-spread functions (PSF) for the present time-domain diffraction tomography method are illustrated in Fig. 2. The time-domain reconstructions shown here, like the other time-domain reconstructions shown in this paper, were obtained using an incident pulse of center frequency 2.5 MHz and a Gaussian envelope corresponding to a -6 dB bandwidth of 1.5 MHz. Point-spread functions were determined by reconstructing a point scatterer located at the origin. For the 2D case, in which the point scatterer can be regarded as a thin wire, synthetic scattering data was obtained using the Born approximation method outlined above for 16 incident-wave directions and 64 measurement directions. The 3D time-domain reconstruction was obtained using Born data for 72 incident-wave directions and 288 measurement directions, each evenly spaced on a rectangular grid defined by the angles Θ and Φ . For comparison, analogous point-spread functions are also shown for standard frequency-domain diffraction tomography reconstructions using single-frequency (2.5 MHz) data.

For the 2D case illustrated in Fig. 2, the time-domain PSF has a slightly narrower peak, indicating that point resolution has been slightly improved by the increased bandwidth employed in the time domain method. More significantly, sidelobes of the time-domain PSF are significantly smaller than those for the single-frequency PSF (the first sidelobe is reduced by 7 dB, while the second is reduced by 19 dB), so that contrast resolution for time-domain diffraction tomography is seen to be much higher than for single-frequency diffraction tomography. For the 3D case, the time-domain reconstruction shows a much more dramatic improvement over the single-frequency reconstruction. In this case, the time-domain solution shows significant increases in both the point resolution (PSF width at half-maximum reduced by 27%) and contrast resolution (first sidelobe reduced by 13 dB and second sidelobe reduced by 18 dB). Furthermore, a comparison of the PSFs for 2D and 3D time-domain reconstruction indicates that much higher image quality is achievable for 3D time-domain imaging than for the 2D case. This increase in image quality suggests that the time-domain diffraction tomography method proposed here may benefit from the overdetermined nature of the general wideband 3D inverse scattering problem.^{42,43}

The effect of transmit and receive aperture characteristics on image quality is illustrated in Fig. 3. Panels (a) and (b) of Fig. 3 show the point-spread function for a number of aperture configurations, each employing 64 measurement directions. Figure 3(a) shows the point-spread function for reconstructions obtained using 1, 4, 8, and 16 incident-wave directions. The point scatterer is clearly imaged even for the reconstruction using one incident-wave direction. Optimal image quality (indistinguishable from reconstructions with 64 incident-wave directions) is obtained for 16 incident-wave directions, so that scattering data obtained using one incident-wave direction for each group of four measurement directions appears to be sufficient for the present reconstruction method.

The effect of limited view range on the point spread

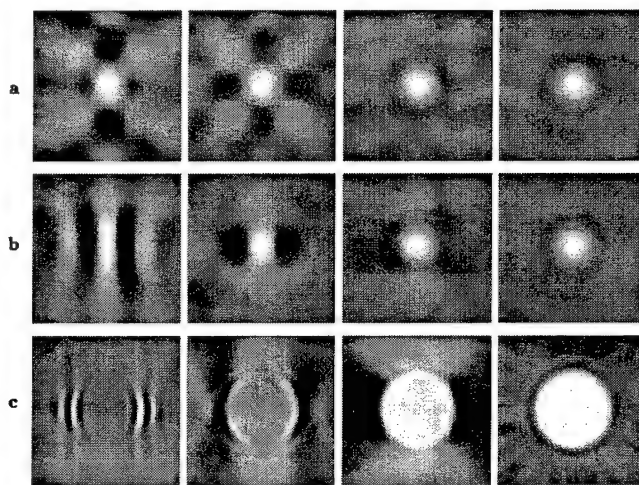


FIG. 3. Effect of aperture characteristics on image quality. Each panel shows the real part of a time-domain reconstruction, $\text{Re}[\gamma_M]$, on a linear grayscale with white representing the maximum amplitude of $|\gamma_M(\mathbf{r})|$ and black represents -1 times the maximum amplitude. (a) Point-spread functions for the same waveform parameters as Fig. 2. Each panel shows an area of 0.6×0.6 mm², corresponding to one square wavelength at the center frequency. Left to right: 1, 4, 8, and 16 incident-wave directions. (b) Point-spread functions for aperture sizes of $\pi/2$, π , $3\pi/2$, and 2π radians, format as in previous panel. (c) Real parts of reconstructions for a homogeneous cylinder ($a = 1.0$ mm, $\gamma = 0.02$). The area shown in each panel is 2.0×2.0 mm². Left to right: aperture sizes of $\pi/2$, π , $3\pi/2$, and 2π radians.

function is also illustrated in Fig. 3. Panel (b) shows the point-spread function for four differently limited apertures, while panel (c) shows reconstructions of a homogeneous cylinder ($a = 1.0$ mm, $\gamma = 0.02$) for the same apertures. In each case, limitation of the transmit and receive apertures to angles near the backscatter direction (aperture size $\pi/2$) results in images that resemble a conventional B-scans. Use of apertures corresponding to pulse-echo mode in the large-aperture limit (aperture size π) yield higher resolution in all directions. Using three-fourths of a circular aperture (size $3\pi/2$) yields image quality close to that for the full aperture (2π) case. The characteristics of all these images result from the set of spatial-frequency vectors interrogated by each group of scattering measurements.¹ Apertures with only a limited range of transmit and receive directions [e.g., the "b-scan" apertures shown in the first column of panels (b) and (c)] provide only information corresponding to large spatial frequency vectors oriented nearly on-axis, so that such images mainly show those edges that are nearly perpendicular to the axis of the aperture.

Reconstructions performed using exact solutions for scattering from cylindrical inhomogeneities provide a straightforward means to assess the accuracy of the time-domain scattering method for a range of object sizes and contrasts. A number of example reconstructions are shown in Figs. 4 and 5. The number of measurement directions for all cylinder reconstructions was chosen based on an empirical test of the number required for a satisfactory image of a homogeneous cylinder; for a cylinder of radius 1 mm, the required number of measurement directions was determined to be approximately 96. Based on spatial-frequency sampling considerations, the number of measurement directions was increased in proportion to the size of the inhomogeneous

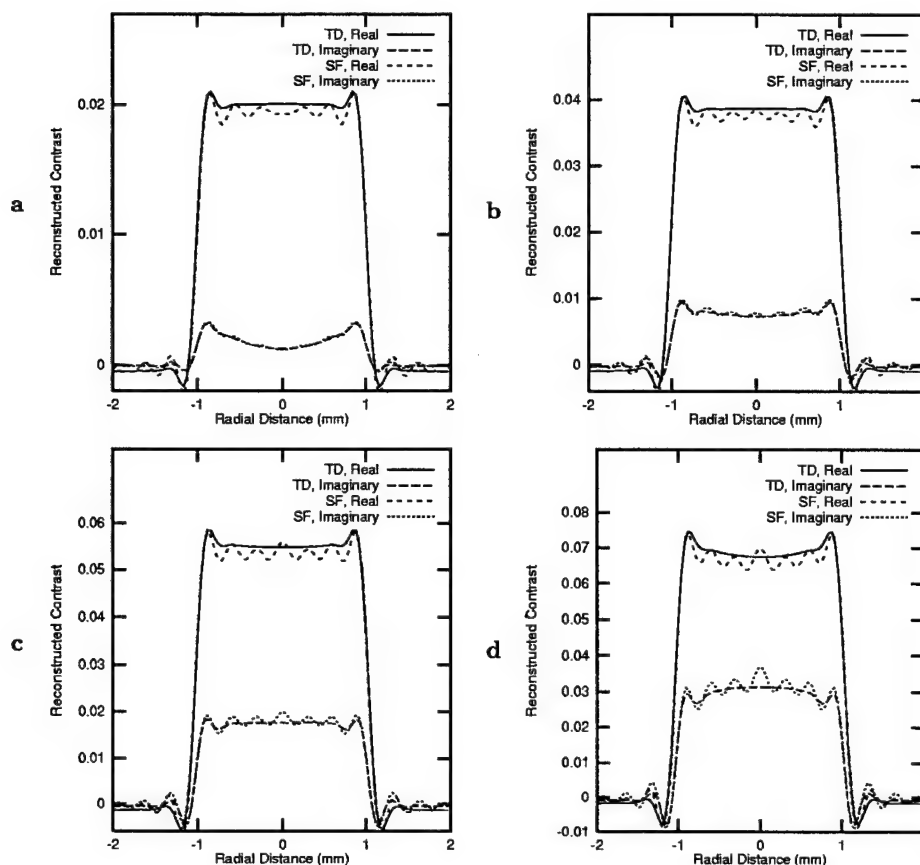


FIG. 4. Cross sections of reconstructed contrast functions $\gamma(r)$ for a cylinder of radius 1 mm, using time-domain (TD) and single-frequency (SF) diffraction tomography. Waveform parameters are as in Fig. 1. (a) $\gamma=0.02$. (b) $\gamma=0.04$. (c) $\gamma=0.06$. (d) $\gamma=0.08$.

region to be reconstructed. Since the results shown in Fig. 3 indicate that considerably fewer incident-wave directions than measurement directions are needed, the number of incident directions was chosen to be one-quarter the number of measurement directions in each case.

Cross sections of time-domain and single-frequency reconstructions, plotted in Fig. 4, show the relative accuracy of each reconstruction method for a cylinder of 1-mm radius and purely real contrast ranging from $\gamma=0.02$ to $\gamma=0.08$. For the synthetic scattering data in each case, 96 measurement directions and 24 incident-wave directions were employed. The time-domain reconstructions show improvement over the single-frequency reconstructions both in improved contrast resolution (smaller sidelobes outside the support of the cylinder) and in decreased ringing (Gibbs phenomenon) artifacts within the support of the cylinder. However, for increasing contrast values, both methods show similar increases in phase error, as indicated by increased imaginary parts of the reconstructed contrast. This error results from the Born approximation, which is based on the assumption that the incident wave propagates through the inhomogeneous medium without distortion. Perturbations in the local arrival time of the incident wavefront, which are more severe for higher contrasts and larger inhomogeneities, can result in a scattered field that is phase shifted relative to the ideal case assumed in the Born approximation; linear inversion of this phase-distorted data naturally results in a phase-distorted reconstruction of the scattering medium. (A complementary

explanation of this phase error, based on the unitarity of the scattering operator, is given in Ref. 19.)

A test of image fidelity for the time-domain reconstruction method is shown in Fig. 5. The real parts of time-domain reconstructions are shown as grayscale images for homogeneous cylinders with radii between 1 and 4 mm and contrasts between $\gamma=0.02$ and $\gamma=0.08$. The number of measurement directions employed for the synthetic scattering data was 96 for the 1-mm radius cylinders, 192 for the 2-mm cylinders, 288 for the 3-mm cylinders, and 384 for the 4-mm cylinders. In each case, four incident-wave directions per measurement direction were used. The first row of this figure corresponds to the time-domain reconstructions shown in Fig. 4.

The images shown in Fig. 5 provide a basis for evaluating the ability of the present time-domain diffraction tomography method to image homogeneous objects of various sizes and contrasts. In this figure, images of $\text{Re}[\gamma_M]$ show uniform quality for small cylinder sizes and contrasts, but poorer image quality for larger sizes and contrasts. For the largest size and contrast employed ($a=4.0$ mm, $\gamma=0.08$), the reconstruction primarily shows the edges of the cylinder and fails to image the interior. Particularly notable is that the "matrix" of images in Fig. 5 is nearly diagonal; that is, a linear increase in object contrast causes image degradation comparable to a corresponding linear increase in object size. Thus, a nondimensional parameter directly relevant to image quality for homogeneous objects is $ka\gamma$, where k is a domi-

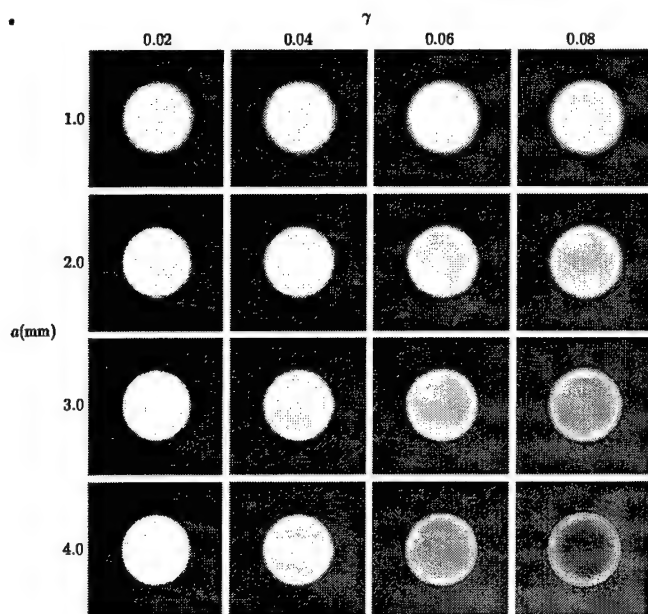


FIG. 5. Images of time-domain reconstructions for cylinders of varying radius a and contrast γ . Each panel shows the real part of the reconstructed contrast, $\text{Re}[\gamma_M(\mathbf{r})]$, for a pulse of center frequency 2.5 MHz and -6 dB bandwidth 1.5 MHz. The area shown in each panel is $2a \times 2a$. All images are shown on a linear, bipolar gray scale where white represents the maximum amplitude of $|\gamma_M(\mathbf{r})|$ and black represents -1 times the maximum amplitude.

nant wave number, a is the object radius, and γ is the object contrast. Using the wave number $k_0 = 10.472$ rad/mm corresponding to the center frequency of 2.5 MHz and a sound speed of 1.5 mm/ μ s, the reconstructions shown in Fig. 5 indicate that the interior of the cylinder is imaged satisfactorily for the approximate range ka $\gamma < 2.5$. This result is consistent with a previous study of single-frequency diffraction tomography, in which adequate Born reconstructions of cylinders were obtained for the parameter range ka $\gamma \leq 2.2$.⁴⁴

Reconstructions for several scattering objects without special symmetry are shown in Fig. 6. All of these reconstructions were performed using synthetic data produced by the k -space method described in Ref. 41. Synthetic scattering data were computed for 64 incident-wave directions and 256 measurement directions in each case. The first panel shows a reconstruction of a cylinder of radius 2.5 mm and contrast $\gamma = -0.0295$ with an internal cylinder of radius 0.2 mm and contrast $\gamma = 0.0632$. These contrast values correspond, based on tissue parameters given in Ref. 32, to the sound-speed contrasts of human skeletal muscle for the outer cylinder and of human fat for the inner cylinder. The second panel shows a reconstruction of a 2.5-mm-radius cylinder with random internal structure. The third reconstruction shown employed a portion of a chest wall tissue map from Ref. 45. In this case, the synthetic data was obtained using a tissue model⁴⁵ that incorporates both sound speed and density variations, so that the reconstructed quantity is given by Eq. (26). In Fig. 6(c), black denotes connective tissue ($\gamma = -0.1073$, $\gamma_\rho = 0.1134$), dark gray denotes muscle ($\gamma = -0.0295$, $\gamma_\rho = 0.0543$), and light gray denotes fat ($\gamma = 0.0632$, $\gamma_\rho = -0.0453$).

The real part of each reconstruction in Fig. 6 shows

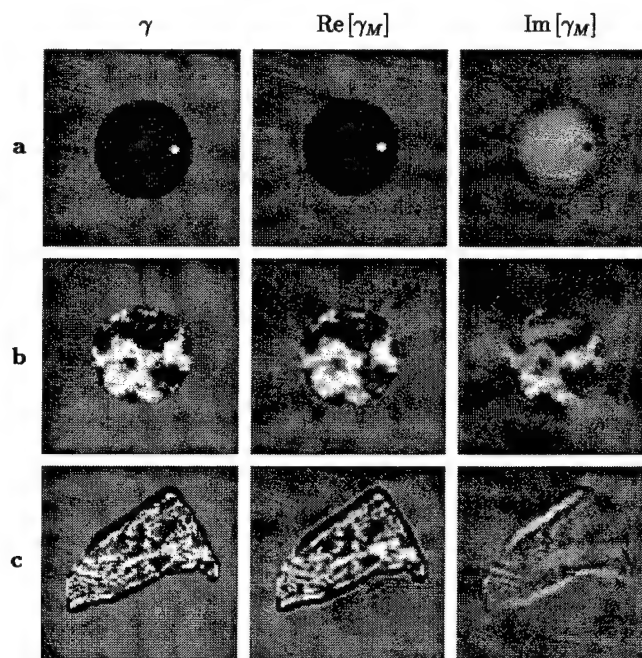


FIG. 6. Time-domain reconstructions from full-wave synthetic data for three arbitrary scattering objects. Each row shows the actual (purely real) contrast function γ together with the real and imaginary parts of the reconstructed contrast function γ_M , using the same linear bipolar gray scale for each panel. Each panel shows a reconstruction area of 5×5 mm². (a) Cylinder, radius 2.5 mm, with an internal cylinder of radius 0.2 mm. (b) Cylinder, radius 2.5 mm, with random internal structure. (c) Tissue structure, with variable sound speed and density, from chest wall cross section 5L in Ref. 45.

good image quality, with high resolution and very little evidence of artifacts. Particularly notable is the accurately detailed imaging of internal structure for the random cylinder and the chest wall cross section. As expected, the density variations present in the chest wall cross section have not greatly affected the image appearance; there is, however, a slight edge enhancement, associated with the Laplacian term in Eq. (26), at boundaries between tissue regions. Also notable is the nearly complete absence of any artifacts outside the scatterer in each case; this result indicates that high contrast resolution has been achieved. However, in each case, the imaginary part of the reconstruction is nonzero, indicating that the Born approximation is not fully applicable. The imaginary parts of each reconstruction are, however, small compared to the real parts. Thus, simple aberration correction methods [of which one example is given by Eq. (24)] could substantially reduce this phase error, as for multiple-frequency diffraction tomography in Ref. 19.

Three-dimensional reconstructions of a homogeneous slab are shown in Fig. 7. The scatterer is characterized by Eq. (31) with $\gamma_0 = 0.01$, $a_x = 0.5$ mm, $a_y = 1.0$ mm, and $a_z = 1.5$ mm. Synthetic data was computed using Eq. (34) for 288 incident-wave directions and 1152 measurement directions, each evenly spaced in the angles Φ and Θ . Signal parameters were as for the examples above, except that the initial sampling rate for the time-domain signals was 9.0 MHz. Iso-surface renderings of the real part of γ_M are shown for the surfaces $\gamma_M = 0.0025$. Since the scattering data were obtained using a Born approximation for the 3D case, the

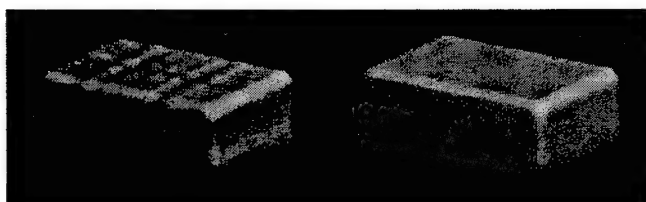


FIG. 7. Three-dimensional reconstructions of a uniform slab with contrast $\gamma=0.01$. Each reconstruction shows an isosurface rendering of the surface $\gamma_M=0.0025$. Left: single-frequency reconstruction. Right: time-domain reconstruction.

imaginary part of each reconstruction is identically zero for both reconstructions. Consistent with the point-spread functions shown in Fig. 2, the time-domain reconstruction is much more accurate than the single-frequency reconstruction. While the single-frequency reconstruction shows an erroneously rippled surface, the time-domain reconstruction is smooth. The time-domain reconstruction is nearly identical to the original object except for some rounding of the sharp edges due to the limited high-frequency content of the signal employed. The length scale of the rounded edges is on the order of one-half the wavelength of the highest frequency in the pulse, i.e., about 0.2 mm for the -6 -dB cutoff of 3.25 MHz.

Since three-dimensional inverse scattering is a computationally demanding problem, comparison of computational efficiency for single-frequency and time-domain methods is of interest. For both reconstructions shown in Fig. 7, identical discretizations of the reconstructed medium were employed. Both computations included solution of the applicable linearized forward problem as well as the inverse problem. Nonetheless, the time-domain method was more efficient than the single-frequency method; the total CPU time required on a 200-MHz AMD K6 processor was 133.3 CPU min for the time-domain method and 287.4 CPU min for the single-frequency method. This gain in efficiency was possible because the greatest computational expense occurred in the "backpropagation" of the signals for each reconstruction point. For the single-frequency method, this step required evaluation of complex exponentials for each incident-wave direction, measurement direction, and spatial point. For the time-domain method, however, the computationally intensive steps (including the forward problem solution and Fourier interpolation of the scattered signals) needed only to be performed once for each transmit/receive pair. For the backpropagation step, performed at each point in the 3D spatial grid, the time-domain reconstruction method required only linear interpolation of the oversampled farfield pressure waveforms.

IV. CONCLUSIONS

A new method for time-domain ultrasound diffraction tomography has been presented. The method provides quantitative images of sound speed variations in unknown media; when two pulse center frequencies are employed, the method is also capable of imaging density variations. Reconstructions performed using this method are equivalent to multiple-

frequency reconstructions using filtered backpropagation, but can be obtained with much greater efficiency.

The time-domain reconstruction algorithm has been derived as a simple filtered delay-and-sum operation applied to far-field scattered signals. This algorithm is closely related to time-domain confocal synthetic aperture imaging, so that it can be considered a generalization of imaging algorithms employed in current clinical instruments. The simplicity of the imaging algorithm allows straightforward addition of features such as time-gain compensation and aberration correction.

Numerical results obtained using synthetic data for 2D and 3D scattering objects show that the time-domain method can yield significantly higher image quality (and, in some cases, also greater efficiency) than single-frequency diffraction tomography. Quantitative reconstructions, obtained using signal parameters comparable to those for present-day clinical instruments, show accurate imaging of objects with simple deterministic structure, random internal structure, and structure based on a cross-sectional tissue model. The method is hoped to be useful for diagnostic imaging problems such as the detection and characterization of lesions in ultrasonic mammography.

ACKNOWLEDGMENTS

This research was funded by the Breast Cancer Research Program of the U.S. Army Medical Research and Material Command, under Grant No. DAMD17-98-1-8141. The author is grateful for helpful discussions with Adrian I. Nachman, Feng Lin, and Robert C. Waag.

- ¹E. Wolf, "Three-dimensional structure determination of semi-transparent objects from holographic data," *Opt. Commun.* **1**, 153-156 (1969).
- ²A. J. Devaney, "A filtered backpropagation algorithm for diffraction tomography," *Ultrason. Imaging* **4**, 336-350 (1982).
- ³D. T. Borup, S. A. Johnson, W. W. Kim, and M. J. Berggren, "Nonperturbative diffraction tomography via Gauss-Newton iteration applied to the scattering integral equation," *Ultrason. Imaging* **14**, 69-85 (1992).
- ⁴S. Gutman and M. Klibanov, "Two versions of quasi-Newton method for multidimensional inverse scattering problem," *J. Comput. Acoust.* **1**, 197-228 (1993).
- ⁵F. W. Kremkau, *Diagnostic Ultrasound: Physical Principles and Exercises* (Grune and Stratton, New York, 1980).
- ⁶J. L. Schwartz and B. D. Steinberg, "Ultrasparse, ultrawideband arrays," *IEEE Trans. Ultrason. Ferroelectr. Freq. Control* **45**, 376-393 (1998).
- ⁷S. H. Maslak, "Computed sonography," in *Ultrasound Annual 1985* (Raven, New York, 1985), pp. 1-16.
- ⁸E. L. Madsen, B. S. Garra, J. A. Parks, A. C. Skelly, and J. A. Zagzebski, *AIUM Quality Control Manual for Gray-Scale Ultrasound Scanners* (American Institute of Ultrasound in Medicine, Laurel, MD, 1995).
- ⁹S. J. Norton, "Reconstruction of a two-dimensional reflecting medium over a circular domain: exact solution," *J. Acoust. Soc. Am.* **67**, 1266-1273 (1980).
- ¹⁰S. J. Norton and M. Linzer, "Ultrasonic reflectivity imaging in three dimensions: exact inverse scattering solutions for plane, cylindrical, and circular apertures," *IEEE Trans. Biomed. Eng.* **28**, 202-220 (1980).
- ¹¹J. H. Kim, S. B. Park, and S. A. Johnson, "Tomographic imaging of ultrasonic reflectivity with correction for acoustic speed variations," *Ultrason. Imaging* **6**, 304-312 (1984).
- ¹²C. Q. Lan and W. Xiong, "An iterative method of ultrasonic reflection mode tomography," *IEEE Trans. Med. Imaging* **13**, 419-425 (1994).
- ¹³D. Miller, M. Oristaglio, and G. Beylkin, "A new slant on seismic imaging: migration and internal geometry," *Geophysics* **52**, 943-964 (1987).

- ¹⁴T. Melamed, Y. Ehrlich, and E. Heymann, "Short-pulse inversion of inhomogeneous media: a time-domain diffraction tomography," *Inverse Probl.* **12**, 977-993 (1996).
- ¹⁵S. Pourjavid and O. Tretiak, "Ultrasound imaging through time-domain diffraction tomography," *IEEE Trans. Ultrason. Ferroelectr. Freq. Control* **38**, 74-85 (1991).
- ¹⁶A. Witten, J. Tuggle, and R. C. Waag, "A practical approach to ultrasonic imaging using diffraction tomography," *J. Acoust. Soc. Am.* **83**, 1645-1652 (1988).
- ¹⁷T. J. Cavicchi and W. D. O'Brien, "Numerical study of higher-order diffraction tomography via the sinc basis moment method," *Ultrason. Imaging* **11**, 42-74 (1989).
- ¹⁸H. Gan, R. Ludwig, and P. L. Levin, "Nonlinear diffractive inverse scattering for multiple scattering in inhomogeneous acoustic background media," *J. Acoust. Soc. Am.* **97**, 764-776 (1995).
- ¹⁹T. D. Mast, A. I. Nachman, and R. C. Waag, "Focusing and imaging using eigenfunctions of the scattering operator," *J. Acoust. Soc. Am.* **102**, 715-725 (1997).
- ²⁰J. M. Blackledge, R. E. Burge, K. I. Hopcraft, and R. J. Wombell, "Quantitative diffraction tomography: I. Pulsed acoustic fields," *J. Phys. D* **20**, 1-10 (1987).
- ²¹S. Mensah and J.-P. Lefebvre, "Enhanced compressibility tomography," *IEEE Trans. Ultrason. Ferroelectr. Freq. Control* **44**, 1245-1252 (1997).
- ²²G. Prokoph and H. Ermert, "A comparison of broadband holographic and tomographic imaging concepts," *Acoust. Imaging* **18**, 381-390 (1991).
- ²³V. A. Burov and O. D. Rumyantseva, "Linearized inverse problem of scattering in monochromatic and pulse modes," *Acoust. Phys.* **40**, 34-42 (1996).
- ²⁴F. Lin, A. I. Nachman, and R. C. Waag, "Quantitative imaging using a time-domain eigenfunction method," submitted to *J. Acoust. Soc. Am.* (1999).
- ²⁵P. M. Morse and K. U. Ingard, *Theoretical Acoustics* (New York, McGraw-Hill, 1968), Chap. 8.
- ²⁶P. M. Morse and H. Feshbach, *Methods of Theoretical Physics* (McGraw-Hill, New York, 1953), Vol. I.
- ²⁷G. Beylkin, "The fundamental identity for iterated spherical means and the inversion formula for diffraction tomography and inverse scattering," *J. Math. Phys.* **24**, 1399-1400 (1982).
- ²⁸A. Papoulis, *The Fourier Integral and Its Applications* (McGraw-Hill, New York, 1962), Chap. 10.
- ²⁹J. Ylitalo, E. Alasaarela, and J. Koivukangas, "Ultrasound holographic B-scan imaging," *IEEE Trans. Ultrason. Ferroelectr. Freq. Control* **36**, 376-383 (1989).
- ³⁰K. E. Thomenius, "Evolution of ultrasound beamformers," *Proc. IEEE Ultrason. Symp.* **2**, 1615-1622 (1996).
- ³¹R. Snieder, "A perturbative analysis of non-linear inversion," *Geophys. J. Int.* **101**, 545-556 (1990).
- ³²T. D. Mast, L. M. Hinkelman, M. J. Orr, V. W. Sparrow, and R. C. Waag, "Simulation of ultrasonic pulse propagation through the abdominal wall," *J. Acoust. Soc. Am.* **102**, 1177-1190 (1997) [Erratum: **104**, 1124-1125 (1998)].
- ³³T. D. Mast, L. M. Hinkelman, M. J. Orr, and R. C. Waag, "The effect of abdominal wall morphology on ultrasonic pulse distortion. Part II. Simulations," *J. Acoust. Soc. Am.* **104**, 3651-3664 (1998).
- ³⁴D.-L. Liu and R. C. Waag, "Correction of ultrasonic wavefront distortion using backpropagation and a reference waveform method for time-shift compensation," *J. Acoust. Soc. Am.* **96**, 649-660 (1994).
- ³⁵C. Dorme and M. Fink, "Ultrasonic beam steering through inhomogeneous layers with a time reversal mirror," *IEEE Trans. Ultrason. Ferroelectr. Freq. Control* **43**(1), 167-175 (1996).
- ³⁶S. Kirshnan, P.-C. Li, and M. O'Donnell, "Adaptive compensation for phase and magnitude aberrations," *IEEE Trans. Ultrason. Ferroelectr. Freq. Control* **43**(1), 44-55 (1996).
- ³⁷Q. Zhu and B. D. Steinberg, "Deabberation of incoherent wavefront distortion: an approach toward inverse filtering," *IEEE Trans. Ultrason. Ferroelectr. Freq. Control* **44**, 575-589 (1997).
- ³⁸I. Claesson and G. Salomonsson, "Frequency- and depth-dependent compensation of ultrasonic signals," *IEEE Trans. Ultrason. Ferroelectr. Freq. Control* **35**, 582-592 (1988).
- ³⁹A. J. Devaney, "Variable density acoustics tomography," *J. Acoust. Soc. Am.* **78**, 120-130 (1985).
- ⁴⁰T. T. Jansson, T. D. Mast, and R. C. Waag, "Measurements of differential scattering cross section using a ring transducer," *J. Acoust. Soc. Am.* **103**, 3169-3179 (1998).
- ⁴¹L. P. Souriau, T. D. Mast, D.-L. D. Liu, M. Tabei, A. I. Nachman, and R. C. Waag, "A *k*-space method for large-scale models of wave propagation in tissue," submitted to *IEEE Trans. Ultrason. Ferroelectr. Freq. Control* (1999).
- ⁴²A. Nachman, "Reconstructions from boundary measurements," *Ann. Math.* **128**, 531-576 (1988).
- ⁴³D. Colton and R. Kress, *Inverse Acoustic and Electromagnetic Scattering Theory*, 2nd ed. (Springer-Verlag, Berlin, 1998), Chap. 10.
- ⁴⁴M. Slaney, A. C. Kak, and L. E. Larsen, "Limitations of imaging with first-order diffraction tomography," *IEEE Trans. Microwave Theory Tech.* **32**, 860-874 (1984).
- ⁴⁵T. D. Mast, L. M. Hinkelman, M. J. Orr, and R. C. Waag, "Simulation of ultrasonic pulse propagation, distortion, and attenuation in the human chest wall," submitted to *J. Acoust. Soc. Am.* **106**, 3665-3677 (1999).

Appendix B

Time-Domain Ultrasound Diffraction Tomography

Proceedings of the 2000 IEEE Ultrasonics Symposium

Vol. 2, pp. 1617–1620

Annual Report for DAMD17-98-1-8141, July 2000

Pages 28–31

Time-Domain Ultrasound Diffraction Tomography

T. Douglas Mast,¹ Feng Lin,² and Robert C. Waag^{2,3}

¹Applied Research Laboratory, The Pennsylvania State University, University Park, PA 16802

²Dept. of Electrical Engineering, University of Rochester, Rochester, NY 14627

³Dept. of Radiology, University of Rochester, Rochester, NY 14642

Abstract—A quantitative ultrasonic imaging method employing time-domain scattering data is presented. This method provides tomographic images of medium properties such as the sound speed contrast; these images are equivalent to multiple-frequency filtered-backpropagation reconstructions using all frequencies within the bandwidth of the incident pulse employed. However, image synthesis is performed directly in the time domain using coherent combination of farfield scattered pressure waveforms, delayed and summed to numerically focus on the unknown medium. The time-domain method is more efficient than multiple-frequency diffraction tomography methods, and can, in some cases, be more efficient than single-frequency diffraction tomography. Example reconstructions, obtained using synthetic data for two-dimensional and three-dimensional scattering of wideband pulses as well as measured scattering data from a 2048-element ring transducer, show that the time-domain reconstruction method provides image quality superior to single-frequency reconstructions for objects of size and contrast relevant to medical imaging problems such as ultrasonic mammography. The present method is closely related to existing synthetic-aperture imaging methods such as those employed in clinical ultrasound scanners. Thus, the new method can be extended to incorporate available image-enhancement techniques such as time-gain compensation to correct for medium absorption and aberration correction methods to reduce error associated with weak scattering approximations.

I. INTRODUCTION

Quantitative imaging of tissue properties is a potentially useful technique for diagnosis of cancer and other disease. Inverse scattering methods such as diffraction tomography can provide quantitative reconstruction of tissue properties including sound speed, density, and absorption. However, although previous inverse scattering methods have achieved high resolution and quantitative accuracy, such methods have not yet been incorporated into commercially successful medical ultrasound imaging systems. Previous methods of diffraction tomography have usually been based on single-frequency scattering, while current diagnostic ultrasound scanners employ wideband time-domain signals. The use of wideband information in image reconstruction is known to provide increased point and contrast resolution, both of which are important for medical diagnosis.

Relatively few previous workers have investigated direct use of wideband scattering data for inverse scattering methods analogous to single-frequency diffraction tomography. A review of several approaches is given in Ref. [1], including linear and nonlinear diffraction tomography methods using scattering data for a number of discrete frequencies [2]–[4], a direct (but not completely general) time-domain reconstruction algorithm [5], and an extension of the eigenfunction method from Ref. [4] to use the full bandwidth of the incident pulse waveform [6].

Recently, a new approach to wideband quantitative imaging has been offered: a time-domain inverse scattering

method that overcomes some of the limitations of previous frequency-domain and time-domain quantitative imaging methods [1]. In this paper, the new time-domain diffraction tomography algorithm is briefly reviewed. The capabilities of the method are demonstrated using simulated reconstructions of two-dimensional and three-dimensional scatterers. The practical capability of the method for ultrasonic mammography is then illustrated by reconstructions of tissue-mimicking phantoms from scattering data measured by a 2.5 MHz, 2048-element ring transducer.

II. THEORY

A new time-domain inverse scattering algorithm, applicable to quantitative imaging of tissue and other inhomogeneous media, is derived in Ref. [1] and summarized briefly below. The medium is modeled as a fluid medium defined by the sound speed contrast function $\gamma(\mathbf{r}) = c_0^2/c(\mathbf{r})^2 - 1$, where c_0 is a background sound speed and $c(\mathbf{r})$ is the spatially-dependent sound speed defined at all points \mathbf{r} . For the scope of the present paper, the medium is assumed to have constant density, no absorption, and weak scattering characteristics; extensions to the reconstruction algorithm that overcome these limiting assumptions are discussed in Ref. [1].

The medium is subjected to a pulsatile plane wave of the form $p_{\text{inc}}(\mathbf{r}, \alpha, t) = f(t - \mathbf{r} \cdot \alpha/c_0)$, where α is a unit vector in the direction of propagation, f is the time-domain waveform, and c_0 is the background sound speed. The scattered wavefield $p_s(\theta, \alpha, t)$ is measured at a fixed radius R in the farfield, where θ corresponds to the direction unit vector of a receiving transducer element. (Alternatively, if scattering measurements are made in the nearfield, the farfield acoustic pressure can be computed using exact transforms that represent propagation through a homogeneous medium [2].) The farfield scattered pressure, when specified for all incident-wave directions α , measurement directions θ , and times t , comprises the data set to be used for reconstruction of the unknown medium. The inverse scattering problem is to reconstruct the unknown medium contrast $\gamma(\mathbf{r})$ using the scattered field $\hat{p}_s(\theta, \alpha, \omega)$ measured at a fixed radius R .

The starting point for the present time-domain inverse scattering method is single-frequency filtered backpropagation [2], [7], [8]. Under the assumption of weak scattering, such that the Born approximation holds, the solution to the single-frequency inverse scattering problem is given by the formula

$$\gamma_B(\mathbf{r}, \omega) = \frac{\hat{\mu}(\omega) e^{-ikR}}{\hat{f}(\omega)} \iint \Phi(\theta, \alpha) \hat{p}_s(\theta, \alpha, \omega) \times e^{ik(\theta - \alpha) \cdot \mathbf{r}} dS_\alpha dS_\theta, \text{ where} \quad (1)$$

$$\begin{aligned}\hat{\mu}(\omega) &= \sqrt{\frac{kR}{8i\pi^3}}, \Phi(\theta, \alpha) = |\sin(\theta - \alpha)| \text{ in 2D, and} \\ \hat{\mu}(\omega) &= \frac{kR}{4\pi^3}, \Phi(\theta, \alpha) = |\theta - \alpha| \text{ in 3D.}\end{aligned}\quad (2)$$

Each surface integral in Eq. (1) is performed over the entire measurement circle for the 2D case and over the entire measurement sphere for the 3D case. Equation (1) provides an exact solution to the linearized inverse scattering problem for a single frequency component of the scattered wavefield $p_s(\theta, \alpha, t)$. The resulting reconstruction, $\gamma_B(\mathbf{r}, \omega)$, has spatial frequency content limited by the "Ewald sphere" of radius $2k$ in wavespace [9].

To improve upon the single-frequency formulas specified by Eq. (1), one can extend the spatial-frequency content of reconstructions by exploiting wideband scattering information. The method outlined here synthesizes a "multiple-frequency" reconstruction $\gamma_M(\mathbf{r})$ by formally integrating single-frequency reconstructions $\gamma_B(\mathbf{r}, \omega)$ over a range of frequencies ω . A general formula for this approach is

$$\gamma_M(\mathbf{r}) = \frac{\int_0^\infty \hat{g}(\omega) \gamma_B(\mathbf{r}, \omega) d\omega}{\int_0^\infty \hat{g}(\omega) d\omega}, \quad (3)$$

where $\hat{g}(\omega)$ is an appropriate frequency-dependent weighting function. In practice, the weighting function $\hat{g}(\omega)$ is chosen to be bandlimited because (for a given set of physical scattering measurements) the frequency-dependent contrast $\gamma_B(\mathbf{r}, \omega)$ can only be reliably reconstructed for a finite range of frequencies ω associated with the spectra of the incident waves employed. Thus, the integrands in Eq. (3) are nonzero only over the support of $\hat{g}(\omega)$ and the corresponding integrals are finite.

If the frequency weighting function is now specified to incorporate the incident-pulse spectrum as well as the frequency- and dimension-dependent coefficient $\hat{\mu}(\omega)$, such that $g(\omega) = \hat{f}(\omega)/\hat{\mu}(\omega)$, Eq. (3) reduces to the form [1]

$$\begin{aligned}\gamma_M(\mathbf{r}) &= \frac{1}{N} \iint \Phi(\theta, \alpha) (p_s(\theta, \alpha, \tau) \\ &+ i \mathbf{H}^{-1}[p_s(\theta, \alpha, \tau)]) dS_\alpha dS_\theta, \text{ where} \\ \tau &= R/c_0 + \frac{(\alpha - \theta) \cdot \mathbf{r}}{c_0}, \quad N = 2 \int_0^\infty \hat{g}(\omega) d\omega,\end{aligned}\quad (4)$$

and \mathbf{H}^{-1} is the inverse Hilbert transform, also known as a quadrature filter.

Equation (4) is notable in several respects. First, it provides a linearized reconstruction that employs scattering information from the entire signal bandwidth without any frequency decomposition of the scattered wavefield. Second, the delay term τ corresponds exactly to the delay required to construct a focus at the point \mathbf{r} by delaying and summing the scattered wavefield $p_s(\theta, \alpha, t)$ for all measurement directions θ and incident-wave directions α . Thus, the time-domain reconstruction formula given by Eq. (4) can be regarded as a quantitative generalization of confocal time-domain synthetic aperture imaging (e.g., the "gold standard" beamformer of Ref. [10]), in which signals are synthetically delayed and summed for each transmit/receive pair to focus at the image point of interest.

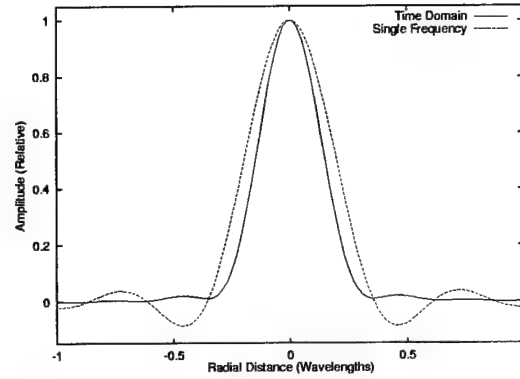


Fig. 1. Point-spread function for three-dimensional time-domain and single-frequency diffraction tomography methods. The vertical scale corresponds to the relative amplitude of the reconstructed contrast $\gamma(\mathbf{r})$, while the horizontal scale corresponds to number of wavelengths at the center frequency.

III. SIMULATIONS

Below, the time-domain diffraction tomography method of Ref. [1] is illustrated using results of simulation tests with 2D and 3D synthetic data. The synthetic scattering data employed were obtained using a Born approximation method for point scatterers and 3D slabs, and a k -space method [11] for arbitrary 2D inhomogeneous media. Additional results, presented in Ref. [1], show reconstructions performed using exact time-domain solutions for scattering from compressible cylinders as well as reconstructions from limited-aperture data. The time-domain waveform employed for all the simulations reported here was $f(t) = \cos(2\pi f_0 t) e^{-t^2/(2\sigma^2)}$, with $f_0 = 2.5$ MHz and $\sigma = 0.25$ μ s, so that the -6 dB bandwidth of the signal was 1.5 MHz. These parameters correspond closely to those of the ring transducer used in the measurements reported in the next section.

The time-domain imaging method was directly implemented using Eq. (4), evaluated using straightforward numerical integration over all incident-wave and measurement directions employed. The synthetic data employed was sampled at rates slightly larger than the Nyquist frequency. Before evaluation of the argument τ for each signal, the time-domain waveforms were Fourier interpolated at a sampling rate of 16 times the original rate. This resampling, as well as the inverse Hilbert transform from Eq. (4), were performed by FFT. Values of the pressure signals at the time τ were then determined using linear interpolation between samples of the resampled waveforms.

A three-dimensional point-spread function (PSF) for the present time-domain diffraction tomography method is illustrated in Fig. 1. The PSF was determined by reconstructing an ideal point scatterer located at the origin. The time-domain reconstruction shows a dramatic improvement over the single-frequency reconstruction, with significant increases in both the point resolution (PSF width at half-maximum reduced by 27%) and contrast resolution (first sidelobe reduced by 13 dB and second sidelobe reduced by 18 dB).

Reconstructions for several arbitrary scattering objects are shown in Fig. 2. All of these reconstructions were performed using synthetic data produced by the k -space method described in Ref. [11]. Synthetic scattering data were computed for 64 incident-wave directions and 256 measure-

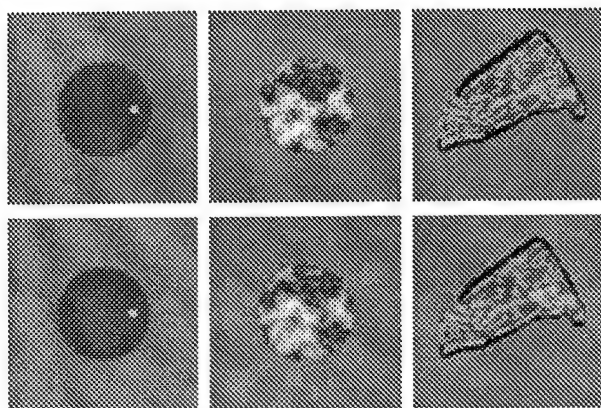


Fig. 2. Time-domain reconstructions from full-wave synthetic data for three arbitrary scattering objects. The upper row shows the contrast function γ for each object, while the lower row shows the real part of the reconstructed contrast γ_M . Each panel shows a reconstruction area of 5 mm \times 5 mm using a linear bipolar gray scale. Left to right: (a) Cylinder, radius 2.5 mm, with an internal cylinder of radius 0.2 mm. (b) Cylinder, radius 2.5 mm, with random internal structure. (c) Tissue structure, with variable sound speed and density, from a chest wall cross section.

ment directions in each case. The first panel shows a reconstruction of a cylinder of radius 2.5 mm and contrast $\gamma = -0.0295$ with an internal cylinder of radius 0.2 mm and contrast $\gamma = 0.0632$. These contrast values correspond, based on tissue parameters given in Ref. [12], to the sound-speed contrasts of human skeletal muscle for the outer cylinder and of human fat for the inner cylinder. The second panel shows a reconstruction of a 2.5 mm-radius cylinder with random internal structure. The third reconstruction shown employed a portion of a chest wall tissue map from Ref. [13]. In this case, the synthetic data was obtained using a tissue model that incorporates both sound speed and density variations, so that the actual reconstructed quantity is slightly different from γ_M [1]. In Fig. 2(c), black denotes connective tissue, dark gray denotes muscle, and light gray denotes fat.

The real part of each reconstruction in Fig. 2 shows good image quality, with high resolution and very little evidence of artifacts. Particularly notable is the accurately detailed imaging of internal structure for the random cylinder and the chest wall cross section. As discussed in Ref. [1], the density variations present in the chest wall cross section have not greatly affected the image appearance; there is, however, a slight edge enhancement at boundaries between tissue regions. Also notable is the nearly-complete absence of any artifacts outside the scatterer in each case; this result indicates that high contrast resolution has been achieved.

Three-dimensional reconstructions of a homogeneous slab with sound speed contrast $\gamma = 0.01$ and dimensions 1 mm \times 2 mm \times 3 mm, are shown in Fig. 3. Synthetic data was computed using a weak scattering approximation for 288 incident-wave directions and 1152 measurement directions, each evenly spaced in the angles Φ and Θ . Isosurface renderings of the real part of the reconstructed γ_M are shown for the surfaces $\gamma_M = 0.0025$. Consistent with the point-spread function shown in Fig. 1, the time-domain reconstruction is much more accurate than the single-frequency reconstruction. While the single-frequency reconstruction shows an erroneously rippled surface, the time-domain reconstruction is smooth. The time-domain reconstruction is nearly identical to the original object except for some round-

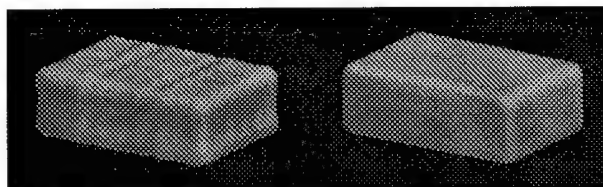


Fig. 3. Three-dimensional reconstructions of a uniform slab with contrast $\gamma = 0.01$. Each reconstruction shows an isosurface rendering of the surface $\gamma_M = 0.0025$. Left: single-frequency reconstruction. Right: time-domain reconstruction.

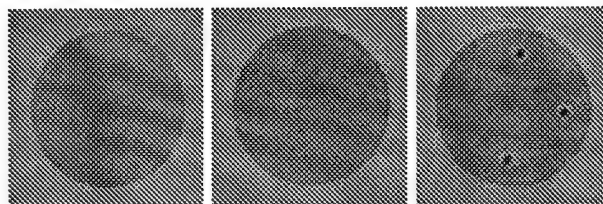


Fig. 4. Reconstructions of three phantoms from measured scattering data. Each panel shows an area of 9 mm \times 9 mm using a bipolar logarithmic scale with a 30 dB dynamic range. Left to right: (a) Homogeneous agar cylinder. (b) Agar with glass spheres. (c) Agar with glass spheres and three nylon filaments.

ing of the sharp edges due to the limited high-frequency content of the signal employed. The length scale of the rounded edges is on the order of one-half the wavelength of the highest frequency in the pulse, *i.e.*, about 0.2 mm for the -6 dB cutoff of 3.25 MHz. Notable is that the time-domain method was more efficient than the single-frequency method in this case; the total CPU time required on a 233 MHz Pentium II processor was 100.0 CPU min for the time-domain method and 233.4 CPU min for the single-frequency method (both computations included solution of the applicable linearized forward problem as well as the inverse problem). This gain in efficiency was possible because the greatest computational expense occurred in the "backpropagation" of the signals, which required evaluation of complex exponentials for the single-frequency method, but only linear interpolation of the oversampled farfield pressure waveforms for the time-domain method.

IV. MEASUREMENTS

The practical capability of the time-domain diffraction tomography method to image tissue-like media has been tested using measured scattering data for three tissue-mimicking phantoms, each of diameter 6 mm. Details of the phantom construction and measurement procedure are given in Ref. [6] and briefly summarized here. The phantoms are primarily composed of agar (nominal sound speed 1510 m/s); one is homogeneous, another contains tiny (subresolution), randomly distributed glass beads, and a third contains three nylon filaments as well as glass beads. Measurements were made using a ring transducer system [14] that consists of 2048 elements, each of which can be used independently as a transmitter or receiver. This fixed transducer configuration avoids signal degradation from phase jitter and excessive scanning time associated with moving transducers. The control electronics associated with the ring transducer provide the capability to program arbitrary transmit waveforms. The element pitch is 0.23 mm, less than one half of the wavelength at the nominal center frequency of 2.5 MHz.

Spatially-limited plane wave pulses were transmitted

from 128 positions equally spaced around the ring. To construct the spatially-limited plane waves, a 4 mm-width cosine rolloff was added to each side of a 10 mm-width uniform central region to provide a smooth transition in amplitude and reduce wavefront spreading. A backpropagation method [15] was then used to obtain the transmit waveforms that produced the desired incident wave.

The incident field (without the scattering object) and the total field (with the scattering object) were measured around the ring for each incident view. To compensate for sound speed changes due to water temperature variations, the background sound speed was tracked using a probe beam during the measurement of both the incident and total fields. The sound speed in the background was estimated from knowledge of the arrival time and the travel distance of the probe beam, which was a spatially limited plane wave directed to the side of the phantom. The resulting speed estimate was used to equalize the time scale of all waveforms. A temperature-compensated incident field $p_i(\theta, \alpha, t)$ was subtracted from the total field $p(\theta, \alpha, t)$ to obtain the scattered field $p_s(\alpha, \theta, t)$. Finally, wavefields were extrapolated to 128 measurement positions at a radius of 7500 mm by an exact spatio-temporal transformation [2], [6].

Far-field scattered waveforms for each incident-wave direction were further processed by a deconvolution operation [1] that compensated for transducer-dependent variations in the incident pulse. The result for each incident-wave direction was an estimate of the scattered farfield pressure associated with an ideal incident pulse of the form $f(t) = \cos(2\pi f_0 t) e^{-t^2/(2\sigma^2)}$, with $f_0 = 2.25$ MHz and $\sigma = 0.25$ μ s. The preprocessed data $p_s(\theta, \alpha, t)$ were then inverted using numerical integration of Eq. (4). The inversion procedure was the same as for the simulations described above, except that the initial sampling rate was 20 MHz and that signals were oversampled to 80 MHz by Fourier interpolation.

Reconstructions for the three phantoms are shown in Fig. 4. Each panel shows good reconstruction quality with a uniform background and high point and contrast resolution as well as quantitative accuracy (similar reconstructions, obtained using an eigenfunction-based inverse scattering method, are presented in Ref. [6]). The subresolution glass spheres do not cause speckle as in pulse-echo B-scan imaging, but instead appear as slight local variations in contrast consistent with weak point scatterers. Both nylon filaments and glass spheres appear dark because higher sound speed corresponds to negative contrast γ as defined above. In panel (c), reconstructions of the nylon wires show slight sidelobe artifacts; these artifacts could be removed by careful choice of an optimal pulse $f(t)$ in the preprocessing of the scattered field [6].

V. CONCLUSIONS

A new method for time-domain ultrasound diffraction tomography has been presented and validated using synthetic and measured scattering data. The method provides quantitative images of sound speed variations in unknown media. These reconstructions are equivalent to multiple-frequency reconstructions using filtered backpropagation, but can be obtained with much greater efficiency. The time-domain reconstruction algorithm has been derived as a simple filtered delay-and-sum operation, closely related to time-domain confocal synthetic aperture imaging, so that it can be considered a generalization of imaging algorithms employed in current clinical instruments. The simplicity of the imaging

algorithm allows straightforward addition of features such as time-gain compensation and aberration correction.

Numerical results obtained using synthetic and measured data show that the time-domain method can yield significantly higher image quality (and, in some cases, also greater efficiency) than single-frequency diffraction tomography. Quantitative reconstructions, obtained using signal parameters comparable to those for present-day clinical instruments, show accurate imaging of objects with simple deterministic structure, random internal structure, and structure based on a cross-sectional tissue model. Reconstructions of tissue-mimicking phantoms suggest that the method will be useful for diagnostic imaging problems such as the detection and characterization of lesions in ultrasonic mammography.

ACKNOWLEDGMENTS

This research was funded by the Breast Cancer Research Program of the U.S. Army Medical Research and Materiel Command, under Grant No. DAMD17-98-1-8141 (TDM), and by NIH Grants DK 45533, HL 50855, and CA 74050, DARPA Grant N00014-96-0749, and the University of Rochester Diagnostic Ultrasound Research Laboratory Industrial Associates (FL and RCW).

REFERENCES

- [1] T. D. Mast, "Wideband quantitative ultrasonic imaging by time-domain diffraction tomography," to appear in *J. Acoust. Soc. Am.* (1999).
- [2] A. Witten, J. Tuggle, and R. C. Waag, "A practical approach to ultrasonic imaging using diffraction tomography," *J. Acoust. Soc. Am.* **83**, 1645-1652 (1988).
- [3] T. J. Cavicchi and W. D. O'Brien, "Numerical study of higher-order diffraction tomography via the sinc basis moment method," *Ultrasonic Imaging* **11**, 42-74 (1989).
- [4] T. D. Mast, A. I. Nachman, and R. C. Waag, "Focusing and imaging using eigenfunctions of the scattering operator," *J. Acoust. Soc. Am.* **102**, 715-725 (1997).
- [5] V. A. Burov and O. D. Rumyantseva, "Linearized inverse problem of scattering in monochromatic and pulse modes," *Acoustical Physics* **40**, 34-42 (1996).
- [6] F. Lin, A. I. Nachman, and R. C. Waag, "Quantitative imaging using a time-domain eigenfunction method," submitted to *J. Acoust. Soc. Am.* (1999).
- [7] A. J. Devaney, "A filtered backpropagation algorithm for diffraction tomography," *Ultrason. Imag.* **4**, 336-350 (1982).
- [8] G. Beylkin, "The fundamental identity for iterated spherical means and the inversion formula for diffraction tomography and inverse scattering," *J. Math. Phys.* **24**, 1399-1400 (1982).
- [9] E. Wolf, "Three-dimensional structure determination of semi-transparent objects from holographic data," *Optics Comm.* **1**, 153-156 (1969).
- [10] K. E. Thomenius, "Evolution of ultrasound beamformers," *Proc. IEEE Ultrason. Symp.* **2**, 1615-1622 (1996).
- [11] L. P. Souriau, T. D. Mast, D.-L. Liu, M. Tabei, A. I. Nachman, and R. C. Waag, "A k -space method for large-scale models of wave propagation in tissue," submitted to *IEEE Trans. Ultrason. Ferroelectr. Freq. Contr.* (1999).
- [12] T. D. Mast, L. M. Hinkelman, M. J. Orr, V. W. Sparrow, and R. C. Waag, "Simulation of ultrasonic pulse propagation through the abdominal wall," *J. Acoust. Soc. Am.* **102**, 1177-1190 (1997).
- [13] T. D. Mast, L. M. Hinkelman, M. J. Orr, and R. C. Waag, "Simulation of ultrasonic pulse propagation, distortion, and attenuation in the human chest wall," submitted to *J. Acoust. Soc. Am.* (1999).
- [14] T. T. Jansson, T. D. Mast, and R. C. Waag, "Measurements of differential scattering cross section using a ring transducer," *J. Acoust. Soc. Am.* **103**, 3169-3179 (1998).
- [15] D.-L. Liu and R. C. Waag, "Propagation and backpropagation for ultrasonic wavefront design," *IEEE Trans. Ultrason., Ferroelectr., Freq. Contr.* **44**, 1-13 (1997).

Appendix C

Simulation of Ultrasonic Pulse Propagation, Distortion,
and Attenuation in the Human Chest Wall

Journal of the Acoustical Society of America **106**, 3665–3677 (1999)

Annual Report for DAMD17-98-1-8141, July 1999

Pages 33–45

Simulation of ultrasonic pulse propagation, distortion, and attenuation in the human chest wall

T. Douglas Mast

Applied Research Laboratory, The Pennsylvania State University, University Park, Pennsylvania 16802

Laura M. Hinkelman^{a)}

Department of Electrical and Computer Engineering, University of Rochester, Rochester, New York 14627

Leon A. Metlay

Department of Pathology and Laboratory Medicine, University of Rochester Medical School, Rochester, New York 14642

Michael J. Orr

Department of Electrical and Computer Engineering, University of Rochester, Rochester, New York 14627

Robert C. Waag

Departments of Electrical and Computer Engineering and Radiology, University of Rochester, Rochester, New York 14627

(Received 5 April 1999; accepted for publication 23 August 1999)

A finite-difference time-domain model for ultrasonic pulse propagation through soft tissue has been extended to incorporate absorption effects as well as longitudinal-wave propagation in cartilage and bone. This extended model has been used to simulate ultrasonic propagation through anatomically detailed representations of chest wall structure. The inhomogeneous chest wall tissue is represented by two-dimensional maps determined by staining chest wall cross sections to distinguish between tissue types, digitally scanning the stained cross sections, and mapping each pixel of the scanned images to fat, muscle, connective tissue, cartilage, or bone. Each pixel of the tissue map is then assigned a sound speed, density, and absorption value determined from published measurements and assumed to be representative of the local tissue type. Computational results for energy level fluctuations and arrival time fluctuations show qualitative agreement with measurements performed on the same specimens, but show significantly less waveform distortion than measurements. Visualization of simulated tissue-ultrasound interactions in the chest wall shows possible mechanisms for image aberration in echocardiography, including effects associated with reflection and diffraction caused by rib structures. A comparison of distortion effects for varying pulse center frequencies shows that, for soft tissue paths through the chest wall, energy level and waveform distortion increase markedly with rising ultrasonic frequency and that arrival-time fluctuations increase to a lesser degree. © 1999 Acoustical Society of America. [S0001-4966(99)03212-9]

PACS numbers: 43.80.Qf, 43.80.Cs, 43.58.Ta, 43.20.Fn [FD]

INTRODUCTION

Echocardiography is widely employed for diagnosis of cardiac diseases including valvular defects, pericardial effusion, and wall motion abnormalities.¹⁻³ Commonly, echocardiography is performed noninvasively through the chest (transthoracic) using an external probe placed on the chest wall. The chest wall, however, can considerably degrade image quality because acoustic paths between the skin and heart may contain ribs and cartilage as well as inhomogeneous muscle and fatty tissue. The result is that as many as 10–30% of patients cannot be successfully imaged with present transthoracic techniques.⁴ This limitation of transthoracic echocardiography has led to the development of transeophageal echocardiography, in which the heart is imaged by a transducer inserted into the esophagus.¹⁻⁴ Although transeophageal echocardiography provides superior image qual-

ity, resulting in high diagnostic sensitivity and specificity, the invasiveness of the procedure is accompanied by increased risk.³⁻⁶ For this reason, improvements in the noninvasive transthoracic approach are desirable, for example, by the development of methods to compensate for image degradation caused by the chest wall.

An understanding of ultrasonic aberration produced by the chest wall is important to the development of appropriate compensation methods for transthoracic ultrasonic imaging. Direct measurements of ultrasonic distortion produced by chest wall specimens^{7,8} have been helpful. Results reported in Ref. 7 show that propagation through the chest wall causes substantial beam distortion. However, that study did not distinguish the effect of soft tissue from effects caused by rib structures. In Ref. 8, a detailed study of distortion caused by soft tissue paths indicates that soft tissue distortion in the chest wall is substantially less than the corresponding distortion in the human abdominal wall. However, distortion caused by ribs was only treated qualitatively in the latter

^{a)}Present address: Department of Meteorology, The Pennsylvania State University, University Park, PA 16802.

study because the physical mechanisms of rib-induced distortion could not be adequately described by the method reported there. Although a model of ultrasound propagation in the chest wall has previously been described,⁹ that model is based on coarse depictions of chest wall morphology including homogeneous tissue layers and evenly-spaced, uniformly-shaped ribs. These previous experiments and simulations, therefore, have left gaps in the current knowledge about the physical causes of ultrasonic wavefront distortion caused by the chest wall.

Recent work on the simulation of ultrasonic pulse propagation¹⁰⁻¹² has provided insight about the wavefront distortion caused by the human abdominal wall. Although these studies have provided specific information about the relationships between soft tissue morphology and ultrasonic wavefront distortion, the work is not fully applicable to distortion caused by the human chest wall. The morphology of chest wall soft tissue is different from that of the abdominal wall in ways that can affect ultrasonic wavefront distortion.⁸ Furthermore, imaging through the chest wall is complicated by ribs that limit the usable acoustic window size and cause scattering and reflection.

The study reported here applies quantitative simulation methods, similar to those presented in Refs. 10 and 12, to anatomically detailed chest wall models that include the ribs. Accurate depiction of rib-ultrasound interactions requires not only representation of the strong reflections associated with sound speed and density contrast between ribs and soft tissue (already accurately modeled by the finite difference method of Ref. 10), but also modeling of the strong losses associated with propagation through bone and cartilage. For this reason, the finite-difference method described in Ref. 10 has been extended to include tissue-dependent absorption. Quantitative descriptions of the distortion caused by soft tissues are obtained by statistical analysis of simulated distortion. Visualizations of wavefronts propagating through maps of chest cross sections provide evidence about physical relationships between wavefront distortion and the morphology of ribs and soft tissue structures in the chest wall. Further insight about wavefront distortion mechanisms is provided by a comparison of distortion results for incident pulses of different center frequencies.

I. THEORY

Ultrasonic pulse propagation through the human chest wall is modeled here using the equations of motion for a fluid of variable sound speed, density, and absorption. The tissue is assumed motionless except for small acoustic perturbations. Absorption is included using an adaptation of the Maxwell solid model,¹³ in which all absorption effects are represented by a single relaxation time. This assumption results in frequency-independent absorption characteristics. Equivalent treatments of tissue-dependent absorption have been employed by a number of previous models for ultrasonic propagation in biological tissues.¹⁴⁻¹⁶ For such a fluid, the linearized equations of mass conservation, momentum conservation, and state can be combined to obtain the first-order, two-dimensional, coupled propagation equations,

$$\frac{\partial p(x,y,t)}{\partial t} + \rho(x,y) c(x,y)^2 \nabla \cdot \mathbf{v}(x,y,t) = -\alpha(x,y) p(x,y,t), \quad (1)$$

$$\rho(x,y) \frac{\partial \mathbf{v}(x,y,t)}{\partial t} + \nabla p(x,y,t) = 0. \quad (2)$$

Here, $p(x,y,t)$ is the acoustic perturbation in fluid pressure, $\mathbf{v}(x,y,t)$ is the vector acoustic particle velocity, $\rho(x,y)$ is the ambient density, $c(x,y)$ is the ambient sound speed, and $\alpha(x,y)$ is an absorption coefficient that is equivalent to the inverse of a spatially-dependent relaxation time $\tau(x,y)$.

The absorption coefficient α , defined as a real quantity, is related to the energy lost per unit length as follows. The propagation equations (1) and (2) lead, for plane-wave propagation of the form $p = e^{i(kx - \omega t)}$, to the dispersion relation

$$k = \frac{\omega}{c} \sqrt{1 + \frac{i\alpha}{\omega}}, \quad (3)$$

where k is the complex wavenumber, ω is the (real) radial frequency $2\pi f$, and c is the (real) sound speed. The imaginary part of the wavenumber k is the absorption in nepers per unit length. Thus, the absorption parameter α can be obtained by a numerical solution of the equation

$$\text{Im}[k] = \frac{\text{loss (dB/length)}}{20 \log_{10}(e)} = \text{Im}\left[\frac{\omega}{c} \sqrt{1 + \frac{i\alpha}{\omega}}\right]. \quad (4)$$

Solution of Eq. (4) results in wavenumbers having a real part that differs from ω/c . Since this discrepancy is less than 1% over the range of tissue properties employed in the present study, use of absorption coefficients computed from Eq. (4) does not significantly affect propagation characteristics except by adding the specified absorption.

Equations (1) and (2) were solved numerically using the finite-difference time-domain (FDTD) method described in Refs. 10 and 17. This method is a two-step MacCormack predictor-corrector algorithm that is fourth-order accurate in space and second-order accurate in time. The computations employed a spatial step size of 15 points per wavelength at the pulse center frequency of 2.3 MHz. Time step sizes were computed using a Courant-Friedrichs-Lewy number of 0.25. Further details on this class of finite difference algorithms can be found in Refs. 18-20.

The initial condition was chosen to model the experimental configuration in Ref. 8, in which a spatially broad, nearly planar wavefront was emitted from a wideband, pulsed, unfocused source far from the tissue layer. The initial wavefront was represented in the present simulation as a plane wave pulse propagating in the +y direction:

$$p(x,y,0) = -\sin[k_0(y-y_0)] e^{-(y-y_0)^2/(2\sigma^2)},$$

$$u(x,y,0) = 0,$$

and

$$v(x,y,0) = \frac{p(x,y,0)}{\rho c}, \quad (5)$$

where the wavenumber k_0 is equal to $2\pi f_0/c$ for a center frequency of f_0 , σ is the Gaussian parameter of the pulse temporal envelope, and u and v are the x and y components of the vector acoustic particle velocity \mathbf{v} . The spatial Gaussian parameter σ was chosen to simulate the bandwidth of the pulse used in the experiments, as discussed below in the Method section.

The computational configuration is analogous to that described in Ref. 10. The domain of computation is two-dimensional, with the y direction taken to be parallel to the direction of propagation and the x direction parallel to the initial wavefront. As in Ref. 10, periodic boundary conditions were applied on the domain edges that were parallel to the direction of propagation, while radiation boundary conditions were applied on the edges perpendicular to the direction of propagation.

II. METHOD

This study employed six chest wall specimens obtained during the autopsies of four different donors between 79 and 85 years of age at death. One specimen (4L) was from a white female, while the others were from white males. After the specimens were obtained, they were stored unfixed at -20°C and thawed when needed for study. Wavefront distortion measurements were made on these and other specimens as part of a study described in Ref. 8. In those measurements, 2.3 MHz ultrasonic pulses generated by a 0.5-in. piston transducer propagated through individual chest wall specimens immersed in a 37°C water bath and the transmitted pulses were measured by a 96-element broadband cardiac array scanned to synthesize a two-dimensional aperture. Statistics describing wavefront distortion, including arrival time fluctuations, energy level fluctuations, and wave shape distortion, were computed for the measured pulses.

For the present study, six of the previously measured specimens were cut into ~ 7 -mm thick cross sections using the technique described in Ref. 10. The slices were then fixed and stained with a modified Gomori's trichrome stain according to the procedure detailed in Ref. 21, so that tissue types could be distinguished. This stain colored muscle tissue red and connective tissue blue while leaving the fat its natural color. Calcified tissue, including bone and cartilage in the current specimens, was not differentially stained by this technique, but the natural contrast between bone, cartilage, and marrow was sufficient to allow tissue mapping. Full-color 300 d.p.i. images of the cross sections were created by placing each stained tissue cross section directly onto the surface of a flatbed digital scanner. Image editing packages (Adobe Photoshop, Version 3.0, and the Gnu Image Manipulation Program, Version 1.0) were used to manually segment the cross sectional images, i.e., to map the images into regions that corresponded to one of six media. The media were water (representing water external to specimens or blood inside blood vessels), fat (including subcutaneous fat, fat interlaced within muscle layers, and marrow), muscle, connective tissue (including skin, septa, and fasciae), cartilage, and bone (including cortical bone and trabeculae within cancellous bone).

The nomenclature employed here for the cross sections corresponds to that of Ref. 8 for the whole specimens from which the cross sections were taken; each cross section is identified by a donor number together with "L" or "R" to indicate whether the corresponding specimen was taken from the left or right side of the breastplate. Additional numbers were used in Ref. 8 to indicate the intercostal space used in each measurement; here, lower-case letters are used to indicate independent acoustic paths. Wavefront distortion measurement results from four of the specimens employed here (4L, 5L, 7L, and 7R) were reported in Ref. 8. Distortion statistics for specimens 8L and 8R were not presented in Ref. 8 because of limited acoustic windows. No new measurements were made for the present study; statistics describing measured distortion are taken directly from Ref. 8.

The six segmented tissue maps are shown in Fig. 1. All of the cross sections contain a layer of septated subcutaneous fat below the skin. Most of the cross sections also include a layer composed primarily of the major pectoral muscles and their connective fasciae above the ribs. Between the ribs are regions of muscle (internal intercostal and external intercostal groups) interlaced with fat. In some cases, additional thin layers of fat between muscle layers are apparent. Cross sections 4L and 7R are cut along the intercostal spaces parallel to the ribs, so that in each a wide cross section of soft tissue appears. Cross sections 5L, 7L, and 8L are cut perpendicular to the ribs, so that each contains soft-tissue acoustic paths with width equal to the width of the corresponding intercostal spaces. Cross section 8R is cut perpendicular to the sternum at a location of large curvature in the ribs, so that the ribs are diagonally sectioned. Several blood vessels appear in cross sections 4L, 7L, 7R, and 8R; the largest of these is the internal mammary artery.

The basic structure of the cross sections is consistent with standard descriptions of chest wall anatomy.^{22,23} Ribs appear in each cross section; each rib is composed of a "costal cartilage" near the sternum (shown in most of the cross sections considered here) attached to a "true rib" (composed primarily of cancellous bone) at the edge farther from the sternum. In the cross sections considered here, the costal cartilages are primarily composed of calcified cartilage, surrounded by a thin layer of cortical bone (solid, dense bone with microscopic porous structure), which in turn is surrounded by the periosteum, a thin membrane of connective tissue. Cross sections 7L and 7R also appear to contain a small amount of cortical bone in the central portion of the ribs. This phenomenon may be associated with advanced calcification known to occur in aging humans.²⁴ Cancellous bone, composed of thin trabeculae that form macroscopic cells filled with marrow, is seen in all the ribs of cross section 5L, which was taken at a distance farther from the sternum so that the true ribs, rather than the costal cartilages, were included in this cross section. Some cancellous bone is also apparent within portions of the ribs of cross sections 4L and 8R. In each case, the cancellous bone is surrounded by a thin layer of cortical bone and by the periosteum. A portion of the sternum, composed of cancellous bone surrounded by cortical bone, is visible at the left side of cross section 4L.

The density and sound speed grids needed for the finite-

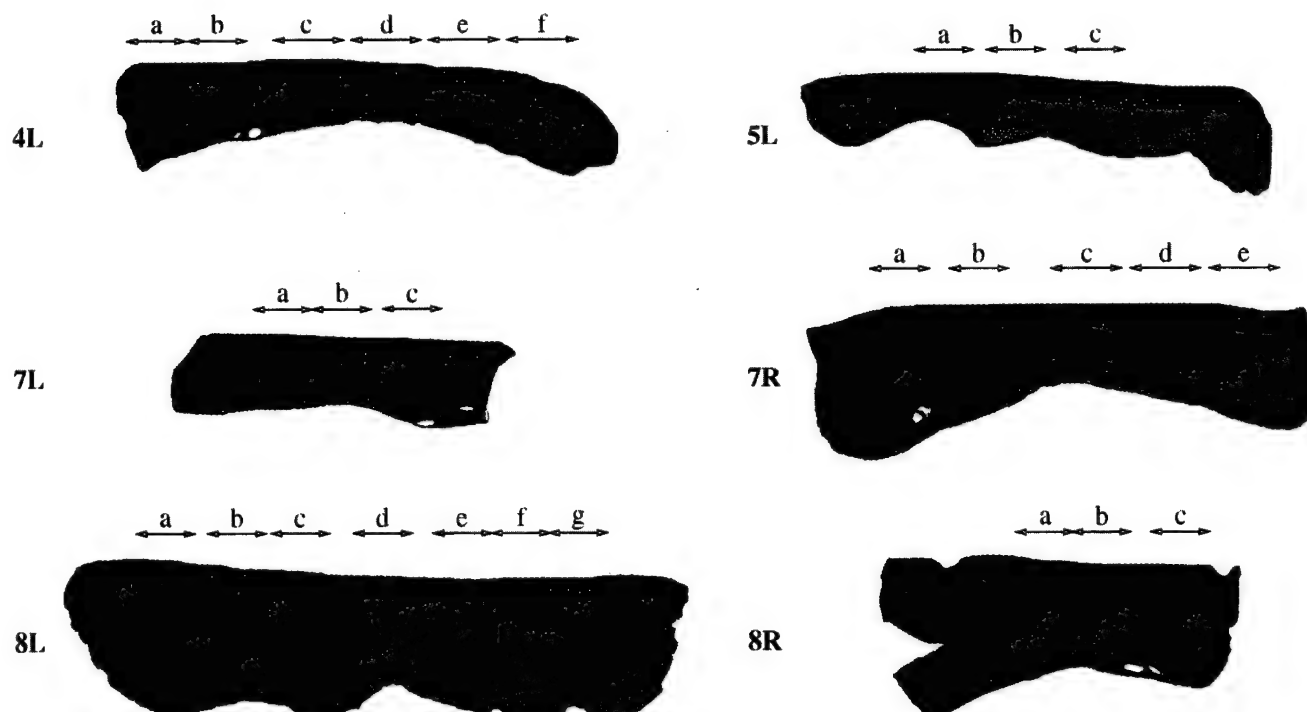


FIG. 1. Chest tissue maps used in simulations. In each map, blue denotes skin and connective tissue, cyan denotes fat, purple denotes muscle, orange denotes bone, and green denotes cartilage. Blood vessels appear as small water-filled (white) regions. Simulated apertures are indicated using lower-case letters for each cross section; the letters correspond to the acoustic path labels used throughout, while the length of the arrow beneath each letter corresponds to the extent of the simulated aperture. Smaller arrows indicate 55-element (11.60-mm) apertures while large arrows indicate 68-element (14.28-mm) apertures.

difference computation were created by mapping regions of the segmented tissue images to reference density and sound speed values for the five tissue types and water. The water sound speed and density employed are those of pure water at body temperature (37.0 °C).^{25,26} Sound speeds for muscle and fat were obtained by averaging values for human tissues given in Refs. 27 and 28. A representative sound speed for connective tissue was determined using an empirical formula relating collagen content to ultrasonic sound speed²⁹ together with a measured value for the collagen content of human skin.³⁰ The sound speed employed for bone was obtained from an average of values reported in Ref. 31 for longitudinal-wave propagation in human cortical bone. The sound speed used here for cartilage is that given in Ref. 32 as quoted in Ref. 27. Density values for soft tissues were determined from Ref. 33 by averaging values reported for adipose tissue, skeletal muscle, and skin, respectively. Density values employed for bone and cartilage are average values from Ref. 31.

Absorption values were determined from attenuation measurements summarized in Ref. 27 for human fat at 37 °C, human bicep muscle at 37 °C, human skin at 40 °C, human and bovine cartilage at 23 °C, and human skull (temperature not reported). Attenuation values reported at other ultrasonic frequencies were interpolated (or, for the skull data, extrapolated) to obtain values for 2.3 MHz (corresponding to the pulse center frequency employed here and in Ref. 8) assuming a linear dependence of attenuation on frequency. This assumed linear dependence is a simplifying approximation; tissue measurements show that attenuation varies approximately as $\alpha \propto f^\beta$, where β is typically between 0.9 and 1.5

for various human soft tissues.³⁴ The absorption for water was estimated by extrapolating frequency- and temperature-dependent absorption values summarized in Ref. 35 to 2.3 MHz and 37.0 °C. The values of tissue parameters employed in the present study are given in Table I.

The finite-difference program was employed to compute propagation of a plane wave pulse through each scanned cross section from the skin to the peritoneal membrane, mimicking the propagation path employed in the distortion measurements of Ref. 8. The spatial step size of the finite-difference grid was chosen to be 0.0442 mm, or 1/15 wavelength in water at the center frequency of 2.3 MHz. The temporal step size was chosen to be 0.00725 μ s, for an optimal Courant–Friedrichs–Lewy number $c\Delta t/\Delta x$ of 0.25.²⁰ The Gaussian parameter σ of the source pulse was chosen to be 0.4766 mm in accordance with the experimentally measured pulse bandwidth (for pulses transmitted through a water path) of 1.2 MHz. A visual comparison confirmed that the

TABLE I. Assumed physical properties for each tissue type employed in the simulations.

Tissue type	Sound speed (mm/ μ s)	Density (g/cc)	Absorption (dB/mm)
Water	1.524	0.993	0.0007
Fat	1.478	0.950	0.12
Muscle	1.547	1.050	0.21
Connective	1.613	1.120	0.37
Cartilage	1.665	1.098	0.97
Bone	3.540	1.990	4.37

simulated pulse closely matched the measured pulses in shape and length.

Each simulation was performed on a workstation with 128 MB of random-access memory. Finite-difference grids on the order of 1500×1000 points were employed. At each time step, the wave field was updated on a grid subset chosen to include the entire support of the acoustic wave but to exclude quiescent regions. The entire pressure field was saved as a raster image at intervals of $0.725 \mu\text{s}$ for later visualization. The computation time for each simulation was on the order of five hours.³⁶

Signals were recorded for $8.62 \mu\text{s}$ at a sampling frequency of 138 MHz by simulated apertures with dimensions close to those in the experimental study of Ref. 8. Positions of all simulated apertures employed are sketched in Fig. 1. The simulation of receiving elements was performed by integrating the locally-computed pressure over the element pitch of 0.21 mm. For cross sections cut parallel to the ribs, the simulated apertures contained 68 elements for an aperture width of 14.28 mm. For cross sections cut perpendicular to the ribs, 55 simulated elements were used to form 11.55 mm apertures. Element directivity effects were implicitly incorporated by the integration of acoustic fields over the width of each element; the resulting directivity functions correspond to those for an idealized line element of width 0.21 mm.

A one-dimensional version of the reference waveform method^{10,37} was used to calculate the arrival time of the pulse at each receiving position in the simulation data. In this method, the relative arrival time of each received waveform is computed by cross-correlation with a reference waveform. The arrival time fluctuations across the receiving aperture are then calculated by subtracting a linear fit from these calculated arrival times, and the root-mean-square value of these fluctuations is computed. Energy level fluctuations in the data were calculated by summing the squared amplitudes of each waveform over a $2.4\text{-}\mu\text{s}$ window that isolated the main pulse, converting to decibel units, and subtracting the best linear fit from the resulting values. As for polynomial fits previously employed in wavefront distortion measurements,⁸ the purpose of the linear fit removal in each case was to compensate for gross changes in tissue thickness across the array. Variations in pulse shape across the aperture were evaluated using the waveform similarity factor;³⁷ this quantity, which can be considered a generalized cross-correlation coefficient, has a maximum of unity when all received waveforms are identically shaped.

To test the frequency dependence of chest wall wavefront distortion, propagation through eight portions of specimens, each containing only soft tissue, was also computed for wavefronts having center frequencies of 1.6 and 3.0 MHz. In each case, the initial wavefront was chosen to have the same temporal envelope as above. The absorption coefficient at these frequencies for each tissue type was extrapolated from the value employed at 2.3 MHz using the assumption that absorption depended linearly on the center frequency. The spatial and temporal sampling rates were also varied in inverse proportion to the pulse center frequency. All runs were otherwise identical in configuration and processing to those described above.

TABLE II. Statistics of simulated wavefront distortion caused by thirteen soft tissue paths within chest wall cross sections. The "Path" column shows the cross section label and aperture letter for each path; these labels correspond to those shown in Fig. 1. The statistics shown include the average specimen thickness for the tissue path considered, rms values and correlation lengths (CL) of the arrival time fluctuations (ATF) and the energy level fluctuations (ELF), the waveform similarity factor (WSF), and the total attenuation.

Path	Thickness (mm)	ATF		ELF		WSF	Attenuation (dB)
		rms (ns)	CL (mm)	rms (dB)	CL (mm)		
4L-c	15.4	32.0	0.60	1.98	1.68	0.981	5.62
4L-d	12.7	10.0	2.58	0.46	1.23	0.999	4.08
4L-e	16.0	10.0	1.37	1.61	1.74	0.998	5.26
4L-f	17.0	17.3	2.48	0.92	1.61	0.999	5.33
5L-a	11.0	11.6	0.95	1.51	1.13	0.991	4.29
5L-c	15.0	14.8	1.03	1.15	1.19	0.996	5.01
7L-a	16.2	16.8	2.64	0.95	1.29	0.999	5.46
7L-b	14.9	22.5	2.66	1.19	1.61	0.998	4.91
7R-c	17.7	17.4	1.77	2.52	2.07	0.997	5.83
7R-d	21.0	8.3	1.10	0.85	1.79	0.999	7.07
7R-e	24.7	13.7	1.37	1.06	1.62	0.997	8.69
8R-a	23.8	26.6	1.78	2.58	1.40	0.992	7.76
8R-b	22.2	29.9	1.44	1.95	1.11	0.989	6.09
Mean	17.5	17.8	1.67	1.44	1.50	0.995	5.80
St. Dev.	4.2	7.8	0.71	0.66	0.30	0.005	1.33

III. RESULTS

Simulated wavefront distortion results for 13 soft tissue paths (i.e., paths in which wavefront distortion was not significantly influenced by the ribs) are shown in Table II. These results indicate that soft tissue paths cause a wide range of wavefront distortion effects depending on the specific morphology of each path. For instance, path 7R-c causes arrival time and energy level fluctuations that are more than twice the magnitude of those caused by the adjacent path 7R-d. This difference is thought to arise from morphological features, including muscle tissue with interlaced fat and a large amount of connective tissue, of the tissue within path 7R-c. Also notable is that the specimen thickness does not closely correspond to variations in distortion. The largest rms arrival time fluctuation and lowest waveform similarity factor, for example, are caused by path 4L-c, which has an average thickness less than the mean for all the tissue paths.

Wavefront distortion statistics for the 13 soft tissue paths are graphically summarized in Fig. 2 together with corresponding statistics for all of the soft tissue measurements reported in Ref. 8. This comparison indicates that wavefront distortion caused by soft tissues in the chest wall simulations is comparable to measured distortion. Arrival time fluctuations and energy level fluctuations for simulated distortion are slightly less than measured values, but mean values of both fluctuations for the simulations fall well within one standard deviation of the corresponding mean fluctuation for the measurements. The waveform similarity factor, however, is substantially higher for simulations than measurements, indicating that simulated waveforms were distorted considerably less than measured waveforms. Correlation lengths for the simulated distortions are somewhat less

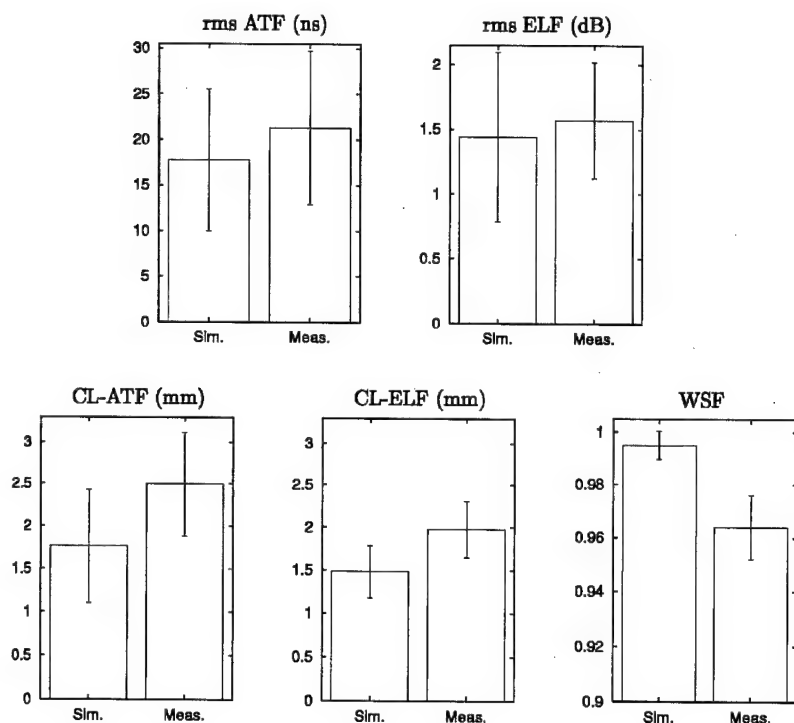


FIG. 2. Summary of distortion statistics for soft tissue paths. The bar chart shows mean values of the rms arrival time fluctuations (ATF), rms energy level fluctuations (ELF), correlation lengths (CL) of these fluctuations, and waveform similarity factors (WSF) for the simulations performed in the present paper and the experiments reported in Ref. 8. Error bars indicate a range of plus or minus one standard deviation from the mean.

than measured values. However, consistent with measurements, the mean correlation length of the simulated arrival time fluctuations is greater than that for the simulated energy level fluctuations.

As in Ref. 8, rib structures were found to cause much more distortion than soft tissue alone. The varied nature of distortion caused by rib effects is illustrated in Fig. 3, which shows three representative sets of measured signals for specimen 8L. These measurements were made during the study reported in Ref. 8. The first panel shows 96 adjacent measured signals, along the array direction (approximately parallel to the ribs) for propagation through a tissue path within an intercostal space. The signals are not severely distorted; secondary arrivals are discernible, but are of lower amplitude than the main arrival. The second panel shows 96 measured signals for an elevation over a rib. Here, all signals are severely distorted. Multiple arrivals, as well as high-amplitude spatially-random fluctuations, are seen. The third panel shows 50 measured signals along the elevation direction (perpendicular to the ribs), centered over the soft tissue between the ribs. Here, the main wavefront is curved rather than straight, an additional arrival behind the main wavefront is seen, and portions of the signals from over the ribs (at both edges of the panel) are advanced relative to the signals from the central soft tissue region.

The present simulations allow more detailed qualitative and quantitative investigation of rib effects than were possible from the previous measurements. Propagation through two rib-influenced paths is illustrated in Figs. 4 and 5, in which computed ultrasonic pulses are superimposed on portions of the tissue maps from Fig. 1. (Similar visualizations of propagation through soft human body wall tissue were shown in Ref. 10.)

Figure 4 shows propagation through a thin rib, composed chiefly of cancellous bone, in cross section 5L (corresponding approximately to path 5L-b). A strong reflection

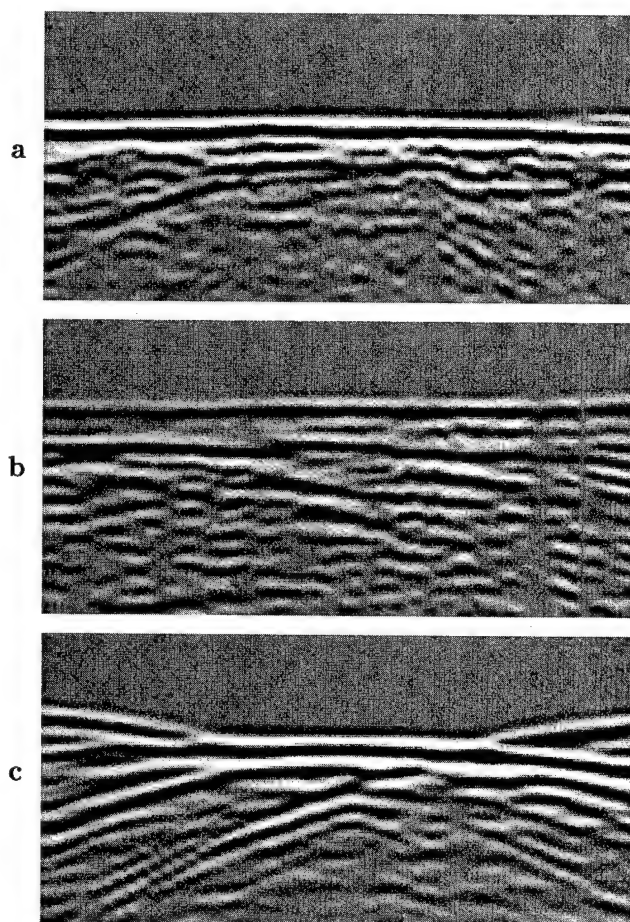


FIG. 3. Measured waveforms for three propagation paths in specimen 8L. Each panel shows received waveforms on a bipolar logarithmic gray scale with a dynamic range of 40 dB. The horizontal range shown in each panel is 20 mm and the vertical range shown is $6.4 \mu\text{s}$. (a) Tissue path between two ribs, in azimuth direction (parallel to ribs). (b) Path including a rib, azimuth direction. (c) Tissue path including intercostal space between two ribs, elevation direction (perpendicular to ribs).

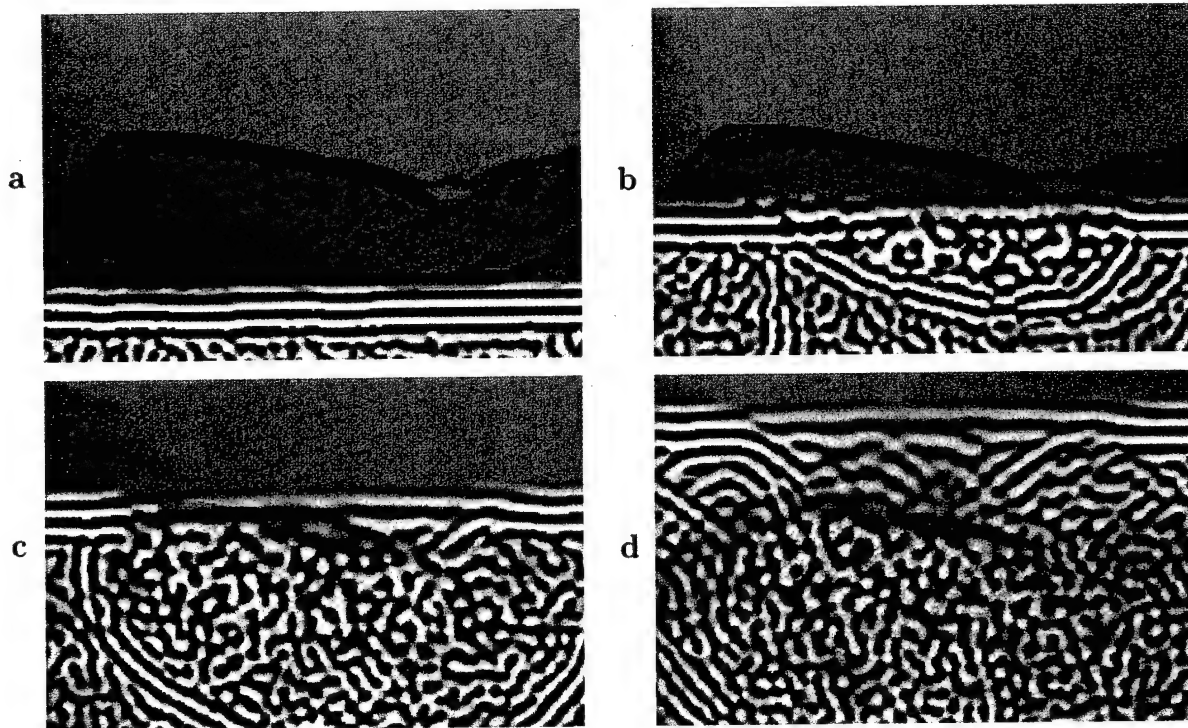


FIG. 4. Simulated propagation through the central rib in cross section 5L (path 5L-b). Panels (a)–(d) show instantaneous acoustic pressure fields at successive intervals of $2.17 \mu\text{s}$. Each panel shows an area that spans 20.32 mm horizontally and 14.58 mm vertically. Logarithmically compressed wavefronts are shown on a bipolar scale with black representing minimum pressure, white representing maximum pressure, and a dynamic range of 57 dB.

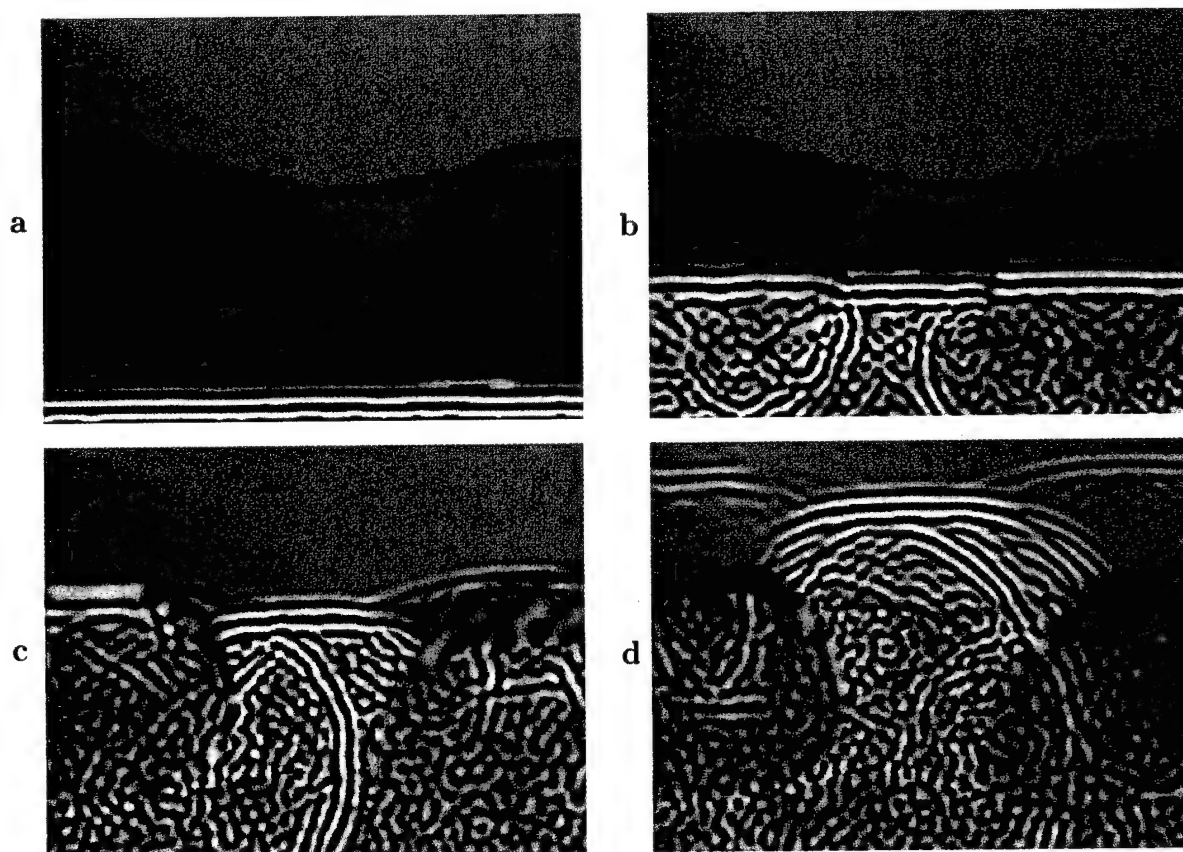


FIG. 5. Simulated propagation through an intercostal space in cross section 8L (path 8L-b). Panels (a)–(d) show instantaneous wavefields at successive intervals of $3.62 \mu\text{s}$. Each panel shows an area that spans 28.27 mm horizontally and 21.20 mm vertically. Wavefronts are shown using the same format as in Fig. 4.

occurs at the first interface between bone and soft tissue, removing a substantial amount of energy from the main wavefront. The small, high-contrast trabeculae within the rib cause considerable scattering, as can be observed in panel (b) of Fig. 4. The scattering causes random fluctuations behind the main wavefront; these fluctuations somewhat resemble those seen in the measured data of Fig. 3(b). After passing through the rib, as seen in panels (c) and (d) of Fig. 4, the central portion of the wavefront shows substantial attenuation and distortion. However, the average arrival time of the wavefront is not greatly changed by propagation through the rib, but is advanced by only about one-half period. This phenomenon apparently occurs because the influence of the "slow" marrow (modeled here as fat) counteracts the influence of the "fast" trabeculae. Noteworthy is that the predominant ultrasonic wavelength has increased after propagation through the rib, so that the effective center frequency of the wavefront has been lowered. Since the absorption model used in the present study includes only frequency-independent absorption, the loss of short-wavelength components in this simulation results only from frequency-dependent scattering caused by the trabeculae.

Propagation within path 8L-b, which includes two larger ribs and the corresponding intercostal space, is illustrated in Fig. 5. At the position of the cross section, these ribs are composed primarily of cartilage and surrounded by a thin layer of cortical bone. Since the cartilage and bone of these ribs are modeled as homogeneous structures, small-scale scattering within these tissues did not occur in this simulation. Instead, the wavefront is reflected from interfaces between cartilage, bone, and soft tissue.

The visualization shown in Fig. 5 provides physical reasons for all the rib-related distortion phenomena seen in the measured data of Fig. 3(c). The wavefronts propagating through the ribs show greater attenuation than that in Fig. 4, both because of the high absorption of the ribs and because of the reflections noted above. These wavefronts are also advanced relative to the wavefront propagating through the intercostal space, because of the higher sound speed of both bone and cartilage. The wavefront propagating through the intercostal space is distorted somewhat by the inhomogeneous soft tissue path, as can be observed in panels (b) and (c). However, much greater distortion results from interaction between the wavefront and the ribs. A rightward-propagating reflection, seen in panels (b) and (c), combines with the main wavefront in panel (d) to result in severe distortion at the right side of the central wavefront. A leftward-propagating reflection from the other rib is also apparent. Furthermore, diffraction from the edges of the ribs results in large curvature of the soft tissue wavefront.

Distortion and attenuation statistics for a variety of simulations employing rib-influenced paths are shown in Table III. Footnotes in Table III indicate physical causes of distortion present within each path. A variety of distortion and attenuation mechanisms are illustrated. Propagation through small intercostal spaces (paths 4L-a, 8L-b, 8L-f, and 7R-a) causes diffraction effects that introduce substantial curvature into the wavefront, as seen in Fig. 5. This large-scale wavefront curvature is associated with large arrival

TABLE III. Statistics of simulated wavefront distortion caused by fourteen tissue paths including rib structures. The footnotes associated with the label for each path indicate morphological features and physical phenomena that affected the wavefront distortion computed for that path. The format is analogous to that in Table II.

Path	Thickness (mm)	ATF		ELF		WSF	Attenuation (dB)
		rms (ns)	CL (mm)	rms (dB)	CL (mm)		
4L-a ^{a,b,c,d}	21.0	260.3	3.00	2.58	2.72	0.968	15.33
4L-b ^{b,c}	17.6	161.9	1.90	4.16	1.49	0.641	43.35
5L-b ^b	14.2	92.5	0.69	3.06	1.92	0.775	26.87
7L-c ^{c,e}	17.8	47.2	1.58	5.33	2.04	0.958	19.66
7R-a ^{a,c,d}	30.4	123.1	2.12	3.80	1.78	0.960	16.57
7R-b ^{c,e}	24.3	165.6	2.71	6.88	2.07	0.274	43.06
8L-a ^c	25.3	113.9	1.18	7.75	2.29	0.907	32.44
8L-b ^{a,d}	22.8	109.7	2.05	3.43	1.22	0.974	10.28
8L-c ^c	28.8	134.0	2.75	3.04	1.57	0.944	40.47
8L-d ^d	23.6	78.9	0.64	3.06	1.55	0.950	6.78
8L-e ^c	26.4	208.8	1.91	3.62	1.50	0.810	44.27
8L-f ^{a,d}	28.5	169.9	1.79	5.02	1.95	0.916	10.70
8L-g ^c	27.6	210.8	1.40	3.36	1.35	0.892	44.22
8R-c ^{b,c}	24.9	81.4	2.08	2.76	1.25	0.962	44.32

^aSmall intercostal spaces.

^bCancellous bone.

^cCortical bone and cartilage.

^dStrong rib reflections.

^eCortical bone within cartilage.

time fluctuation values although the wavefronts generally appear to be locally smooth. Interference between directly-transmitted and rib-reflected wavefronts (paths 4L-a, 8L-b, 8L-d, 8L-f, and 7R-a) introduces arrival time, energy level, and waveform distortion substantially greater than that for soft tissue paths without ribs. Propagation through cancellous bone (paths 4L-a, 4L-b, 5L-b, and 8R-c) results in considerable attenuation and large waveform distortion, while propagation through cortical bone and cartilage (paths 4L-a, 4L-b, 8L-a, 8L-c, 8L-e, 8L-g, 7L-c, 7R-a, 7R-b, and 8R-c) results in even larger attenuation but smaller distortion. Where bone is embedded within cartilage (paths 7L-c and 7R-b), additional scattering also occurs. For the path including a large bone inclusion (path 7R-b), this scattering results in an extremely high energy level and waveform distortion.

Computed frequency-dependent wavefront distortion statistics are summarized in Fig. 6. Tissue paths used for these computations, none of which include rib structures, are those labeled 4L-d, 4L-f, 5L-a, 5L-c, 8R-a, 8R-b, 7L-a, and 7L-b in Fig. 1. The results shown in Fig. 6 indicate that arrival time fluctuations, energy level fluctuations, and waveform distortion all become more severe with increasing pulse frequency. The most dramatic change is in the energy level distortion; on average, the rms energy level fluctuations for the 3.0-MHz signals are 2.3 times those for the 1.6-MHz signals. Correlation lengths of both arrival time and energy level fluctuations decrease with frequency, so that the predominant length scales of ultrasonic wavefront distortion are seen to decrease with the ultrasonic wavelength. As with the rms distortion statistics, the most dramatic frequency-dependent change is in the energy level fluctuations. Still, even the high-frequency pulses here show substantially

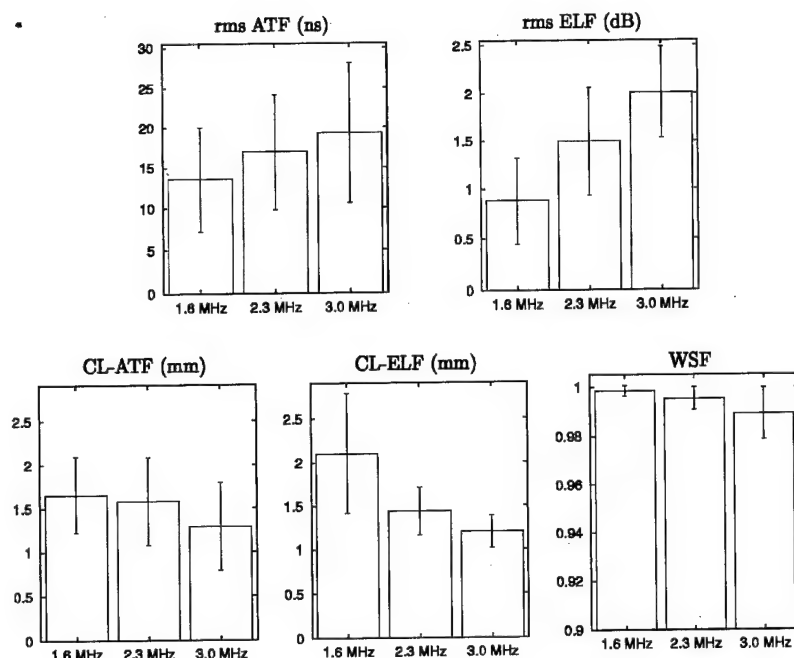


FIG. 6. Summary of simulated frequency-dependent distortion results. Mean rms arrival time fluctuations (ATF), energy level fluctuations (ELF), correlation lengths (CL) of these fluctuations, and waveform similarity factors (WSF) are shown for each of the three pulse frequencies investigated. Error bars indicate a range of plus or minus one standard deviation from the mean.

smaller distortion than that previously observed in experiments and simulations for the human abdominal wall.^{10-12,38}

IV. DISCUSSION

As with earlier simulations of propagation through tissue,^{10,12} the current study shows qualitative agreement with measured wavefront distortion results for similar specimens.⁸ However, the accuracy of the present model is limited by simplifications of true tissue structure. In particular, the computational model here does not account for property variations within tissue types, tissue microstructure, or three-dimensional tissue structure. Each of these simplifications limits the ability of the present model to precisely mimic experimentally measured ultrasonic wavefront distortion. These limitations are discussed, with respect to soft tissues, in Ref. 10.

The modeling of ribs adds additional complication. In the current study, individual trabeculae were assumed to be composed of tissue having properties identical to cortical bone, an assumption known as Wolff's hypothesis.³⁹ The validity of this hypothesis has been questioned;^{40,41} however, measured elastic properties of individual trabeculae vary widely^{40,41} and recent work⁴² has provided support for Wolff's hypothesis. Thus, the properties employed here for trabecular bone can be regarded as reasonable order-of-magnitude estimates. Likewise, the modeling of marrow as fat tissue is a simplifying assumption that may have limited validity, although available data suggest that the density and sound speed of marrow are close to those for other adipose tissues.³¹ In addition, the present model for cartilage is based on measurements of normal cartilage, while the cartilage present in the specimens employed here was calcified due to the age of the donors. However, density measurements made on eight representative samples of calcified cartilage (two from specimen 7R, four from specimen 1R,⁸ and two from an unused specimen) resulted in an average density of 0.00111 kg/m^3 , which is different by only 1% from the den-

sity assumed here. Since sound speed in calcified tissue has been empirically shown to be directly related to density,^{43,44} this small change in density suggests that the acoustic properties of the calcified cartilage in our specimens is close to that for normal cartilage.

The computations reported here model the chest wall as a fluid of variable sound speed, density, and compressibility. This model implicitly neglects shear wave propagation. The neglect of shear waves in soft tissues is believed to be justified because the absorption of shear waves in soft tissues is much greater than absorption of longitudinal waves.^{45,46} In calcified tissues, however, significant shear waves are known to be generated.^{47,48} In the current scattering configuration, some shear waves are likely generated wherever the rib surface is far from parallel to the wavefront. However, since shear wave absorption has been found to be somewhat larger than longitudinal wave absorption for ultrasonic propagation in bone,⁴⁷ the significance of shear-wave propagation within bone on transmitted ultrasonic wavefronts is questionable. For this reason, omission of nonlongitudinal waves in the present study, as in another computational study of ultrasonic scattering from bone,⁴⁹ is believed to be justified; however, further study would be required to confirm this assumption.

The absence of frequency-dependent absorption is a possible source of error in the present estimates of total tissue attenuation, energy level fluctuations, and waveform distortion. However, since absorption in tissue increases approximately linearly with frequency, lower absorption for frequency components below the pulse center frequency would nearly cancel higher absorption for frequency components above the center frequency, so that the average absorption incurred by a wideband pulse should still be computed with fair accuracy. For this reason, the absence of frequency-dependent absorption in the calculations reported here is not considered to be a significant source of error in the computed attenuation or energy level fluctuation curves. Still, the inclusion of frequency-dependent absorption would result in

additional waveform distortion effects. The lack of this effect is a likely reason for the lower waveform distortion (higher waveform similarity factors) obtained from simulations as compared to measurements. However, the absence of frequency-dependent absorption effects allowed frequency-dependent scattering effects to be clearly quantified separately from absorption effects.

Although the simulations were planned to match the measurements of Ref. 8 closely, a number of differences remain. The most important of these, as discussed in Ref. 10, is that the simulations were performed using a two-dimensional tissue model while the measurements were inherently three-dimensional. Other differences include details of the source waveform and wavefront shape, variations in the specimen orientations and the regions interrogated, and variations in the distance between the specimen and the real or simulated receiving aperture. All of these differences could contribute to discrepancies between measurements and simulations.

In general, most of the simplifying assumptions in the present tissue model are likely to result in underestimation of wavefront distortion produced by the human chest wall. The incorporation of tissue microstructure, spatially-dependent acoustic properties for each tissue type, shear wave propagation in bone and cartilage, three-dimensional propagation, and frequency-dependent absorption could all result in greater spatial and temporal variations in the propagating acoustic fields, so that these features could produce simulated distortion with characteristics closer to measurements. For this reason, distortion statistics computed using the present tissue model should be interpreted as lower limits for the statistics of distortion occurring in real chest wall tissue.

Additionally, some of the discrepancy between simulated and measured distortion may be explained by the non-uniform characteristics of the receiving transducer employed in the measurements.⁸ The water-path measurements reported in Ref. 8 show arrival time fluctuations (mean 2.21 ns) and energy level fluctuations (mean 0.36 dB); although small, these fluctuations are comparable to the difference between the average measured and simulated fluctuations. Thus, compensation for arrival time and energy level fluctuations due to transducer irregularities could reduce measured distortion to levels closer to the simulations. Also, the waveform similarity factor for water path measurements was 0.991,⁸ which indicates greater waveform distortion than the average value of 0.995 computed here for soft tissue paths. Thus, compensation of the measured data for transducer impulse-response variations could raise the measured waveform similarity factor to a value in closer agreement with simulations.

Previous experimental measurements of wavefront distortion caused by the human chest wall⁸ have suggested that distortion caused by chest wall soft tissues is less severe than that caused by the human abdominal wall.^{11,38} This difference has been observed to occur even though average specimen thicknesses were comparable in chest wall⁸ and abdominal wall^{11,38} measurements. The present results provide support for these results; arrival time and energy level distortion by the chest wall was found here to be smaller than that produced by the abdominal wall in previous simulation

studies.^{10,12} For the simulations, this difference may be partially explained by the fact that the chest wall specimens employed here are thinner on average (mean thickness 17.5 mm) than the abdominal wall cross sections employed in Refs. 10 and 12 (mean thickness 26.7 mm). Another possible partial explanation is that the pulse center frequency employed in abdominal wall measurements and simulations was 3.75 MHz, significantly higher than the center frequency of 2.3 MHz for the chest wall measurements and simulations. Differences in pulse frequency and specimen thickness may explain the discrepancy in energy level distortion between the abdominal wall and chest wall, but do not fully explain the discrepancy in arrival time distortion results. For instance, the mean arrival time and energy level fluctuations per unit length are 1.02 ns/mm and 0.083 dB/mm for the present study vs 1.96 ns/mm and 0.105 dB/mm for the abdominal wall cross sections of Ref. 10 and 12. Arrival time distortion was shown here to increase only subtly with increasing pulse frequency, so that this discrepancy in arrival time fluctuations is not fully explained by pulse frequency differences. However, energy level fluctuations increase markedly with frequency for chest wall tissue. Thus, for equal ultrasonic pulse frequencies, chest wall tissue should cause energy level distortion per unit length comparable to that caused by abdominal wall tissue.

It was suggested in Ref. 8 that chest wall morphology may differ from abdominal morphology in a manner that results in smaller ultrasonic wavefront distortion. The cross sections employed here can be compared with those employed in Refs. 10 and 12 to evaluate the importance of morphological differences between chest wall and abdominal wall tissue. One difference between the two groups of cross sections is the nature of the subcutaneous fat layers. The abdominal wall cross sections generally contain thicker fat layers, containing many more lobular structures than the chest wall cross sections. Since the high contrast between septa and fat causes substantial ultrasonic scattering,¹⁰⁻¹² this morphological difference is likely to result in lower overall energy level and waveform distortion for chest wall tissue (although, as discussed above, the energy level distortion per unit propagation length should be comparable). Also, the abdominal wall and chest wall cross sections have a markedly different structure within the muscle layers that occur below the subcutaneous fat. The abdominal wall cross sections have many large-scale features due to aponeuroses (interfaces between muscle groups, composed of connective tissue and fat) and large fatty regions. These large-scale features cause large wavefront fluctuations that are associated with large rms arrival time fluctuations.^{10,12} In contrast, muscle layers of the chest wall cross sections considered here contain primarily smaller-scale structures associated with small islands of interlaced fatty tissue. This morphological difference may result in lower large-scale arrival time fluctuations but significant energy level fluctuations associated with scattering, consistent with the differences between distortion caused by soft tissues in the abdominal wall and the chest wall.

The present results for the frequency dependence of distortion provide further insight into the importance of scatter-

ing effects relative to large-scale structure in wavefront distortion caused by soft tissues. If wavefront distortion in the chest wall were caused only by large-scale tissue structures, the distortion would be roughly independent of frequency, since propagation effects are independent of frequency in the geometric acoustics limit. However, distortion caused by scattering effects should increase with the pulse frequency for inhomogeneities of size comparable to the wavelength. Previous simulation and experimental studies¹⁰⁻¹² on distortion caused by the human abdominal wall have suggested that energy level fluctuations and waveform distortion are generally associated with scattering effects, while arrival time fluctuations are predominantly caused by large-scale path length differences. The present results, while consistent with those conclusions, indicate that scattering plays a role in all types of distortion considered here. Since energy level fluctuations and waveform similarity factors exhibit more dramatic increases in distortion with increasing pulse frequency, the present results suggest that scattering is of primary importance in causing energy level and waveform distortion and of secondary importance in causing arrival time distortion.

These results can be employed to evaluate the potential of various approaches to improve echocardiographic imaging. Available acoustic windows for transthoracic imaging are severely limited by the presence of the ribs, so that image quality cannot be significantly improved by an increase of aperture size. The present results also indicate that use of higher-frequency probes may provide less benefit than expected because of frequency-dependent scattering in the chest wall.

For these reasons, aberration correction methods are potentially important in transthoracic echocardiography, particularly for higher-frequency imaging. The frequency-dependent distortion results reported here suggest that distortion models employing single phase screens may be of some benefit for aberration correction in echocardiography through soft tissue paths. The relatively weak dependence of arrival time fluctuations on pulse frequency suggests that a large portion of arrival time variations are caused by tissue structures too large to cause significant frequency-dependent scattering effects. Similar conclusions regarding the importance of large-scale structures to arrival time fluctuations have also been drawn from results presented in Refs. 10 and 12.

Still, the present results, like those from earlier studies,¹⁰⁻¹² suggest that single phase screens will not provide complete correction for distortion caused by soft tissues. In particular, methods employing single phase screens will not completely remove distortion caused by scattering. The sharp increase of amplitude and waveform distortion with frequency, as well as the moderate increase of arrival time distortion with frequency, indicate that scattering effects become much more important to ultrasonic aberration as imaging frequencies increase. Furthermore, phase screen models do not inherently account for distortion caused by rib structures, shown here to produce diffraction, reflection, and scattering. Thus, any attempted correction using only phase

screen models is likely to provide little improvement in the presence of strong rib-induced effects.

Other correction models that incorporate rib structures may provide greater image improvements for the distortions most important to echocardiography. Processing wavefronts with techniques such as angular spectrum filtering can remove some spurious arrivals,⁵⁰ although such computations may be difficult to incorporate into a general correction algorithm. Other possible methods include those incorporating models of tissue structure. Models incorporating ray acoustics⁹ may provide improvement, but implicitly neglect diffraction and scattering effects, so that aberration correction would be incomplete, particularly for small intercostal spaces. A more complete aberration correction method could employ synthetic focusing using full-wave numerical computation of acoustic fields within sufficiently accurate models of tissue structure. This method has been implemented, within the context of a quantitative frequency-domain inverse scattering method, in Ref. 51. However, the results presented here indicate that distortion caused by soft tissue and rib structures varies widely based on morphological variations between (and within) individuals. Thus, for any general correction method employing models of tissue structure, separate models of tissue structure must be constructed for each region of interest.

V. CONCLUSIONS

A computational study of ultrasonic propagation through the chest wall, including tissue-dependent absorption as well as detailed anatomical cross sections, has been presented. For soft tissue paths, computational results for arrival time distortion, energy level distortion, and correlation lengths of these distortions are comparable to those reported in previous chest wall measurements. Both simulations and measurements indicate that arrival time distortion and energy level distortion caused by soft tissues in the human chest wall is smaller than that caused by the human abdominal wall. Differences in morphology between the abdominal wall and the chest wall provide a probable explanation for this difference.

Distortion caused by rib structures is much more severe than that caused by soft tissues. Reflections and diffraction from rib structures complicate wavefronts that travel through soft tissue paths adjacent to ribs and can cause arrival time and energy level fluctuations much greater than those induced by soft tissue structures. Wavefronts propagating directly through rib structures are attenuated by both internal absorption and reflection at interfaces between bone, cartilage, and soft tissue. Internal scattering within rib structures causes distortion phenomena that include severe waveform and energy level distortion, additional attenuation, and lowering of the effective frequency for the transmitted pulse. The strong dependence of distortion on the morphological details of rib structures presents a major challenge for aberration correction in echocardiography.

Simulation of propagation through soft tissue paths using three different pulse frequencies has indicated that the distortion types investigated here have different frequency dependence. Arrival time fluctuations increase subtly with frequency, while energy level and waveform distortion in-

crease greatly. Thus, a substantial portion of arrival time fluctuations produced by the chest wall may be explained by large-scale tissue variations, but some arrival time distortion and most energy level and waveform distortion apparently result from scattering. Thus, correction of wavefront distortion caused by soft tissues should become both more important and more challenging as pulse frequencies employed in imaging systems are increased.

ACKNOWLEDGMENTS

The authors thank Cari Kelly, Tara Jones, Tracy David, and Michael Pirri for assistance in creating accurate tissue maps of the chest wall cross sections. The original two-dimensional version of the distortion estimation software using the reference waveform method was developed by D.-L. Donald Liu. Funding for this investigation was provided by NIH grants No. DK 45533, No. HL 50855, and No. CA 74050, U.S. Army Grant No. DAMD17-98-1-8141, DARPA Grant N00014-96-0749, and the University of Rochester Diagnostic Ultrasound Research Laboratory Industrial Associates. Some computations were performed at the Cornell National Supercomputing Facility, which was supported in part by the National Science Foundation, New York State, and the IBM Corporation.

- ¹ H. Feigenbaum, *Echocardiography* (Lea and Febiger, Philadelphia, 1994).
- ² A. E. Weyman, *Principles and Practice of Echocardiography*, 5th ed. (Lea and Febiger, Philadelphia, 1994).
- ³ J. T. T. Chen, *Essentials of Cardiac Imaging*, 2nd ed. (Lippincott-Raven, Philadelphia, 1997).
- ⁴ F. M. Clements and N. P. de Bruijn, *Transesophageal Echocardiography* (Little, Brown, and Company, Boston, 1991).
- ⁵ K.-L. Chan, G. I. Cohen, R. A. Sochowski, and M. G. Baird, "Complications of transesophageal echocardiography in ambulatory adult patients: analysis of 1500 consecutive examinations," *J. Am. Soc. Echocardiogr.* **4**, 577-582 (1991).
- ⁶ W. G. Daniel, R. Erbel, W. Kasper, C. A. Visser, R. Engberding, G. R. Sutherland, E. Grube, P. Hanrath, B. Maisch, K. Dennig, M. Scharl, P. Kremer, C. Angermann, S. Iliceto, J. M. Curtius, and A. Mügge, "Safety of transesophageal echocardiography: a multicenter survey of 10,419 examination," *Circulation* **83**, 817-821 (1991).
- ⁷ A. D. Savakus, K. K. Shung, and N. B. Miller, "Distortions of ultrasonic field introduced by the rib cage in echocardiography," *J. Clin. Ultrasound* **10**, 413-419 (1982).
- ⁸ L. M. Hinkelman, T. L. Szabo, and R. C. Waag, "Measurements of ultrasonic pulse distortion produced by the human chest wall," *J. Acoust. Soc. Am.* **101**, 2365-2373 (1997).
- ⁹ Y. Y. Botros, E. S. Ebbini, and J. L. Volakis, "Two-step hybrid virtual array-ray (VAR) technique for focusing through the rib cage," *IEEE Trans. Ultrason. Ferroelectr. Freq. Control* **45**, 989-999 (1998).
- ¹⁰ T. D. Mast, L. M. Hinkelman, M. J. Orr, V. W. Sparrow, and R. C. Waag, "Simulation of ultrasonic pulse propagation through the abdominal wall," *J. Acoust. Soc. Am.* **102**, 1177-1190 (1997).
- ¹¹ L. M. Hinkelman, T. D. Mast, L. A. Metley, and R. C. Waag, "The effect of abdominal wall morphology on ultrasonic pulse distortion. Part I: Measurements," *J. Acoust. Soc. Am.* **104**, 3635-3649 (1998).
- ¹² T. D. Mast, L. M. Hinkelman, M. J. Orr, and R. C. Waag, "The effect of abdominal wall morphology on ultrasonic pulse distortion. Part II: Simulations," *J. Acoust. Soc. Am.* **104**, 3651-3664 (1998).
- ¹³ H. Kolsky, *Stress Waves in Solids* (Clarendon, Oxford, UK, 1953), pp. 106-129.
- ¹⁴ S. Leeman, L. Hutchins, and J. P. Jones, "Bounded pulse propagation," in *Acoustical Imaging*, edited by P. Alais and A. F. Metherell (Plenum, New York, 1982), Vol. 10, pp. 427-435.
- ¹⁵ S. Finette, "Computational methods for simulating ultrasound scattering in soft tissue," *IEEE Trans. Ultrason. Ferroelectr. Freq. Control* **34**, 283-292 (1987).
- ¹⁶ C. W. Manry and S. L. Broschat, "FDTD simulations for ultrasound propagation in a 2-D breast model," *Ultrason. Imaging* **118**, 25-34 (1996).
- ¹⁷ V. W. Sparrow and R. Raspet, "A numerical method for general finite amplitude wave propagation and its application to spark pulses," *J. Acoust. Soc. Am.* **90**, 2683-2691 (1991).
- ¹⁸ R. W. MacCormack, *Lecture Notes in Physics* (Springer-Verlag, Berlin, 1971), Vol. 8, p. 151.
- ¹⁹ D. Gottlieb and A. Turkel, "Dissipative two-four methods for time-dependent problems," *Math. Comput.* **30**, 703-723 (1976).
- ²⁰ E. Turkel, "On the practical use of high-order methods for hyperbolic systems," *J. Comput. Phys.* **35**, 319-340 (1980).
- ²¹ L. M. Hinkelman, L. A. Metley, C. J. Churukian, and R. C. Waag, "Modified Gomori trichrome stain for macroscopic tissue slices," *J. Histotech.* **19**, 321-323 (1996).
- ²² H. Gray, *Gray's Anatomy*, edited by T. P. Pick and R. Howden (Gramercy, New York, 1977), pp. 358-364 (facsimile of 1901 American edition of *Anatomy, Descriptive and Surgical*).
- ²³ R. Warwick and P. L. Williams, *Gray's Anatomy*, 35th ed. (Saunders, Philadelphia, 1973), pp. 488-490, 519-527.
- ²⁴ A. Elkeles, "Sex differences in the calcification of the costal cartilages," *J. Am. Geriatr. Soc.* **14**, 456-461 (1966).
- ²⁵ N. Bilaniuk and G. S. K. Wong, "Speed of sound in pure water as a function of temperature," *J. Acoust. Soc. Am.* **93**, 1609-1612 (1993).
- ²⁶ *Handbook of Chemistry and Physics*, edited by R. C. Weast (CRC Press, Boca Raton, 1985), p. F-10.
- ²⁷ S. A. Goss, R. L. Johnston, and F. Dunn, "Comprehensive compilation of empirical ultrasonic properties of mammalian tissues," *J. Acoust. Soc. Am.* **64**, 423-457 (1978).
- ²⁸ S. A. Goss, R. L. Johnston, and F. Dunn, "Compilation of empirical ultrasonic properties of mammalian tissues II," *J. Acoust. Soc. Am.* **68**, 93-108 (1980).
- ²⁹ J. E. Olerud, W. O'Brien, M. A. Riederer-Henderson, D. Steiger, F. K. Forster, C. Daly, D. J. Ketterer, and G. F. Odland, "Ultrasonic assessment of skin and wounds with the scanning laser acoustic microscope," *J. Invest. Dermatol.* **8**, 615-623 (1987).
- ³⁰ R. E. Neuman and M. A. Logan, "The determination of collagen and elastin in tissues," *J. Biol. Chem.* **186**, 549-556 (1950).
- ³¹ F. A. Duck, *Physical Properties of Tissue: A Comprehensive Reference Book* (Academic, New York, 1990).
- ³² K. T. Dussik and D. J. Fritch, "Determination of sound attenuation and sound velocity in the structure constituting the joints, and of the ultrasonic field distribution within the joints on living tissues and anatomical preparations, both in normal and pathological conditions," Progress Report to Public Health Service, National Institutes of Health Project A454, 15 September 1956.
- ³³ H. Q. Woodard and D. R. White, "The composition of body tissues" *Br. J. Radiol.* **59**, 1209-1219 (1986).
- ³⁴ International Commission on Radiation Units and Measurements, *ICRU Report 61: Tissue Substitutes, Phantoms, and Computational Modelling in Medical Ultrasound* (ICRU, Bethesda, MD, 1998), pp. 43-51.
- ³⁵ K. H. Herzfeld and T. A. Litovitz, *Absorption and Dispersion of Ultrasonic Waves* (Academic, New York, 1959), pp. 353-361.
- ³⁶ Simulations were performed on a Linux workstation with an AMD K6 processor running at 200 MHz and 128 MB of random-access memory. The simulation code was written in Fortran 77 and compiled using the front end fort77 and the Fortran-to-C converter f2c with the Gnu C compiler gcc.
- ³⁷ D.-L. Liu and R. C. Waag, "Correction of ultrasonic wavefront distortion using backpropagation and a reference waveform method for time-shift compensation," *J. Acoust. Soc. Am.* **96**, 649-660 (1994).
- ³⁸ L. M. Hinkelman, D.-L. Liu, L. A. Metley, and R. C. Waag, "Measurements of ultrasonic pulse arrival time and energy level variations produced by propagation through abdominal wall," *J. Acoust. Soc. Am.* **95**, 530-541 (1994).
- ³⁹ J. Wolff, *Das Gesetz der Transformation der Knochen* (Hirschwald, Berlin, 1982).
- ⁴⁰ J. C. Rice, S. C. Cowin, and J. A. Bowman, "On the dependence of the elasticity and strength of cancellous bone on apparent density," *J. Biomech.* **21**, 155-168 (1988).
- ⁴¹ J. Y. Rho, R. B. Ashman, and C. H. Turner, "Young's modulus of trabecular and cortical bone material: ultrasonic and tensile measurements," *J. Biomech.* **26**, 111-119 (1993).
- ⁴² C. H. Turner, J. Rho, Y. Takano, T. Y. Tsui, and G. M. Pharr, "The

- elastic properties of trabecular and cortical bone tissues are similar: results from two microscopic measurement techniques," *J. Biomech.* **32**, 437–441 (1999).
- ⁴³S. Lees, J. M. Ahern, and M. Leonard, "Parameters influencing the sonic velocity in compact calcified tissues of various species," *J. Acoust. Soc. Am.* **74**, 28–33 (1983).
- ⁴⁴S. Lees, "Sonic properties of mineralized tissues," in *Tissue Characterization with Ultrasound*, edited by J. F. Greenleaf (CRC Press, Boca Raton, 1986), pp. 207–226.
- ⁴⁵L. A. Frizzell, E. L. Carstensen, and J. F. Dyro, "Shear properties of mammalian tissues at low MHz frequencies," *J. Acoust. Soc. Am.* **60**, 1409–1411 (1976).
- ⁴⁶E. L. Madsen, H. J. Sathoff, and J. A. Zagzebski, "Ultrasonic shear wave properties of soft tissues and tissuelike materials," *J. Acoust. Soc. Am.* **74**, 1346–1355 (1983).
- ⁴⁷L. Adler and K. V. Cook, "Ultrasonic properties of freshly frozen dog tibia," *J. Acoust. Soc. Am.* **58**, 1107–1108 (1975).
- ⁴⁸S. S. Kohles, J. R. Bowers, A. C. Vailas, and R. Vanderby, "Ultrasonic wave velocity measurement in small polymeric and cortical bone specimens," *J. Biomech. Eng.* **119**, 232–236 (1997).
- ⁴⁹K. Chandra and C. Thompson, "Ultrasonic characterization of fractal media," *Proc. IEEE* **81**, 1523–1533 (1993).
- ⁵⁰L. M. Hinkelman and D.-L. Liu, "Measurement and analysis of ultrasonic pulse wavefront distortion produced by chest wall," *Proceedings of the 12th Annual University of Rochester Diagnostic Ultrasound Research Laboratory Industrial Associates Meeting*, 1995, pp. 8–25.
- ⁵¹T. D. Mast, A. I. Nachman, and R. C. Waag, "Focusing and imaging using eigenfunctions of the scattering operator," *J. Acoust. Soc. Am.* **102**, 715–725 (1997).

Appendix D

Validation of FFT-Based Algorithms for
Large-Scale Modeling of Wave Propagation in Tissue

Proceedings of the 2000 IEEE Ultrasonics Symposium

Vol. 2, pp. 1551–1556

Annual Report for DAMD17-98-1-8141, July 2000

Pages 47–52

Validation of FFT-Based Algorithms for Large-Scale Modeling of Wave Propagation in Tissue

John C. Mould, Gregory L. Wojcik, Laura M. Carcione, Makoto Tabei*,
T. Douglas Mast*, Robert C. Waag**

Weidlinger Associates, 4410 El Camino Real, Suite 110, Los Altos, CA 94022,

*University of Rochester, †Department of Electrical & Computer Engineering,

‡Departments of Electrical & Computer Engineering and Radiology, Rochester, NY 14642

*Applied Research Laboratory, The Pennsylvania State University, University Park, PA 16801

Abstract - We investigate accuracy of existing 2D pseudospectral and k-space formulations for simulating acoustic propagation in tissue or model scattering media. They are intended to provide insight into tissue-ultrasound interaction and a "test bed" for aberration correction schemes in medical imaging. Both methods employ FFT's to evaluate spatial derivatives to high accuracy on coarse grids. The primary difference lies in the approach to time integration. Scattering in large-scale, 2D, inhomogeneous media is included. We compare simulations against analytical solutions to illustrate spatial and temporal discretization required for acceptable solutions.

INTRODUCTION

The medium is represented by a uniform Cartesian grid where pressure/stiffness and velocity/density are unknowns/parameters at discrete points. Spectral operators in space enable accuracy and computational efficiency in very large models. However, inhomogeneities are often represented as piecewise constant from node to node, rather than smooth. The resulting stairstep can produce spurious diffractions at edges/corners, inaccurate reflections and transmissions at interfaces and local Gibbs phenomena, by approximating derivatives at a material discontinuity. Thus, the efficiency permitted by coarse spectral grids is compromised by the need to resolve interface derivatives.

For example, scattering by a soft cylinder requires only two nodes per wavelength inside and outside the cylinder for accurate propagation, but significantly more nodes per wavelength are necessary to reduce interface artifacts. Interface artifacts are quantified for a single interface, 1D

multilayer models, and cylindrical scatterers. Abdominal wall cross sections with coarse and fine-scale inhomogeneities are used to explore fidelity of wave propagation versus nodes per wavelength and tissue characteristic lengths. We show that the existing tools are useable in 2D.

The pseudospectral method is implemented in the *SpectralFlex* code. *Kbench* implements the k-space method.

PSEUDOSPECTRAL AND K-SPACE METHODS

The pseudospectral and k-space methods were formulated to provide efficient high-accuracy solutions to long range wave propagation problems. In fact, they debuted during the same year [1,2]. We briefly describe the two methods as implemented in [3,4], highlighting the major similarities and differences.

Both use FFT's to evaluate spatial derivatives to high accuracy on coarse grids. The primary difference lies in their respective approaches to time integration. Note that coarse spatial grids provide the primary incentive for FFT based (or any high order) method. The computational burden is linear in the number of timesteps per cycle, for both 2D and 3D. Including the timestep, computational burden is proportional to the number of Points Per Wave (PPW)³ in 2D or (PPW)⁴ in 3D.

SpectralFlex adopts a 4th order staggered Adams Bashforth ABS4 time integrator [5]. Among general purpose integrators, this is close to optimal for the current applications - 2-3 digits of accuracy for a wave propagating several hundred wavelengths on the coarsest possible grid. The stability limit for ABS4 in 2D is CFL = 0.3. The CFL number is defined as: $CFL = \Delta t / (\Delta x / c)$, where Δt is the timestep, c is the wavespeed and Δx is the cell size.

Accuracy frequently requires a smaller timestep, say CFL = 0.1. *Kbench* implements a time integrator in k-space based on the exact solution for waves propagating in a homogeneous medium [4]. It outperforms the general purpose ABS4 time integrator for weak scatterers in a homogeneous linear acoustic medium. ABS4 becomes more efficient when the scattering objects have a larger impedance contrast.

LONG RANGE PROPAGATION

To illustrate the advantages of the FFT based approach for long range propagation, we propagate a 2.5 MHz pulse 200 wavelengths through water using both *SpectralFlex* and *PZFlex*, a finite element code that is second order accurate in both space and time. The center frequency is 2.5 MHz, but spectral content is observable up to 5 MHz. Thus, 4 PPW at 2.5 MHz is the minimum sampling capable of resolving the pulse.

Figure 1 compares exact, *PZFlex* and *SpectralFlex* solutions. *SpectralFlex* used 4 PPW at CFL = 0.1, whereas *PZFlex* used 20 PPW at CFL = 0.8. These discretizations in time and space are typical of those that would be used in real problems. The *SpectralFlex* signal looks good and can be made better by reducing the timestep. The *PZFlex* signal is delayed in time and badly dispersed. A much finer grid is required to achieve reasonable accuracy. Note that at CFL = 1., *PZFlex* becomes a characteristic method, and produces exact results, even at 2 PPW. Unfortunately, this only works for 1D linear problems.

Kbench produces exact results for this example because the time integrator is based on the exact solution for a homogeneous medium.

DISCONTINUITIES

Spectral methods compute highly accurate spatial derivatives of smooth fields. Thus, in homogeneous regions, 2 cells per minimum wavelength (ie, highest spatial frequency) suffice. However, at material interfaces both the pressure and velocity fields should exhibit slope discontinuities as given by (1), where n denotes the normal direction and the

$$\frac{\partial p^+}{\partial n} = \frac{\rho^+}{\rho^-} \frac{\partial p^-}{\partial n} \quad (1)$$

superscript defines the + or - side of the interface. The velocity field likewise exhibits slope discontinuities at interfaces.

Spectral methods enforce smoothness, approximating the jumps in normal derivatives with steep gradients over a few cells. This approximation is quite good at 10-20 cells per wavelength, but less accurate at 2 cells per wavelength. For a staggered grid, as in *SpectralFlex*, the material interfaces coincide with velocity nodes, so we average the density at these interface points. On a regular grid, all the nodes lie away from interfaces, so no averaging is necessary, but the accuracy is even worse than for the staggered grid.

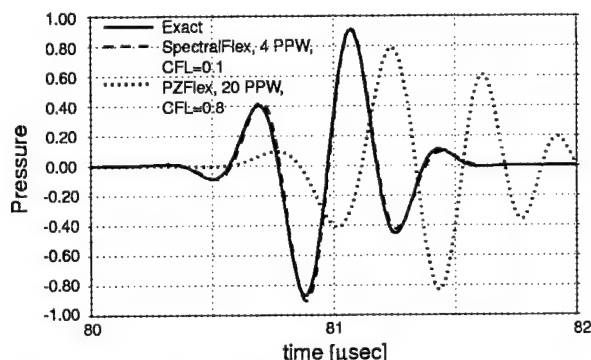


Figure 1. Long range pulse propagation through water.

1D versus exact solutions

Table 1 summarizes material properties used for the 1D benchmarks. Figure 2 illustrates the reflection/transmission of a normally incident pulse at a water/fat interface as modeled by *SpectralFlex*. To plotting accuracy, the transmitted signals appear exact (because it has much larger amplitude than the reflected wave). However, the error in the reflected signal is readily apparent at 4 PPW, and barely visible at 6 PPW.

Figure 3 shows results for a water /bone interface. In this case, errors are visible in both the reflected and transmitted signals at 4 PPW. In both codes, the most pathological case is varying density/constant stiffness. Fortunately, most tissues have a higher contrast in stiffness than density [6], so this worst case is seldom encountered. As shown in Fig. 4 (density=1000, 928 kg/m³) errors in the reflected wave are visible even at 12 PPW.

Table 1 – Material Properties for 1-D benchmarks

Material	Density [kg/m ³]	Wavespeed [m/sec]
Water	1000.	1500.
Fat	928.	1427.
Conn	1100.	1537.
Musl	1041.	1571.
Livr	1050.	1577.

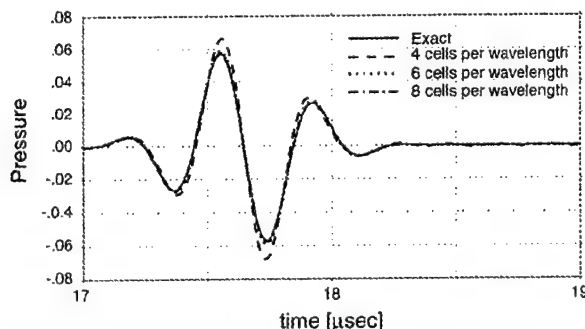


Figure 2. Reflected pulse at a water/fat interface.

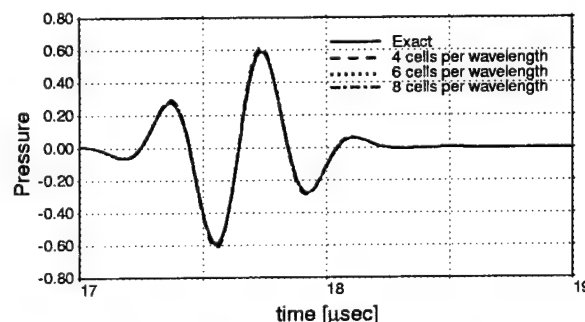


Figure 3. Reflected pulse at a water/bone interface.

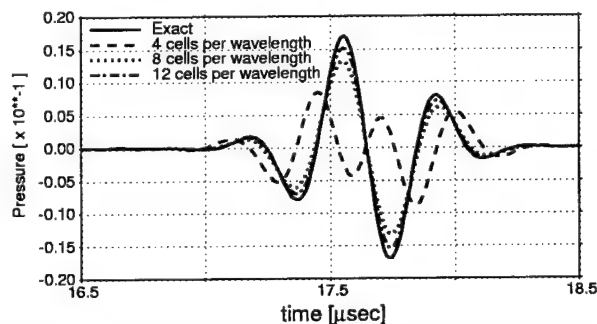


Figure 4. Reflected pulse from worst case interface.

The next benchmark examines propagation through a 1-D approximation of an abdominal cross section. Material parameters are again given in Table 1. Slight errors in the transmitted wave are apparent at 4 PPW (Fig. 5), but not at 8 PPW. Reflected signals (not shown) are similar. Figure 6

illustrates the effect of coarse non-conforming grids. At 4.1 PPW, cell boundaries are misaligned with actual material interfaces by up to $\frac{1}{2}$ cell. This is, of course, the case for any real model with discontinuous material properties. Properties are assigned based on the center of the cell. The errors introduced by this sampling dwarf all others. More will be said about this in a later section.

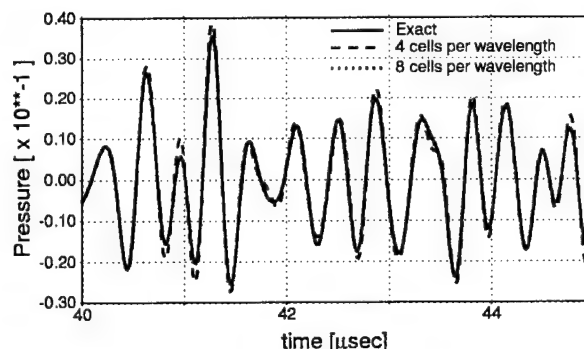


Figure 5. Pulse transmitted through 1-D abdominal wall model.

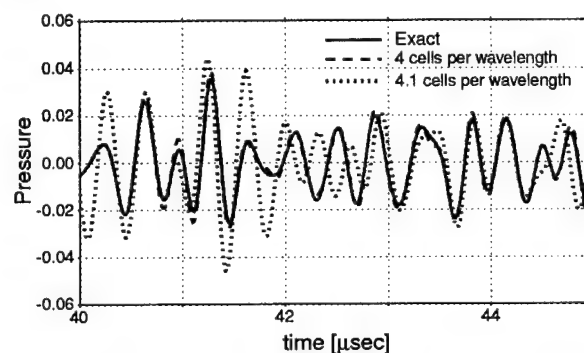


Figure 6. Pulse transmitted through 1-D approximation of abdominal wall. Non-conforming grid.

Scattering by cylinders

In addition to the numerical errors at interfaces, approximations are introduced by the stair-step representation of curved surfaces. To quantify these approximations, we consider 3 mm radius fat and bone cylinders immersed in water and insonified by the usual 2.5 MHz pulse. We compute the difference between exact and numerical signals for each timestep at 128 locations at 6 mm radius, and equal spacing in theta. We use the L^2 norm of this matrix as an error metric. Figure 7a shows the L^2 error vs PPW for *kbench* and *SpectralFlex* at CFL = 0.2.

The curves are similar, though *kbench* is slightly more accurate. For the larger contrast bone case in Figure 7b, similar trends are evident, but in this case *SpectralFlex* is more accurate. The error is tending to zero as the PPW increases. The rate of convergence is not quite quadratic. For context, Fig. 12 shows waveforms for L^2 error near 0.01.

Table 2 - Material Properties for Cylinders

Material	Wavespeed [m/sec]	Density [kg/m ³]
Water	1524.	993.
Fat	1478.	950.
Bone	3540.	1990.

Figure 7c illustrates that at low CFL, the error due to time integration tends to zero. For this problem, *kbench* permits reasonable accuracy at roughly double the *SpectralFlex* timestep. For the bone cylinder, the stability limit of *SpectralFlex* is 0.15 (0.3 in the bone), and *kbench* can go up to 0.2.

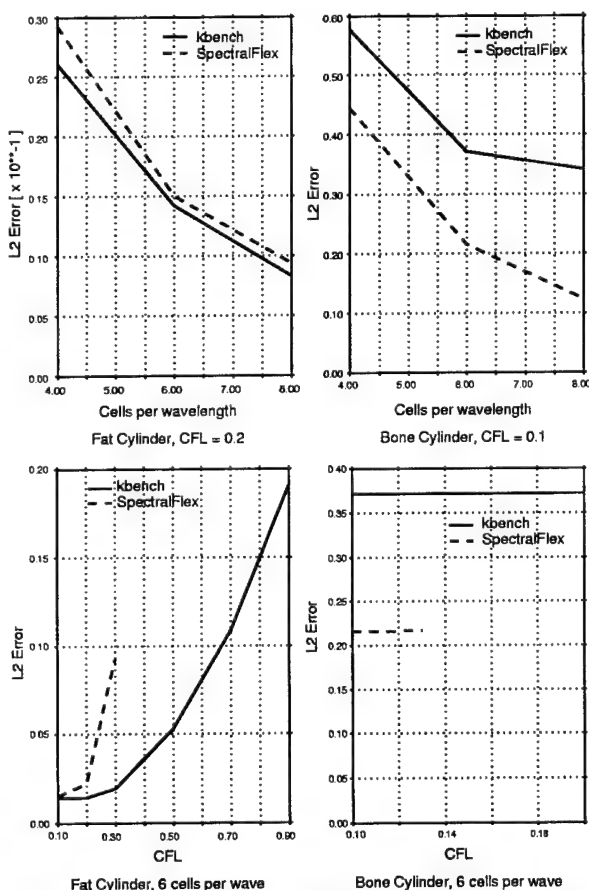


Figure 7. Cylinder benchmarks. Convergence with increasing discretization.

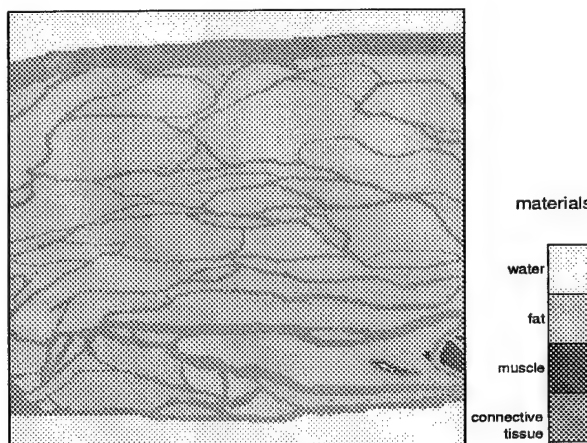


Figure 8. Abdominal wall model.

Tissue examples

Figure 8 shows an abdominal wall cross section [7,8]. This model is insonified by a 4.35 MHz plane wave pulse. Figure 9 displays typical reflected and transmitted signals computed by *SpectralFlex* at 4, 8 and 12 PPW. The grids were defined such that material boundaries always lie in exactly the same place. Again, it is confirmed that even the coarse 4 PPW model produces fairly accurate results.

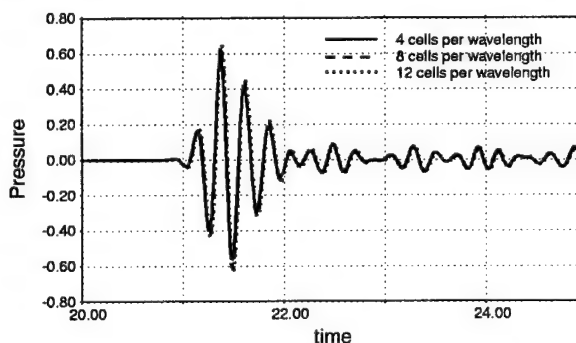


Figure 9. Transmitted pulse from Abdominal wall model.

INTERFACE TREATMENTS

Given that the largest numerical errors in the FFT based methods stem from material interfaces, we look at several interface treatments for reducing those errors.

Jump conditions

One possible method for improving the accuracy at interfaces is to split the solution into smooth and non-smooth parts, and apply the spectral method only to the smooth part. The idea is to introduce

local corrections at material interfaces that enforce the jump conditions exactly. E.g., construct low order polynomials over the cells adjacent to the interface that have zero value and zero slope 1 cell away, and, when added to the continuous part satisfy the jump condition (1) at the interface. Obviously, the correction is not required to be local, but if it covers more than 1 cell, the algorithm will become much more complicated for multiple interfaces. LaVeque [9] discusses such an approach applied to finite difference models.

Figure 10 compares reflected and transmitted signals for coarse models of an interface with and without the jump correction for interface velocity. This example isolates the effects of density changes in that only the density is discontinuous. The bulk modulus is continuous. The correction term improves the computed result, but not to the level of a homogeneous material. A similar correction could be applied to the discontinuity in the velocity gradients. However, it will have a weaker effect on the staggered grid since the leading coefficients are already continuous.

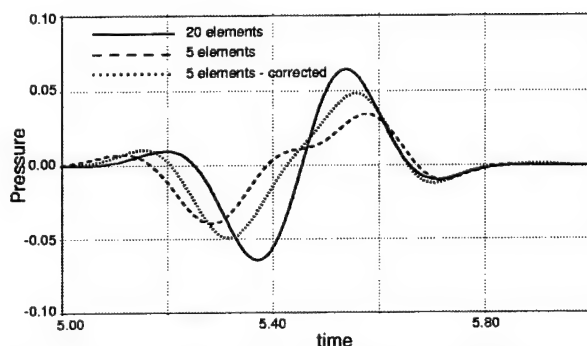
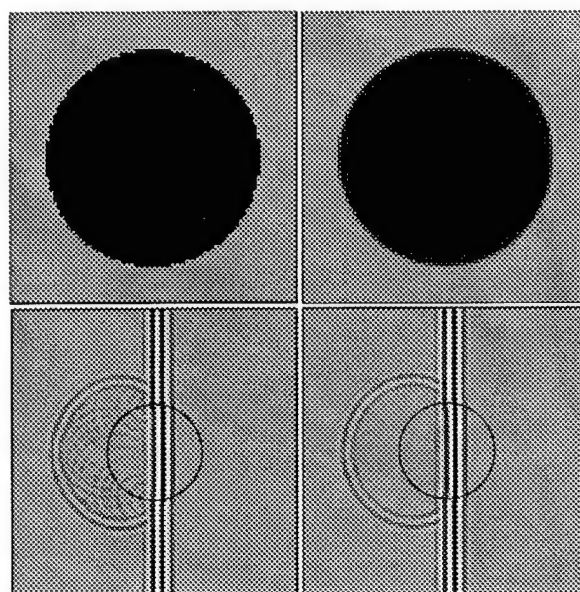


Figure 10. Jump treatment applied to interfaces.

Smoothing (Bandlimitation)

Another approach to improving accuracy at discontinuities is to smooth or bandlimit the model before sampling. This removes unresolvable high spatial frequencies from the model itself. We found that perfect bandlimitation reduced computed signals too much, but a "halfband" filter improves accuracy. The halfband filter is smooth with an amplitude of 0.5 at half the sampling frequency. Figure 11 shows direct and halfband filtered *kbench* models of a 3 mm cylinder using the same number of PPW. The corresponding pressure fields are plotted using a 60 dB bipolar log scale.



a) Unsmoothed b) Halfband Filtered
Figure 11. Direct sampled & bandlimited cylinders. Models and pressure, 60 dB bipolar log scale.

The staircase representation of the cylinder generates diffracted signals at each corner in 11a, but these have disappeared in 11b. Figure 12 shows selected waveforms from the direct and halfband sampled models. The late time diffractions have been removed, and overall L^2 error was reduced from 0.0155 to 0.0105. This exercise demonstrates that smoothing can be useful. However, there are some practical complications. The current procedure computes the smoothed object as the inverse transform of the object's analytical spectrum multiplied by the filter, and is thus defined only for objects with a known analytical spectrum. The extension to more general models defined on a pixel by pixel level has not yet been demonstrated. Also, continuous variations of material properties produce a large number of distinct materials. In the limit, each cell of the model has different properties. For the purely acoustic case, this presents little difficulty, but when material nonlinearity or viscoacoustic damping is added, the complexity intensifies. E.g., for each wavespeed/damping set, an optimization problem must be solved to compute the appropriate relaxation constants, and these constants must be stored.

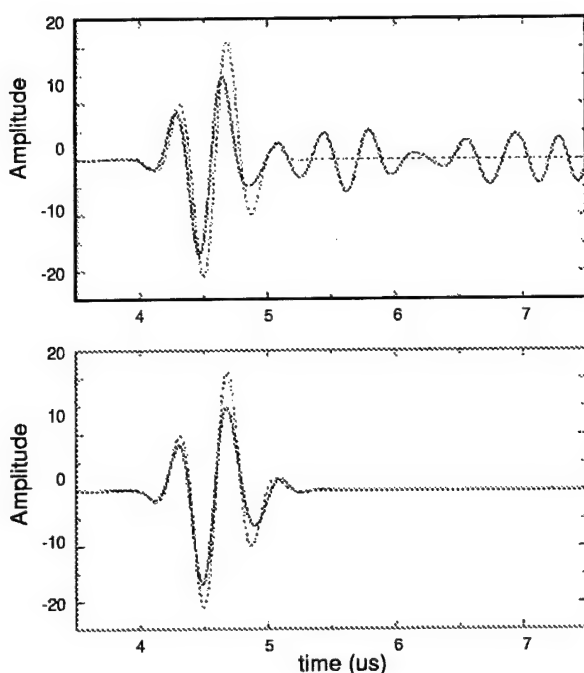


Figure 12. Backscattered signals from direct (top) and bandlimited (bottom) models.

Note that this procedure adds information to the model compared to the unsmoothed case. Because smoothing is applied to the analytical cylinder, the continuous variation of material constants provides a richer set of parameters than is available in the unsmoothed representation. As long as the model is known to higher resolution than the grid, information will be added. It is an interesting question whether smoothing would be beneficial on a grid finer than the pixel by pixel model definition. For example, the UOR tissue cross sections [7,8] are the most detailed models we know of. These are represented as piecewise constant with a pixel size 0.085 mm (about 7 PPW for a 2.5 MHz pulse). For a 5 MHz pulse, the coarsest grid would have finer resolution than the model.

Volume averaging of material constants has also been shown effective [10]. This adds additional information compared to the unsmoothed case, and the correction is more local than smoothing. However, the practical difficulties are the same.

As a last resort, increased discretization (brute force) will always converge to an accurate solution. This is a practical solution in 2D, as the above tissue examples indicate.

CONCLUSIONS

Model parameterization is a critical issue and puts all the above results in practical perspective. As shown above, differences in material constants or interface locations cause much larger differences in reflected/transmitted signals than any numerical errors in the FFT based methods. For gaining insight, or as a test-bed for aberration correction schemes, a 4 PPW model is sufficient at frequencies of 2.5 MHz or greater. Fine grids or cell-by-cell representation of material properties are needed only for more accurate rendition of model geometry.

ACKNOWLEDGEMENTS

Sponsored in part (JCM, GLW, LMC) by DARPA and ONR, and monitored by Dr. Wallace A. Smith.

REFERENCES

- [1] N.N. Bojarski, "k-space formulation of the acoustic scattering problem, *J. Acoust. Soc. Am.*, Vol. 53, 374, 1973, presented 84th mtg. ASA, 1972.
- [2] O. Kreiss and J. Oliger, "Comparison of accurate methods for the integration of hyperbolic equations," *Tellus*, vol. 24, 199-215, 1972.
- [3] G. Wojcik, B. Fornberg, R. Waag, L. Carcione, J. Mould, L. Nikodym, T. Driscoll, "Pseudospectral methods for large-scale bioacoustic models," *IEEE Ultrasonics Symp.* 1501-1506, 1997.
- [4] L.P. Souriau, T.D. Mast, D.L. Liu, A. Nachman and R.C. Waag, "A k-space method for large-scale models of wave propagation in tissue," *IEEE Trans. UFFC*, Submitted for publication, Feb. 1999.
- [5] M.B. Ghrist, B. Fornberg and T. Driscoll, "Staggered time integrators for wave equations," Preprint No. 394, Dept of Applied Math., Univ. of Colorado, Boulder, CO., 1998.
- [6] F.A. Duck, 1990, *Physical Properties of Tissue*, Academic Press.
- [7] L.M. Hinkelman, T.D. Mast, M.J. Orr, and R.C. Waag, "Effects of abdominal wall morphology on ultrasonic pulse distortion," *Proc. IEEE Ultrason. Symp.*, 1493-1496, 1997.
- [8] T.D. Mast, L.M. Hinkelman, M.J. Orr, V.W. Sparrow and R.C. Waag, "Simulation of ultrasonic pulse propagation through the abdominal wall," *J. Acoust. Soc. Am.*, 102, 1177-1190, 1997.
- [9] R. LaVeque, C. Zhang, "The Immersed Interface Method for Wave Equations with Discontinuous Coefficients," Univ. of Wash., Seattle WA, 1994.
- [10] F. Muir, J. Dellinger, J. Etgen and D. Nichols, "Modeling elastic fields across irregular boundaries," *Geophysics*, Vol. 57, No. 9, 1992.

Appendix E

A k -Space Method for Large-Scale Models of Wave Propagation in Tissue

To Appear in *IEEE Transactions on Ultrasonics,
Ferroelectrics, and Frequency Control*

Annual Report for DAMD17-98-1-8141, July 2000

Pages 53–86

A k -space method for large-scale models of wave propagation in tissue

T. Douglas Mast
Applied Research Laboratory
The Pennsylvania State University
University Park, PA 16801

Laurent P. Souriau
Department of Electrical and Computer Engineering
University of Rochester
Rochester, NY 14627

D.-L. Donald Liu
Ultrasound Group
Siemens Medical Systems
Issaquah, WA 98027

Makoto Tabei¹
Adrian I. Nachman²
Robert C. Waag³
Departments of Electrical and Computer Engineering,^{1,3}
Mathematics,² and Radiology³
University of Rochester
Rochester, NY 14627

Abstract

Large-scale simulation of ultrasonic pulse propagation in inhomogeneous tissue is important for study of ultrasound-tissue interaction as well as for development of new imaging methods. Typical scales of interest span hundreds of wavelengths; most current two-dimensional methods, such as finite-difference and finite-element methods, are unable to compute propagation on this scale with the efficiency needed for imaging studies. Furthermore, for most available methods of simulating ultrasonic propagation, large-scale three-dimensional computations of ultrasonic scattering are infeasible. Some of these difficulties have been overcome by previous pseudospectral and k -space methods, which allow substantial portions of the necessary computations to be executed using fast Fourier transforms. This paper presents a simplified derivation of the k -space method for a medium of variable sound speed and density; the derivation clearly shows the relationship of this k -space method to both past k -space methods and pseudospectral methods. In the present method, the spatial differential equations are solved by a simple Fourier transform method and temporal iteration is performed using a k - t space propagator. The temporal iteration procedure is shown to be exact for homogeneous media, unconditionally stable for "slow" ($c(\mathbf{x}) \leq c_0$) media, and highly accurate for general weakly scattering media. The applicability of the k -space method to large-scale soft-tissue modeling is shown by simulating two-dimensional propagation of an incident plane wave through several tissue-mimicking cylinders as well as a model chest wall cross section. A three-dimensional implementation of the k -space method is also employed for the example problem of propagation through a tissue-mimicking sphere. Numerical results indicate that the k -space method is accurate for large-scale soft-tissue computations, with much greater efficiency than that of an analogous leapfrog pseudospectral method or a 2-4 finite difference time-domain method. However, numerical results also indicate that the k -space method is less accurate than the finite-difference method for a high-contrast scatterer with bone-like properties, although qualitative results can still be obtained by the k -space method with high efficiency. Possible extensions to the method, including representation of absorption effects, absorbing boundary conditions, elastic-wave propagation, and acoustic nonlinearity, are discussed.

I. Introduction

Computation of a scattered acoustic field, given an incident wavefield and complete specification of an inhomogeneous medium, is known as the forward scattering problem. Numerical solution of the forward scattering problem is central to many aspects of ultrasonic imaging, including inverse scattering methods, numerical studies of wavefront distortion, and development of new methods for adaptive focusing. Most methods for numerical solution of the forward scattering problem fall into one of three categories: finite-difference methods, finite-element methods, and spectral methods.

Finite-difference and finite-element methods are known as local because the wave propagation equations of interest are solved at each point based only on conditions at nearby points. In contrast, spectral methods such as the k -space method [1]–[7] and the pseudospectral approach [8]–[14] are called global because information from the entire wavefield is employed to solve the wave propagation equations at each point. In part because of their global nature, spectral methods can be more accurate than local methods—for instance, pseudospectral methods applied to periodic problems have been shown to be equivalent to finite-difference methods of infinite order [12].

Spectral methods also have considerable advantages for large-scale forward solvers because the required storage and the number of operations per iteration can be dramatically reduced compared to local methods. This advantage occurs principally because spectral methods can allow computations to be performed on coarser grids while maintaining accuracy. For example, finite-element methods and high-order finite-difference methods typically require grid spacings on the order of ten points per minimum wavelength, while second-order finite-difference methods can require twenty points per wavelength [10]. Spectral methods, in theory, require only two points per wavelength (spatial Nyquist sampling), although for computations of propagation in inhomogeneous media, greater accuracy is achieved with grid spacings on the order of four points per wavelength [10, 11, 14].

This report addresses the problem of large-scale ultrasonic wave propagation in biological media such as human tissue. For problems of interest in medical ultrasound, domain sizes can often exceed the capabilities of conventional forward solvers. For example, one computation of realistic scale would be the simulated propagation of a pulse with an upper bandwidth limit of 5 MHz in a volume of dimensions 30 mm on each side and a nominal sound speed of 1.5 mm/ μ s, so that the minimum wavelength is 0.3 mm. For this computation, a second-order finite-difference

method (using twenty points per wavelength) would require a three-dimensional grid containing 8×10^9 nodes, a finite-element or fourth-order finite-difference method (using ten points per wavelength) would require 1×10^9 nodes, and a spectral method (using four points per wavelength) would require 6.4×10^7 nodes. Since a grid of 6.4×10^7 single-precision complex numbers requires storage of 512 megabytes, only spectral methods are feasible for realistic three-dimensional computations on present-day computers that typically have a maximum random-access memory storage of several gigabytes. The efficiency provided by fast Fourier transform implementations of spectral algorithms is a further reason why spectral methods are a practical approach to large-scale and three-dimensional computations of ultrasonic wave propagation.

Previous spectral approaches have included pseudospectral methods, in which spatial derivatives are evaluated globally by Fourier transformation and wavefields are advanced in time using various numerical integration techniques [8]–[14]. This method has provided high accuracy in many cases; however, temporal iteration techniques that provide good accuracy for large-scale models typically require small time steps, significant additional computations, or storage of wavefields from additional time steps [13], so that the efficiency advantages of the pseudospectral approach are less than might first be expected. The k -space family of methods [1]–[7] can overcome this problem by providing explicit temporal propagators related to the Green's function for wave propagation in k - t (spatial frequency and time) space.

The present paper presents a simplified derivation of the k -space method using a differential representation of the wave propagation equations. The spatial part of the wave propagation equations is solved by Fourier transformation in a manner analogous to past pseudospectral methods; this derivation is shown to be theoretically equivalent to previous integral formulations of the k -space method. Temporal iteration is performed using a k - t space propagator [2], which is shown to be exact for homogeneous media, and in general to provide much greater accuracy and stability than leapfrog iteration (in which temporal derivatives are evaluated using second-order-accurate finite differences) without significant additional computation or storage requirements. Thus, the k -space method provides spatial and temporal accuracy ideal for large-scale models of acoustic propagation in weakly scattering media.

Below, a derivation of the k -space method is presented for propagation in fluid media with spatially-dependent sound speed and density. For several canonical forward problems relevant to ultrasonic imaging, the accuracy and efficiency of the k -space method is compared to a pseudospectral method employing leapfrog iteration and to a 2-4 finite difference time-domain method.

The k -space and finite-difference methods are also used in an example computation for a large-scale two-dimensional tissue model. Another example computation illustrates the efficiency of the k -space method for three-dimensional scattering computations. Possible extensions of the present k -space method, including multiple relaxation effects for absorption, absorbing boundary conditions, inclusion of elastic and nonlinear acoustic effects, and parallelization, are discussed.

II. Theory

A. Derivation of the k -space method

The k -space method for solving the acoustic scattering problem is briefly derived below. The derivation is simpler than those previously published, and also provides some new insight regarding the remarkable accuracy and stability characteristics of the k -space method.

The method is applicable to large-scale modeling of linear ultrasonic propagation in soft tissues, which are modeled here as fluid media with spatially-dependent sound speed and density. Although the k -space method described below can be extended to include absorption effects, acoustic nonlinearity, and shear-wave propagation, these effects are neglected in this derivation for simplicity.

For a fluid medium with spatially-dependent sound speed and density, the linear acoustic wave equation is [15]

$$\nabla \cdot \left(\frac{1}{\rho(\mathbf{x})} \nabla p(\mathbf{x}, t) \right) - \frac{1}{\rho(\mathbf{x}) c(\mathbf{x})^2} \frac{\partial^2 p(\mathbf{x}, t)}{\partial t^2} = 0, \quad (1)$$

where $p(\mathbf{x}, t)$ is the acoustic perturbation in pressure, $\rho(\mathbf{x})$ is the spatially-dependent density, and $c(\mathbf{x})$ is the spatially-dependent sound speed.

By defining the normalized wavefield $f(\mathbf{x}, t) \equiv p(\mathbf{x}, t) / \sqrt{\rho(\mathbf{x})}$, as performed in a number of previous studies (*e.g.*, Refs. [16] and [17]), the first-order derivative term can be eliminated from Eq. (1). Details of this step are given in Ref. [6]. When the wavefield is also split into incident and scattered parts, such that $f(\mathbf{x}, t) = f_i(\mathbf{x}, t) + f_s(\mathbf{x}, t)$, a wave equation for the scattered field can then be written

$$\nabla^2 f_s(\mathbf{x}, t) - \frac{1}{c_0^2} \frac{\partial^2 f_s(\mathbf{x}, t)}{\partial t^2} = \frac{1}{c_0^2} \left(q(\mathbf{x}, t) + \frac{\partial^2 v(\mathbf{x}, t)}{\partial t^2} \right). \quad (2)$$

The terms on the right-hand side are effective sources associated with density and sound speed variations, defined as

$$q(\mathbf{x}, t) = c_0^2 \sqrt{\rho(\mathbf{x})} \nabla^2 \left(1 / \sqrt{\rho(\mathbf{x})} \right) f(\mathbf{x}, t) \quad (3)$$

and

$$v(\mathbf{x}, t) = \left(\frac{c_0^2}{c(\mathbf{x})^2} - 1 \right) f(\mathbf{x}, t). \quad (4)$$

The incident wavefield $f_i(\mathbf{x}, t)$ is required to satisfy the usual wave equation without any source terms (*i.e.*, the D'Alembertian operator from the left-hand side of Eq. (2), applied to $f_i(\mathbf{x}, t)$, is equal to zero). Thus, the total wavefield $f(\mathbf{x}, t)$ also satisfies Eq. (2) identically, so that the numerical algorithm developed below for the scattered field is equally applicable to the total field.

With the additional definition of an auxiliary field $w(\mathbf{x}, t) = f_s(\mathbf{x}, t) + v(\mathbf{x}, t)$, Eq. (2) can be rewritten in k -space as the coupled set of equations

$$\frac{\partial^2 W(\mathbf{k}, t)}{\partial t^2} = (c_0 k)^2 [V(\mathbf{k}, t) - W(\mathbf{k}, t)] - Q(\mathbf{k}, t), \quad (5)$$

$$V(\mathbf{k}, t) = \mathbf{F} \left[\left(1 - \frac{c(\mathbf{x})^2}{c_0^2} \right) [f_i(\mathbf{x}, t) + w(\mathbf{x}, t)] \right], \quad (6)$$

$$Q(\mathbf{k}, t) = c_0^2 \mathbf{F} \left[\sqrt{\rho(\mathbf{x})} \nabla^2 \left(\sqrt{\frac{1}{\rho(\mathbf{x})}} [f_i(\mathbf{x}, t) + w(\mathbf{x}, t) - v(\mathbf{x}, t)] \right) \right], \quad (7)$$

where \mathbf{F} denotes spatial Fourier transformation and capital letters indicate spatially Fourier transformed quantities.

For each point in k -space, Eq. (5) represents an independent ordinary differential equation equivalent to the standard simple-harmonic oscillator equation with the source terms $(c_0 k)^2 V$ and $-Q$. This ordinary differential equation can be discretized in several ways. For instance, a second-order accurate finite-difference representation of the second-order time derivative allows Eq. (5) to be written as

$$W(\mathbf{k}, t + \Delta t) - 2W(\mathbf{k}, t) + W(\mathbf{k}, t - \Delta t) \approx (c_0 k \Delta t)^2 \left[V(\mathbf{k}, t) - W(\mathbf{k}, t) - \frac{Q(\mathbf{k}, t)}{(c_0 k)^2} \right], \quad (8)$$

where Δt is the time step. This is known as "leapfrog" iteration; use of Eq. (8) in the current method is analogous to commonly used pseudospectral approaches [13, 14]. (Although increased accuracy can be achieved by higher-order methods such as fourth-order Adams-Bashforth or Adams-Moulton iteration, these methods have the disadvantage of requiring storage of the entire computational grid for additional time steps [12, 13].)

A more accurate form of the temporal iterator is obtained using a nonstandard finite difference approach. For the homogeneous simple harmonic oscillator equation, an exact discretization is known [18]. (That is, for any temporal and spatial step sizes, the discrete difference equations yield exactly the same solutions as the continuous differential equations. A similar exact discretization for the linear part of the Korteweg-de Vries equation was presented in Ref. [19].) Use of this nonstandard discretization leads to the following discrete form of Eq. (5):

$$W(\mathbf{k}, t + \Delta t) - 2W(\mathbf{k}, t) + W(\mathbf{k}, t - \Delta t) = 4 \sin^2 \left(\frac{c_0 k \Delta t}{2} \right) \left[V(\mathbf{k}, t) - W(\mathbf{k}, t) - \frac{Q(\mathbf{k}, t)}{(c_0 k)^2} \right]. \quad (9)$$

Because the discretization employed is exact for the simple harmonic oscillator equation, Eq. (9) is exactly equivalent to the differential equation (5) for the case of a homogeneous medium [*i.e.*, $V(\mathbf{k}, t) = Q(\mathbf{k}, t) = 0$]. Numerical results shown below indicate that high accuracy is also

achieved for weakly scattering media, in which case $V(\mathbf{k}, t) \ll W(\mathbf{k}, t)$ and $Q(\mathbf{k}, t) \ll W(\mathbf{k}, t)$. The present discretization method is equivalent to that employed by Bojarski (the form given in Ref. [2] follows after some trigonometric manipulation); however, previous derivations of this method have been based on approximations to an integral representation of Eq. (5) [2, 6]. It may also be noted that Eqs. (8) and (9) are equivalent in the limit of small Δt . However, results shown below indicate that, for weakly scattering media, use of the k - t propagator (9) provides much greater accuracy for larger time steps.

In numerical implementation of the k -space algorithm, Eq. (5) is used to advance the auxiliary field $W(\mathbf{k}, t)$ in time. Equations (6) and (7) represent updates of the effective scattering sources v and q and their spatial Fourier transformation to yield the k -space effective sources V and Q . Notable is that the effective source v is directly proportional to the square of the sound speed variation of the medium, while the effective source q is directly proportional to the Laplacian of $1/\sqrt{\rho(\mathbf{x})}$. Thus, for a piecewise-constant inhomogeneous medium, v may be non-zero everywhere while q is nonzero (and singular) only on borders between regions.

The present k -space algorithm can now be summarized as follows:

1. Set any initial conditions for $w(\mathbf{x}, t)$ and spatially Fourier transform (by FFT) to obtain initial conditions for $W(\mathbf{k}, t)$.
2. Define the incident wave $f_i(\mathbf{x}, t)$ on the entire grid ($f_i(\mathbf{x}, t)$ can be identically zero).
3. Compute $v(\mathbf{x}, t)$ and transform to obtain $V(\mathbf{k}, t)$ [Eq. (6)].
4. Compute $q(\mathbf{x}, t)$ and transform to obtain $Q(\mathbf{k}, t)$ [Eq. (7)].
5. Evaluate $W(\mathbf{k}, t + \Delta t)$ [Eq. (9)] and inverse transform to obtain $w(\mathbf{x}, t + \Delta t)$.
6. Set $t \rightarrow t + \Delta t$ and go to step (2).

This method requires three fast Fourier transform operations per time step (one each for steps 3, 4, and 5 of the algorithm enumerated above).

Also notable is that the algorithm is directly applicable to one-dimensional, two-dimensional, and three-dimensional propagation. This is possible because the k - t space Green's function has an identical form for any number of spatial dimensions [2]. For example, to implement the present

methods for two-dimensional computations, the algorithm outlined above is simply employed using two-dimensional Fourier transforms. The three-dimensional version of the algorithm is formally identical, but with three-dimensional Fourier transforms.

To distinguish between the standard leapfrog iteration method and the improved method used here, the following nomenclature is used in the present paper. The above algorithm employing Eq. (9) is referred to as a k -space method, while the corresponding algorithm employing Eq. (8) for temporal iteration is referred to as a leapfrog pseudospectral method. This nomenclature is used because the algorithm employing Eq. (9) is mathematically equivalent to an extended form of Bojarski's k -space method [2] cast in terms of differential equations rather than integral equations. The algorithm employing Eq. (8) is referred to as pseudospectral because it is mathematically equivalent to a conventional "method of lines" pseudospectral algorithm with leapfrog iteration [12]. (A conventional pseudospectral algorithm of this form would employ the spatial inverse Fourier transform of Eq. (8) for temporal iteration.)

B. Temporal and spatial sampling criteria

To determine the usable range of spatial and temporal sampling rates for the present k -space method, limits on the stability and accuracy of the method can be evaluated analytically.

The stability of the k -space and leapfrog pseudospectral methods derived above can be evaluated using standard, linear von Neumann stability analysis [20]. In this technique, the difference equations that comprise Eqs. (8) and (9) are applied to a test function

$$W_{\text{test}}(\mathbf{k}, n\Delta t) = \vartheta(\mathbf{k})^n \psi(\mathbf{k}), \quad (10)$$

where $\psi(\mathbf{k})$ is a spatial-frequency domain eigenmode and $\vartheta(\mathbf{k})$ is a temporal amplification factor. If a difference equation admits solutions with $|\vartheta(\mathbf{k})| > 1$ for any vector wavenumber \mathbf{k} , errors may grow exponentially with time and the solution is thus unstable. If $|\vartheta(\mathbf{k})| \leq 1$ for all wavenumbers, then the solution is numerically stable. For simplicity, the present stability computation is performed in the absence of density variations; the incident wave $f_i(\mathbf{x}, t)$ is assumed (without loss of generality) to be zero. To obtain limiting stability criteria, the worst-case sound speed inhomogeneity $c(\mathbf{x}) = c_{\text{max}}$ is also assumed.

Application of this technique to Eq. (8), which represents a leapfrog pseudospectral approach, yields a quadratic equation for $\vartheta(\mathbf{k})$. The resulting stability condition is

$$c_{\text{max}} k_{\text{max}} \Delta t \leq 2, \quad (11)$$

where c_{\max} is the maximum sound speed in the region of computation, $k_{\max} = \pi/\Delta x$ is the maximum wavenumber in the discrete Fourier transforms used to compute $W(\mathbf{k}, t)$, and Δt and Δx , respectively, are the temporal and spatial steps employed. Using the standard definition for a Courant-Friedrichs-Lewy (CFL) number [21], the stability condition

$$\text{CFL} \equiv \frac{c_0 \Delta t}{\Delta x} \leq \frac{2}{\pi} \frac{c_0}{c_{\max}} \quad (12)$$

is obtained for the leapfrog pseudospectral method represented by Eq. (8).

Application of the same analysis to the k -space iterator of Eq. (9) yields the stability condition

$$\sin \frac{\pi \text{CFL}}{2} < \frac{c_0}{c_{\max}}. \quad (13)$$

This condition has the remarkable result that, for media with $c(\mathbf{x}) \leq c_0$ everywhere, the linear numerical stability of the k -space method is unconditional. However, for any medium, an upper limit on the time step still arises from the requirement of sampling at the Nyquist rate: that is, the time step should be sufficiently small to allow two samples per period for the highest-frequency component of the computed field. Thus, the temporal sampling criterion can be written

$$\Delta t \leq \frac{1}{2f_{\max}} = \frac{\pi}{c_{\max} k_{\max}} = \frac{\Delta x}{c_{\max}}, \quad (14)$$

or simply $\text{CFL} \leq c_0/c_{\max}$. The stability criterion (13) is met whenever the Nyquist sampling criterion (14) is met; thus, the Nyquist sampling criterion is more restrictive.

For the spatial discretization, a Nyquist criterion based on the maximum spatial frequency $k_{\max} = \pi/\Delta x$ is met for any step size Δx . However, the inhomogeneous medium will be inaccurately represented (aliased) if its Fourier transform has significant spatial-frequency components beyond k_{\max} . Aliasing is a particular problem when the medium contains discontinuities (which correspond to infinite spatial-frequency content); removal of errors associated with discontinuities is discussed in the following section.

C. Effects of Discontinuities

The Fourier transforms performed in the present k -space algorithm can lead to numerical artifacts (related to the Gibbs phenomenon) when the inhomogeneous medium contains discontinuities in sound speed or density. To avoid such artifacts, the scattering object can be spatially filtered to smooth any discontinuities. That is, the spatially-dependent sound speed $c(\mathbf{x})$ and density $\rho(\mathbf{x})$

can be replaced by filtered functions of the form

$$u_{\text{filtered}}(\mathbf{x}) = \mathbf{F}^{-1}[U(\mathbf{k}) \phi(\mathbf{k})], \quad (15)$$

in which the Fourier transform $U(\mathbf{k})$ of the function $u(\mathbf{x})$ is multiplied by a low-pass spatial-frequency filter $\phi(\mathbf{k})$. The function $U(\mathbf{k})$ should be represented as accurately as possible; for example, exact Fourier transforms of simply-shaped inhomogeneities can be used when available. Below, the exact Fourier transform of a two-dimensional disk is employed for filtered representations of an infinite cylinder.

In the present study, the filter employed is the half-band filter [22]

$$\phi_H(k) = \begin{cases} 1, & k/k_{\max} < 1/2, \\ f(k/k_{\max} - 1/2), & 1/2 \leq k/k_{\max} \leq 3/2, \end{cases} \quad (16)$$

where

$$f(\theta) = \frac{1}{2} + \frac{9}{16} \cos(\pi\theta) - \frac{1}{16} \cos(3\pi\theta) \quad (17)$$

and k is the magnitude of the spatial-frequency vector \mathbf{k} .

This filter defines a smoothly tapered window that causes no attenuation of spatial frequencies below $k_{\max}/2$ and drops to half amplitude (-6 dB) at the spatial frequency k_{\max} . Zero amplitude is reached at the spatial frequency $3/2 k_{\max}$, which exceeds the spatial-frequency range of the discrete Fourier transforms employed in the k -space algorithm, so that aliasing error is not eliminated by the half-band filter. However, a strict bandlimiting filter was found to cause excessive loss of high-spatial-frequency components in the medium, so that scattering amplitude near the backscatter direction was greatly reduced. The half-band filter of Eq. (16) was found to greatly reduce Gibbs phenomenon artifacts while maintaining enough high-spatial-frequency components of inhomogeneities to provide accurate backscatter results.

For inhomogeneous media, exact Fourier transforms are not generally available. However, artifacts associated with discontinuities can still be removed by the methods given above. For example, a finely sampled representation of the medium could be filtered using Eq. (15) and then decimated to the desired spatial step size.

III. Numerical Methods

Numerical implementation of the k -space algorithm was accomplished using the algorithm described above. The normalized incident wave $f_i(\mathbf{x}, t)$ was defined as a plane wave with Gaussian temporal shape,

$$f_i(\mathbf{x}, t) = \rho(\mathbf{x})^{-\frac{1}{2}} \sin(\omega_0 \tau) e^{-\tau^2/(2\sigma^2)}, \quad (18)$$

where τ is the retarded time $\tau = t - (x - x_0)/c_0$ and x_0 is the initial central position of the wavefield. This incident wave was implicitly specified using initial conditions (as for the incident plane wave in Ref. [23]) rather than explicitly updated at each time step. Boundary conditions were implicitly periodic at each edge of the computational domain, due to the inherent periodicity of the fast Fourier transforms employed.

Wavefields were computed on two-dimensional grids large enough to avoid influence of “wraparound” error within the temporal window of interest. All k -space computations were performed on square grids of size N by N . Prior to execution of the main computation loop, the Laplacian occurring in Eq. (7) was evaluated using second-order accurate, centered finite-difference representations of the second derivative in each direction. Within the main computational loop, all spatial derivatives were evaluated by Fourier transformation, implemented using a fast Fourier transform (FFT) algorithm [24]. For maximum FFT efficiency, grid sizes N were chosen to be integers with prime factors no higher than 3.

To reduce any spatial anisotropy associated with the rectangular grid shape, the spatial-frequency time-domain wavefield $W(\mathbf{k}, t + \Delta t)$ was windowed using the radially symmetric window

$$\phi(\mathbf{k}) = H(k_{\max} - k) \quad (19)$$

before inversion to yield $w(\mathbf{x}, t + \Delta t)$. (That is, within step 5 in the algorithm enumerated above.) In Eq. (19), H is, as before, the Heaviside step function, k_{\max} is the maximum wavenumber magnitude (equal to $\pi/\Delta x$, since the spatial-frequency range sampled extends from $-\pi/\Delta x$ to $\pi/\Delta x$ in each direction), and k is the magnitude of the vector wavenumber \mathbf{k} . In some cases, the medium properties $c(\mathbf{x})$ and $\rho(\mathbf{x})$ were also smoothed by windowing in the spatial-frequency domain using Eq. (16) with a wavenumber cutoff of $k_{\max} = \pi/\Delta x$.

For comparison, wavefields were also computed using a second-order in time, fourth-order in space finite-difference method, described in Refs. [21], [23], and [25]–[27]. As for the k -space computations, the incident wave was specified by a single initial condition rather than updated at

each time step. Periodic boundary conditions were applied on all sides of the grid. Time steps were determined using a CFL number of 0.25, which is a natural choice for this finite-difference method [26]. As in Refs. [23] and [28], computations were performed at each time step only on portions of the grid where the wavefields were nonzero; this reduces the required computation time for the finite-difference method by about one half.

To test the k -space and finite-difference methods quantitatively, benchmark computations were performed using an exact series solution for the scattering of a plane wave by a fluid cylinder [29]. The sampling rate and waveform shape were chosen to match the time-domain simulation data for the case of interest. The pressure field was then computed for each frequency component with relative magnitude within 60 dB of the peak magnitude. Each single-frequency computation truncated the series at the term having a relative contribution less than 10^{-12} times the sum of all terms. The frequency-domain scattered fields were then inverted by FFT to obtain numerically exact solutions for the time-domain pressure fields at the simulated measurement points. An exact time-domain solution for scattering from a fluid sphere was also obtained using an analogous approach.

Benchmark studies of accuracy were performed using a cylinder with radius 2.0 mm and acoustic properties of human fat, and a background medium with acoustic properties of water at body temperature. Rationale for use of these values is discussed in Ref. [23]. The cylinder had a sound speed of 1.478 mm/ μ s and a density of 0.950 g/cm³, while the background medium had a sound speed of 1.524 mm/ μ s and a density of 0.993 g/cm³. The scattering geometry was as shown in Fig. 1. The incident pulse was a plane wave with Gaussian temporal characteristics, a temporal Gaussian parameter $\sigma = 0.25$ μ s, and a central starting position of $x = -4.5$ mm at time zero. For this pulse, a nominal maximum frequency is 4.43 MHz, corresponding to the spectral point 40 dB down from the center frequency (for the benchmark problem, this frequency corresponds to a minimum wavelength of 0.33 mm). The k -space, leapfrog pseudospectral, finite-difference, and exact methods described above were used to compute time histories of the total pressure field at 128 equally-spaced “measurement” points spanning a circle of radius 2.5 mm concentric to the cylinder. The pressure was interpolated using a two-dimensional lowpass interpolation filter implemented by the formula [30]

$$p_{\text{interp}}(x, y) = \sum_{x_i} \sum_{y_i} \frac{\sin(\pi(x - x_i)/\Delta x)}{\pi(x - x_i)/\Delta x} \frac{I_0[\beta(1 - [(x - x_i)/(m\Delta x)]^2)^{1/2}]}{I_0[\beta]} \\ \times \frac{\sin(\pi(y - y_i)/\Delta x)}{\pi(y - y_i)/\Delta x} \frac{I_0[\beta(1 - [(y - y_i)/(m\Delta x)]^2)^{1/2}]}{I_0[\beta]} \times p(x_i, y_i),$$

$$x - m\Delta x \leq x_i < x + m\Delta x,$$

$$y - m\Delta x \leq y_i < y + m\Delta x,$$

where I_0 is the zeroth-order modified Bessel function of the first kind and β is the Kaiser window coefficient, taken here to be 7.0. This choice of β provides a filter with flat response up to about $0.6 k_{\text{max}}$ and sidelobes at the -70 dB level.

The domain size for each k -space, pseudospectral, and finite-difference computation employing this cylinder was $18 \times 18 \text{ mm}^2$.

Further studies of accuracy were performed using a cylinder of radius 10 mm. Other parameters were as described above for the small problem, except that the radius of the measurement circle was 12.5 mm and the starting position of the wavefront was $x = -14.5$ mm. The k -space method was employed to compute two cases corresponding to unsmoothed and smoothed contrast functions, using a spatial step of four points per minimum wavelength and a CFL number of 0.5. In each k -space computation for this cylinder, the domain size employed was $72 \times 72 \text{ mm}^2$. The finite-difference method was employed to compute a single case, using a spatial step of fourteen points per minimum wavelength, a CFL number of 0.25, and a domain size of $72 \text{ mm} \times 60 \text{ mm}$.

To evaluate the relative accuracy and efficiency of the k -space and finite-difference methods for a high-contrast scatterer, computations were also performed using a cylinder of radius 2.0 mm with the sound speed and density of human bone. The values employed were a sound speed of $3.54 \text{ mm}/\mu\text{s}$ and a density of 1.99 g/cm^3 , as in Ref. [28]. The incident pulse, receiver, and computational domain characteristics were identical to those for the 2.0 mm "fat" cylinder case described above.

In all of the above accuracy tests, a quantitative measure of the accuracy was obtained using the time-domain L^2 error of each numerically computed pressure field $p_{\text{num}}(\mathbf{x}, t)$ versus the corresponding exact series solution $p_{\text{exact}}(\mathbf{x}, t)$. This quantity has the definition

$$\epsilon = \frac{\|p_{\text{num}}(\mathbf{x}_r, t) - p_{\text{exact}}(\mathbf{x}_r, t)\|}{\|p_{\text{exact}}(\mathbf{x}_r, t)\|}, \quad (20)$$

where $\|p(\mathbf{x}_r, t)\|$ is the L^2 norm [31] of a matrix composed of the time-domain signal $p(\mathbf{x}, t)$ for all receiver points \mathbf{x}_r and all time samples computed. Eq. (20) represents an accuracy criterion that is much stricter than more general criteria, such as comparison of the rms waveform amplitude or the amplitude and phase at the center frequency. To achieve a low L^2 error by the definition of Eq. (20), both the waveform amplitude and phase must be accurately computed for all significant frequency components of the field.

The use of the present k -space method in a more realistic two-dimensional simulation of ultrasonic propagation was also tested. For this purpose, a cross-sectional tissue map of the human chest wall [28] was used as the simulated medium. A pulse center frequency of 3.0 MHz was employed together with a temporal Gaussian parameter of $0.3127 \mu\text{s}$; these parameters correspond to the highest center frequency employed in the simulation study reported in Ref. [28]. The corresponding nominal minimum wavelength is 0.34 mm. The k -space computation employed 4 points per minimum wavelength, a CFL number of 0.5, and a grid size of $54.9 \times 54.9 \text{ mm}^2$. The finite-difference computation employed 14 points per minimum wavelength, a CFL number of 0.25, and a grid size of $38.5 \times 29.7 \text{ mm}^2$. As in Refs. [23] and [28], periodic boundary conditions were applied on the sides perpendicular to the wavefront, while first-order radiation boundary conditions [23] were applied on the sides parallel to the wavefront.

Finally, to illustrate the efficiency and accuracy of the present k -space method for three-dimensional computations, scattering from a penetrable sphere with acoustic properties of human muscle (speed $1.547 \text{ mm}/\mu\text{s}$, density $1.090 \text{ g}/\text{cm}^3$ [23]) was computed. The sphere radius was 1.5 mm; time-domain pressure waveforms were recorded at 128 equally-spaced measurement points on the sphere surface (in the $\phi = 0$ plane). The computation employed an incident pulse identical to that for the cylinder simulations described above, a spatial step of four points per minimum wavelength, and a CFL number of 0.5. The total pressure wavefield was computed for a time duration of $7.3 \mu\text{s}$ on a three-dimensional grid of dimensions $10.66 \times 10.66 \times 10.66 \text{ mm}^3$. The accuracy of this computation was assessed by evaluating the L^2 error between the k -space and exact solutions using Eq. (20).

IV. Numerical Results

An example k -space computation, performed using the 2.0 mm cylinder with acoustic properties of human fat, is illustrated in Fig. 1. The cylinder is also sketched in each panel. For the computation shown, smoothed sound speed and density functions were obtained by filtering the analytic spatial Fourier transform of the cylinder using Eq. (16). The time history of the total wavefield is shown as computed by the k -space method for a spatial step size of four points per minimum wavelength and a CFL number of 0.5. Details visible include a scattered wave from the edge nearest the initial wavefront (c), weak focusing near the trailing edge of the cylinder (e), scattering from the trailing edge [(f)–(i)], and low-level multiple scattering [(g)–(h)].

Results of accuracy benchmarks for the k -space and leapfrog pseudospectral methods described above are shown in Fig. 2. Each of these computations was made using the 2.0 mm radius cylinder described above and a spatial step size of four points per maximum wavelength. The results show that the k -space method employing the k - t space propagator of Eq. (9) provides much higher accuracy than the pseudospectral method employing the leapfrog propagator of Eq. (8). The two methods provide equivalent results for very small time steps (CFL numbers less than about 0.1), but the k -space method maintains its highest accuracy up to a CFL number of about 0.4. In contrast, the pseudospectral method rapidly increases in error for CFL numbers above 0.1.

Error results for the pseudospectral computations shown in Fig. 2 are not given for CFL numbers above 0.6 because the computation was unstable for higher CFL numbers. (That is, computed fields incurred spurious exponential growth, resulting in numerical overflow.) This observation of instability is consistent with the linear stability limit of 0.6366 given by Eq. (12) for this case. The k -space method did not incur any numerical instability for the range of CFL numbers investigated, so that the method is seen to be unconditionally stable as predicted for $c(\mathbf{x}) \leq c_0$. However, the error of this method grows as the CFL number approaches and exceeds unity, consistent with the Nyquist sampling criterion given by Eq. (14).

Pseudospectral methods employing higher-order time integration achieve higher accuracy than the leapfrog iteration used as a comparison here. However, tests of the present k -space method and a pseudospectral method employing fourth-order Adams-Bashforth time integration have shown trends similar to that seen in Fig. 2 [32]. Specifically, for weakly-scattering media, the k -space method yields similar accuracy for time steps two to three times larger than those required by the higher-order pseudospectral method described in Ref. [13].

The relative accuracy of the k -space method and the 2-4 finite difference method are compared in Fig. 3 as a function of the spatial step size. For these computations, the CFL number of the k -space computations was held constant at 0.5, consistent with the CFL-accuracy relationship shown in Fig. 2, while the CFL number of the finite-difference computations was held at 0.25 [26]. Both methods achieve high accuracy for finer grid spacings; however, the k -space method achieves higher accuracy for much larger spatial step sizes. The L^2 error drops below 0.05 for k -space computations employing only three points per minimum wavelength, while achievement of the same accuracy criterion requires 14 points per minimum wavelength for the finite-difference computations. This difference suggests that storage requirements for k -space computations can be much smaller than those for finite-difference computations of comparable accuracy: on the order of 12 times smaller for two-dimensional computations and 43 times smaller for three-dimensional computations.

Visual comparison of simulated waveforms for the 2.0 mm radius cylinder is shown in Fig. 4. Waveforms in this figure are those computed using the k -space (four points per minimum wavelength, CFL number 0.5, with both unsmoothed and smoothed contrast functions), finite-difference time-domain (14 points per minimum wavelength, CFL number 0.25), and exact methods. The k -space solution for the unsmoothed cylinder shows a small time-domain L^2 error (0.0243), but also exhibits spurious waves (nearly 60 dB down from the peak pressure amplitude) between the two main arrivals. These spurious waves are removed by use of the k -space method with smoothed medium parameters [*i.e.*, $\rho(\mathbf{x})$ and $c(\mathbf{x})$ smoothed using Eq. (16) with $k_{\max} = \pi/\Delta x$]; the L^2 error is decreased to 0.0214 by this smoothing. The finite-difference result bears a strong qualitative resemblance to the exact solution, but the larger L^2 error (0.0454) indicates that phase errors have been introduced by the dispersion inherent to the finite-difference method. Computation times [33] were 2.31 minutes for the k -space method and 1.55 hours for the finite-difference method, so that the k -space method yields greater accuracy at much less computational cost.

Waveforms for the 10 mm radius cylinder are shown in Fig. 5 in a format analogous to that of Fig. 4. These results indicate that, as for the smaller cylinder, smoothing of the contrast functions produces a reduction in spurious low-amplitude waves. For this problem, unlike the 2.0 mm radius cylinder discussed above, this smoothing slightly decreases the overall accuracy. (The time-domain L^2 error is 0.1292 for the smoothed case versus 0.1288 for the unsmoothed case.) The finite-difference solution, using 14 points per wavelength and a CFL number of 0.25, requires much greater storage and computational time, and produces waveforms with poorer accuracy (an L^2

error of 0.1794) than the k -space method.

Results for the 2 mm “bone” cylinder are shown in Fig. 6. In this case, the k -space method using a CFL number of 0.5 exhibited numerical instability. This instability is expected, since this CFL number exceeds the limit of 0.2833 set by Eq. (13). To obtain an appropriate temporal sampling rate, the time step was reduced in proportion to the increase in c_{\max} , resulting in a CFL number of 0.2153. Required computation time for the k -space method was 5.34 minutes [33]; the time-domain L^2 error was 0.3061 for the unsmoothed case and 0.2687 for the smoothed case.

The finite-difference method, employing 14 points per wavelength and a CFL number of 0.1076 (also changed in proportion to c_{\max}), achieved an L^2 error of 0.0350 in a computation time of 3.99 hours [33]. This result indicates that finite-difference methods can be much more accurate than k -space methods for scattering problems involving very high-contrast inhomogeneities such as bone within soft tissue. However, the k -space solution, as seen in Fig. 6, still shows good qualitative agreement with the exact solution.

The relative inaccuracy of the k -space method for high-contrast scatterers may be associated with aliasing effects, as suggested in Ref. [5]. That is, large jumps in spatial contrast functions are associated with significant high-frequency components of the corresponding k -space spectra. If the spatial-frequency range employed in the k -space algorithm is not sufficiently large, aliasing errors result. Low-pass filtering of the contrast functions would remove this aliasing, but also introduces additional errors because high spatial-frequency components of the scattering medium are lost. The half-band filtering employed here is a compromise that greatly reduces aliasing errors while maintaining some contributions from high spatial frequencies (up to the spatial Nyquist rate).

Computational results for a large-scale two-dimensional tissue model are shown in Fig. 7. Waveforms computed by the k -space (four points per minimum wavelength, CFL number 0.5, no smoothing) and the finite-difference (ten points per minimum wavelength, CFL number 0.25) were recorded at 130-element apertures composed of simulated point receivers separated by a pitch of 0.21 mm. The results produced by the finite-difference method and the k -space method are visually indistinguishable. However, despite the reduced grid size and limited computations employed for the finite-difference method, the k -space method was more efficient by about a factor of four; the required CPU time for the k -space method was 0.90 CPU hours, while the corresponding time for the finite-difference time-domain method was 4.58 CPU hours [33]. This discrepancy in efficiency is even more impressive when note is made that the k -space method using 4 points per minimum wavelength provides significantly higher accuracy than the finite-difference method using 14 points

per minimum wavelength (as illustrated in Fig. 3). Thus, the present k -space method is suggested to be an appropriate replacement for finite-difference methods previously employed to compute propagation through large-scale soft-tissue models [23]–[28].

Results of the example three-dimensional computation are shown in Fig. 8. Three-dimensional isosurface renderings of the total pressure wavefield are shown at three instants separated by $0.79 \mu\text{s}$. For the three-dimensional computation, the total computation time required was 1.51 hours [33]. The L^2 error of the computed waveforms, relative to the exact time-domain solution for scattering from a sphere [29], was 0.0186.

V. Extensions to the k -Space Method

The present method can be extended in a number of ways to increase its range of applicability in computations of ultrasound-tissue interactions.

Absorption effects could be added to the present algorithm in several ways. The most straightforward method for including absorption is to include an *ad hoc* damping term proportional to $\partial f_s / \partial t$ in Eq. (2) [3]–[5]. This approach yields absorption coefficients roughly independent of the frequency. Similarly, inclusion of a damping term proportional to $\partial^3 f_s / \partial t^3$ (a thermoviscous approximation) would lead to absorption roughly proportional to the frequency squared [34]. However, neither of these approaches has a rigorous justification for use in models of ultrasound propagation in biological tissue.

A physically justifiable approach for inclusion of absorption in the present algorithm is to consider absorption associated with multiple relaxation processes. The theoretical basis for this approach is presented in Ref. [35]; one implementation of this method in a finite-difference time-domain algorithm is given in Ref. [36]. Since multiple relaxation processes can lead to a variety of frequency-dependent absorption characteristics, this approach provides a possibility of modeling realistic frequency-dependent attenuation in tissue without introduction of nonphysical dispersion or violation of causality. Following the methods presented in Ref. [36], absorption due to multiple relaxation processes can be implemented in a computationally efficient form. Possible alternatives include the time-causal power law absorption formulation of Ref. [37].

Another possible extension to the present method is to incorporate the full elastic wave propagation equations. This extension would account for shear wave propagation, which may substantially affect results for propagation models including bone and other calcified tissue. By applying methods similar to those outlined in Ref. [7] to the algorithm described above, a full elastic k -space method incorporating Fourier-space evaluation of spatial derivatives and a k - t space propagator could be derived. Such a method would, as in Ref. [7], include separate k - t space propagators for compressional and shear waves.

Boundary conditions of k -space and pseudospectral methods are inherently periodic, so that simple radiation boundary conditions cannot be straightforwardly implemented. One option for absorbing boundary conditions is to include tapered (artificial) absorption functions at each boundary [38]. The technique of perfectly matched layers (PML) [39] can provide true radiation boundary conditions; however, present PML implementations are not applicable to the second-order wave

equation employed here. Combination of a k -space method with PML boundary conditions may require derivation of a new k - t space time integrator for the first-order wave propagation equations.

The present derivation was based on the linear (small-amplitude) acoustic propagation equations. The k -space method could be easily extended to incorporate finite-amplitude acoustic effects. For example, the nonlinear terms of the Westervelt propagation equation (used in Ref. [34] for modeling of ultrasonic propagation in tissue) could be included as effective source terms additional to the effective sources v and q defined above. The numerical results obtained above suggest that the k -space method is most accurate when the effective source terms are fairly small; thus, a nonlinear extension to the k -space method should be highly accurate for weakly nonlinear effects.

Computation times for the k -space method can easily be reduced by parallelization. The primary computational burden of the method is incurred in the multidimensional fast Fourier transforms (FFT) taken at each time step. Since FFT's can be efficiently executed on parallel processors [24, 40], the present k -space method should scale efficiently to large problems that require parallel processing.

VI. Conclusions

A simplified derivation of the k -space method for computation of ultrasonic wave propagation has been presented. The method efficiently accounts for sound speed and density variations, and can be extended to include realistic absorption effects and absorbing boundary conditions. Three-dimensional computations can also be performed without change to the algorithm as derived here.

Analytic and numerical results have shown that the present k -space method provides superior stability and accuracy over both a similar leapfrog pseudospectral method and a fourth-order space, second-order time, finite-difference method. This improved accuracy allows larger spatial and time steps to be employed, so that large-scale multidimensional computations are more feasible. Computations using a realistic two-dimensional tissue model support the conclusion that the k -space method provides high accuracy and low computational cost for large-scale computations.

The results also indicate that care should be taken when choosing and implementing a forward solver for a particular scattering problem. For instance, in the present k -space method, one can suppress spurious waves by smoothing sound speed and density variations; however, this smoothing does not decrease the time-domain L^2 error in some cases. Likewise, the finite-difference time-domain method employed here is less accurate than the k -space method in most cases examined here, but achieved higher accuracy for a test case with a bone-like scatterer. In general, the k -space method proposed here should be most applicable to large-scale scattering problems involving low-contrast inhomogeneities such as soft tissue structures.

Acknowledgments

The authors thank Fadil Santosa and Bengt Fornberg for helpful discussions. This research was funded by NIH Grants DK 45533, HL 50855, CA 74050, and 1R29CA81688, US Army Grant DAMD-17-98-1-8141, DARPA Grant N00014-96-0749, and the University of Rochester Diagnostic Ultrasound Research Laboratory Industrial Associates.

References

- [1] N. N. Bojarski, "The k -space formulation of the scattering problem in the time domain," *J. Acoust. Soc. Am.*, vol. 72, pp. 570–584, 1982.
- [2] N. N. Bojarski, "The k -space formulation of the scattering problem in the time domain: an improved single propagator formulation," *J. Acoust. Soc. Am.*, vol. 77, pp. 826–831, 1985.
- [3] B. Compani-Tabrizi, " K -space formulation of the absorptive full fluid elastic scalar wave equation in the time domain," *J. Acoust. Soc. Am.*, vol. 79, pp. 901–905, 1986.
- [4] S. Finette, "A computer model of acoustic wave scattering in soft tissue," *IEEE Trans. Biomed. Eng.*, vol. 34, pp. 336–344, 1987.
- [5] S. Finette, "Computational methods for simulating ultrasound scattering in soft tissue," *IEEE Trans. Ultrason., Ferroelect., Freq. Contr.*, vol. 34, pp. 283–292, 1987.
- [6] S. Pourjavid and O. J. Tretiak, "Numerical solution of the direct scattering problem through the transformed acoustical wave equation," *J. Acoust. Soc. Am.*, vol. 91, pp. 639–645, 1992.
- [7] Q. H. Liu, "Generalization of the k -space formulation to elastodynamic scattering problems," *J. Acoust. Soc. Am.*, vol. 97, pp. 1373–1379, 1995.
- [8] H.-O. Kreiss and J. Oliger, "Comparison of accurate methods for the integration of hyperbolic equations," *Tellus*, vol. 24, pp. 199–215, 1972.
- [9] B. Fornberg, "On a Fourier method for the integration of hyperbolic equations," *SIAM J. Numer. Anal.*, vol. 12, pp. 509–528, 1975.
- [10] D. Gottlieb and S. A. Orszag, *Numerical Analysis of Spectral Methods*, Philadelphia: SIAM, 1977.
- [11] D. C. Witte and P. G. Richards, "The pseudospectral method for simulating wave propagation," in *Computational Acoustics*, D. Lee, A. Cakmak, and R. Vichnevetsky, Eds., vol. 3, pp. 1–18, New York: North-Holland, 1990.
- [12] B. Fornberg, *A Practical Guide to Pseudospectral Methods*, Ch. 3, Cambridge: Cambridge University Press, 1996.

- [13] G. Wojcik, B. Fornberg, R. Waag, L. Carcione, J. Mould, L. Nikodym, and T. Driscoll, "Pseudospectral methods for large-scale bioacoustic models," *Proc. IEEE Ultrason. Symp.*, 1997, vol. 2, pp. 1501–1506.
- [14] Q. H. Liu, "The pseudospectral time-domain (PSTD) algorithm for acoustic waves in absorptive media," *IEEE Trans. Ultrason., Ferroelect., Freq. Contr.*, vol. 45, pp. 1044–1055, 1998.
- [15] A. D. Pierce, *Acoustics: an Introduction to its Physical Principles and Applications*, Second Edition, Ch. 1, Woodbury, New York: Acoustical Society of America, 1989.
- [16] S. A. Johnson and M. L. Tracy, "Inverse scattering solutions by a sinc basis moment method—Part I: theory," *Ultrason. Imag.*, vol. 5, pp. 361–375, 1983.
- [17] A. Nachman, "Reconstructions from boundary measurements," *Ann. Math.*, vol. 128, pp. 531–576, 1988.
- [18] R. E. Mickens, *Nonstandard Finite Difference Models of Differential Equations*, Singapore: World Scientific, 1994.
- [19] B. Fornberg and G. B. Whitham, "A numerical and theoretical study of certain nonlinear wave phenomena," *Phil. Trans. Royal Soc. London*, vol. 289, pp. 373–404, 1978.
- [20] E. H. Twizell, *Computational Methods for Partial Differential Equations*, New York: Ellis Horwood Limited, 1984.
- [21] E. Turkel, "On the practical use of high-order methods for hyperbolic systems," *J. Comp. Phys.*, vol. 35, pp. 319–340, 1980.
- [22] R. E. Crochiere and L. R. Rabiner, *Multirate Digital Signal Processing*, Englewood Cliffs, NJ: Prentice-Hall, 1983.
- [23] T. D. Mast, L. M. Hinkelman, M. J. Orr, V. W. Sparrow, and R. C. Waag, "Simulation of ultrasonic pulse propagation through the abdominal wall," *J. Acoust. Soc. Am.*, vol. 102, pp. 1177–1190, 1998. [Erratum: *J. Acoust. Soc. Am.*, vol. 104, pp. 1124–1125, 1998.]
- [24] M. Frigo and S. G. Johnson, "FFTW: An adaptive software architecture for the FFT," *Proceedings of the ICASSP*, vol. 3, pp. 1381–1384, 1998.

- [25] R. W. MacCormack, "Numerical solution of the interaction of a shock wave with a laminar boundary layer," in *Lecture Notes in Physics*, J. Ehlers, K. Hepp, and H. A. Weidenmüller, Eds., vol. 8, pp. 151–163, Berlin: Springer-Verlag, 1971.
- [26] D. Gottlieb and A. Turkel, "Dissipative two-four methods for time-dependent problems," *Math. Comp.*, vol. 30, pp. 703–723, 1976.
- [27] V. W. Sparrow and R. Raspet, "A numerical method for general finite amplitude wave propagation and its application to spark pulses," *J. Acoust. Soc. Am.*, vol. 90, pp. 2683–2691, 1991.
- [28] T. D. Mast, L. M. Hinkelman, M. J. Orr, and R. C. Waag, "Simulation of ultrasonic pulse propagation, distortion, and attenuation in the human chest wall," *J. Acoust. Soc. Am.*, vol. 106, pp. 3665–3677, 1999.
- [29] P. M. Morse and K. U. Ingard, *Theoretical Acoustics*, Ch. 8, New York: McGraw-Hill, 1968.
- [30] A. V. Oppenheim and R. W. Schaffer, *Discrete-Time Signal Processing*, Ch. 7, Englewood Cliffs, New Jersey: Prentice Hall, 1989.
- [31] R. L. Burden, J. D. Faires, and A. C. Reynolds, *Numerical Analysis*, Ch. 8, Boston: Prindle, Weber, and Schmidt, 1978.
- [32] J. C. Mould, G. L. Wojcik, L. M. Carcione, M. Tabei, T. D. Mast, and R. C. Waag, "Validation of FFT-based algorithms for large-scale modeling of wave propagation in tissue," *Proc. IEEE Ultrason. Symp.*, 1999.
- [33] All CPU timings reported in this paper were obtained using a Linux workstation with a 200 MHz AMD K6 processor and 128 MB RAM.
- [34] I. M. Hallaj and R. O. Cleveland, "FDTD simulation of finite-amplitude pressure and temperature fields for biomedical ultrasound," *J. Acoust. Soc. Am.*, vol. 105, pp. L7–L12, 1999.
- [35] A. I. Nachman, J. Smith, and R. C. Waag, "An equation for acoustic propagation in inhomogeneous media with relaxation losses," *J. Acoust. Soc. Am.*, vol. 88, pp. 1584–1595, 1990.
- [36] X. Yuan, D. Borup, J. Wiskin, M. Berggren, and S. Johnson, "Simulation of acoustic wave propagation in dispersive media with relaxation losses by using FDTD method with PML

absorbing boundary condition," *IEEE Trans. Ultrason., Ferroelect., Freq. Contr.*, vol. 46, pp. 14–23, 1999.

- [37] T. L. Szabo, "Time domain wave equations for lossy media obeying a frequency power law," *J. Acoust. Soc. Am.*, vol. 96, pp. 491–500, 1994.
- [38] C. Cerjan, D. Kosloff, R. Kosloff, and M. Reshef, "A nonreflecting boundary condition for discrete acoustic and elastic wave equations," *Geophysics*, vol. 50, pp. 705–708 (1985).
- [39] J.-P. Berenger, "A perfectly matched layer for the absorption of electromagnetic waves," *J. Comput. Phys.*, vol. 114, pp. 185–200, 1994.
- [40] P. N. Swarztrauber, "Multiprocessor FFTs," *Parallel Computing*, vol. 5, pp. 197–210, 1987.

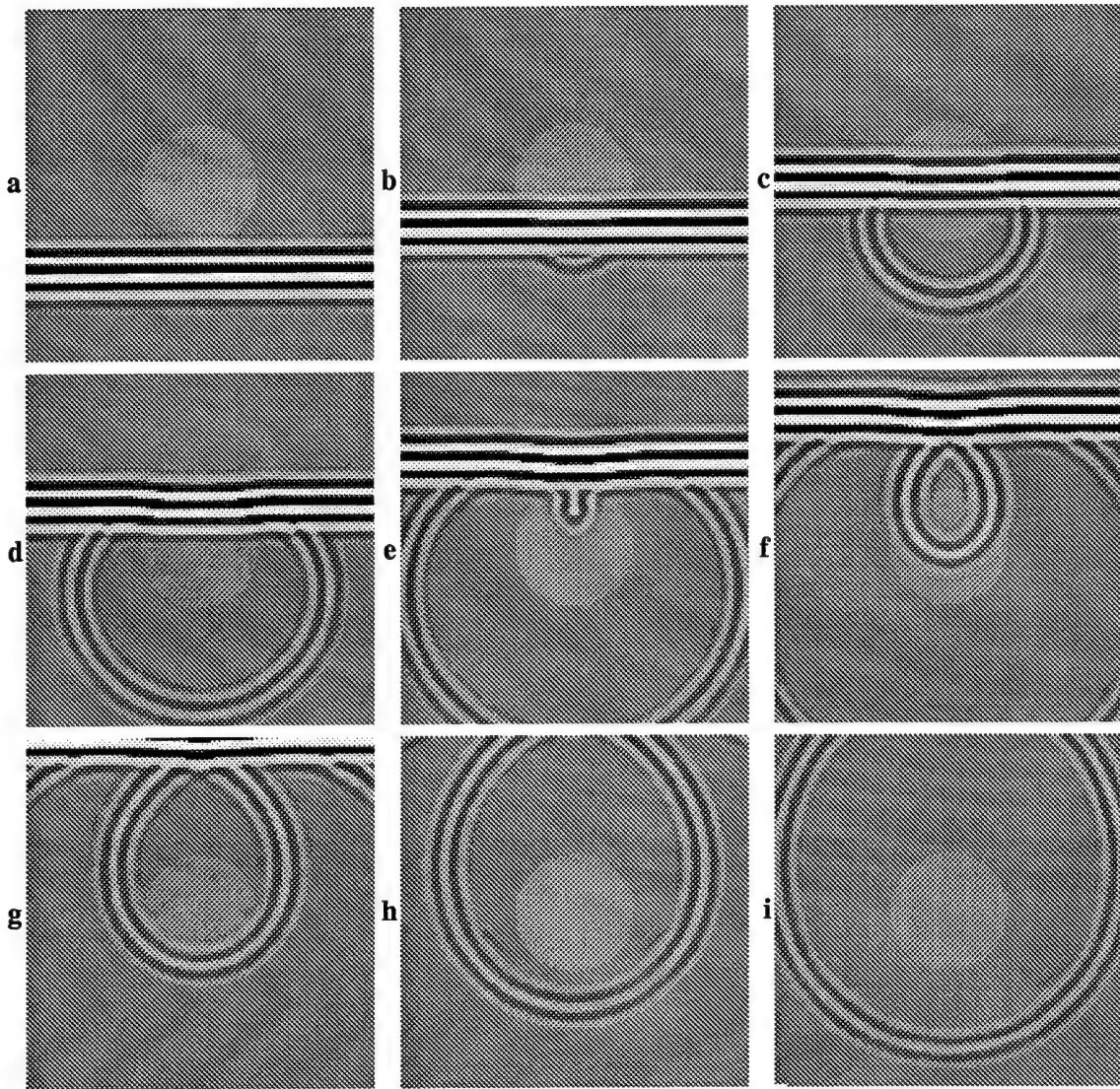


Figure 1: Time history of total acoustic pressure computed by the k -space method for a cylinder of 2.0 mm radius and fat-mimicking acoustic properties. The cylinder is sketched as a light gray region. The first panel shows the wavefield impinging on the cylinder at time $t = 0.98 \mu\text{s}$ and subsequent panels (progressing from left to right and top to bottom) show the total wavefield at intervals of $0.98 \mu\text{s}$. The acoustic pressure is plotted in all panels using a bipolar logarithmic scale with a 60 dB dynamic range.

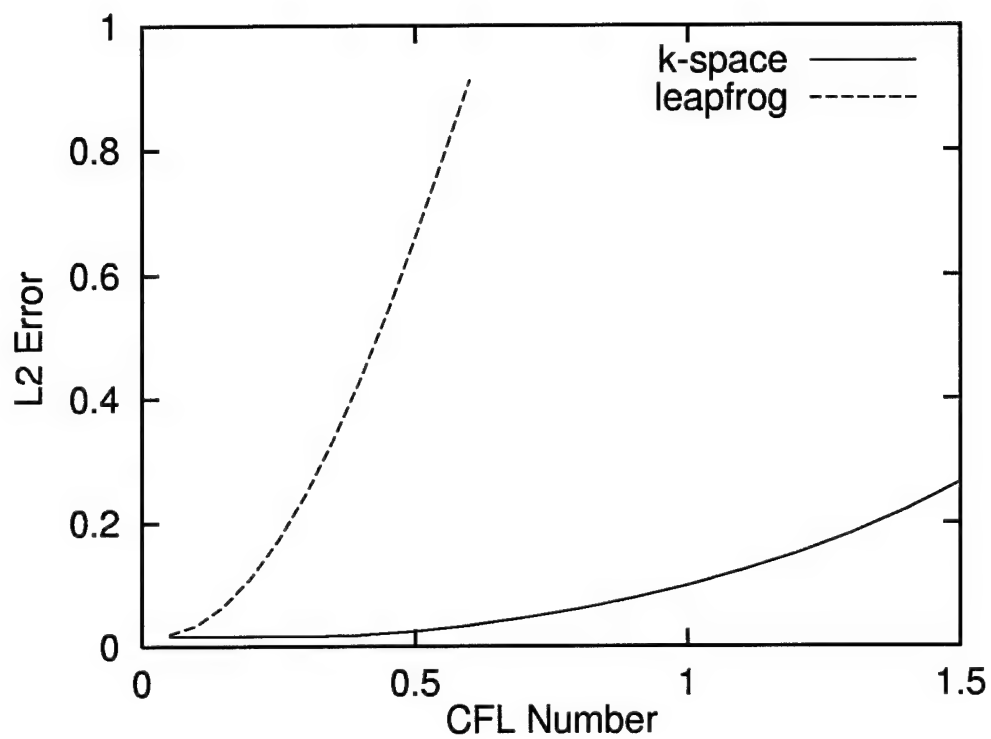


Figure 2: Time-domain comparison of accuracy for the k -space and leapfrog pseudospectral methods as a function of CFL number. Each test used the “fat” cylinder of 2.0 mm radius and a spatial step size of four points per minimum wavelength.

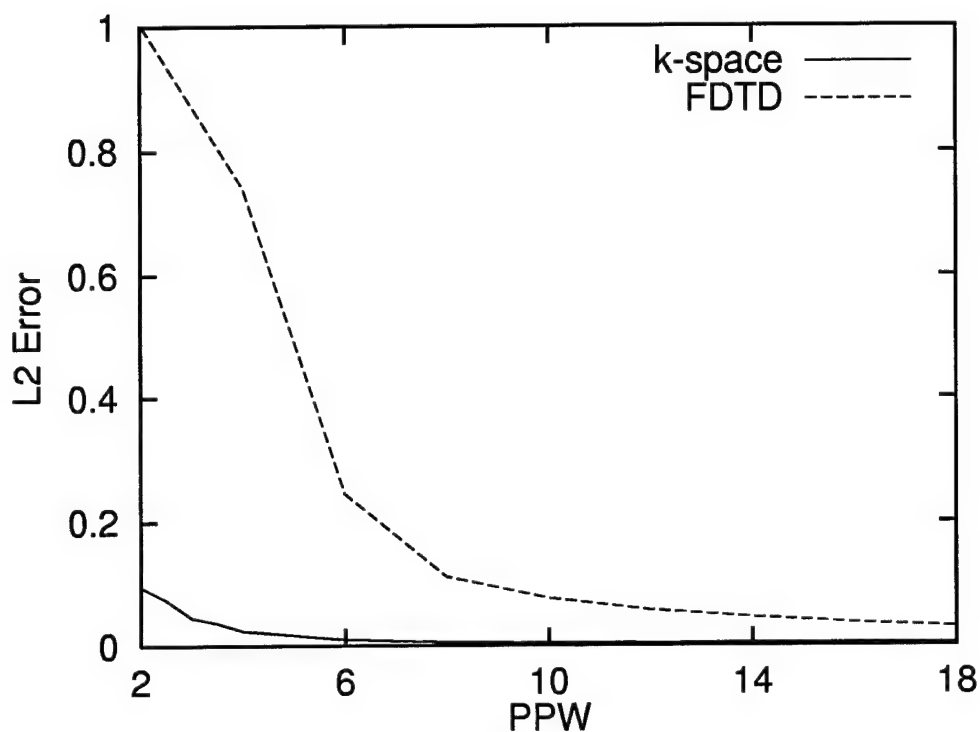


Figure 3: Time-domain comparison of accuracy for the k -space and 2-4 finite-difference time-domain methods as a function of the spatial step size in points per minimum wavelength (PPW). Each test used the “fat” cylinder of 2.0 mm radius. CFL numbers were 0.5 for the k -space method and 0.25 for the finite-difference time-domain method.

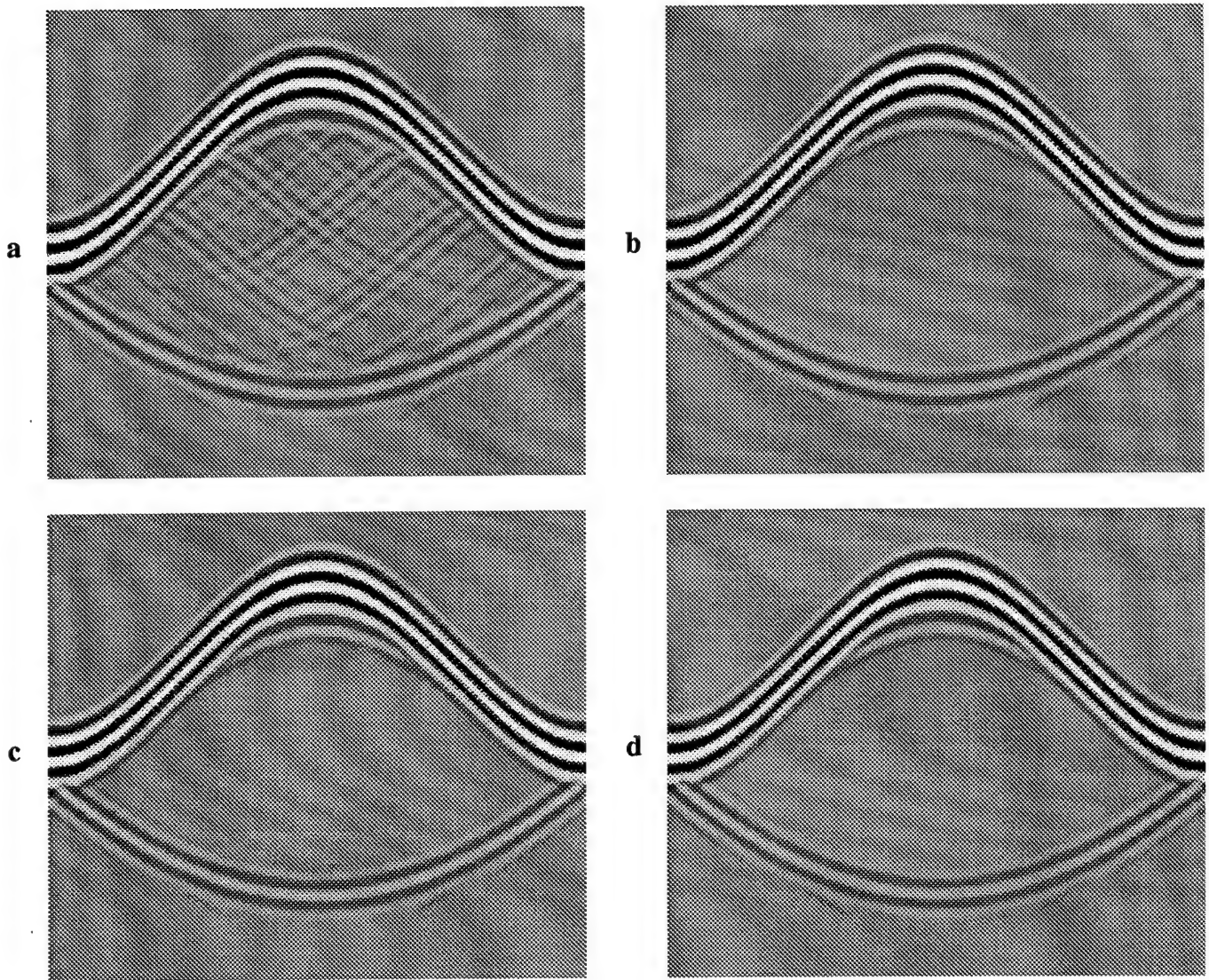


Figure 4: Computed waveforms for the “fat” cylinder at a radius of 2.5 mm for a cylinder of radius 2.0 mm and a pulse center frequency of 2.5 MHz. The acoustic pressure is shown on a bipolar logarithmic scale with 60 dB dynamic range. The horizontal range of each plot is 360 degrees, covering the entire measurement circle starting with angle 0 (forward propagation). The vertical range of each panel corresponds to a temporal duration of 9 μ s, with $t = 0$ at the top of each plot. (a) Unsmoothed object; k -space solution with four points per minimum wavelength, L^2 error 0.0243. (b) Smoothed object; k -space solution with four points per minimum wavelength, L^2 error 0.0214. (c) Finite-difference solution with 14 points per minimum wavelength, L^2 error 0.0454. (d) Exact solution.

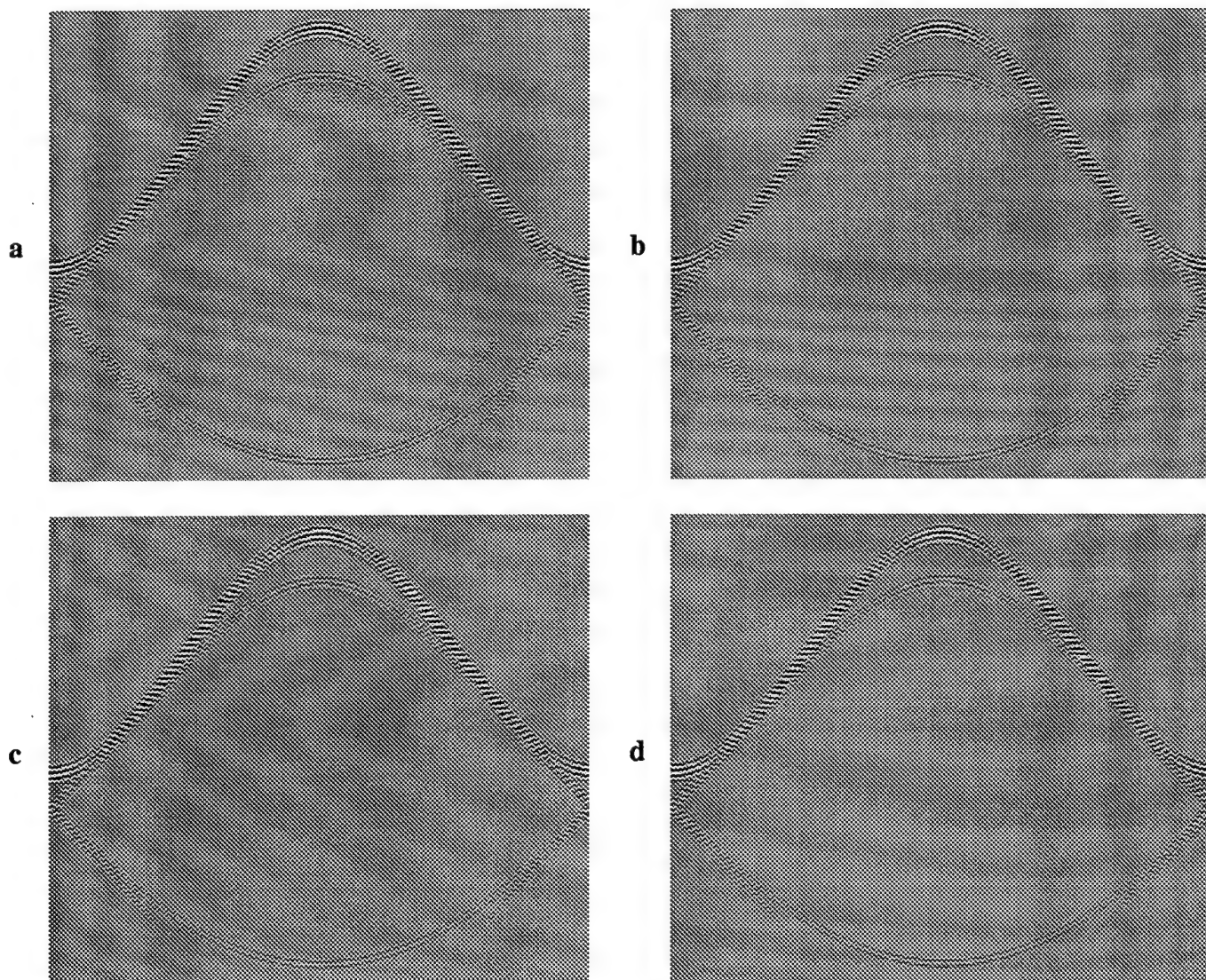


Figure 5: Computed waveforms at a radius of 12.5 mm for a “fat” cylinder of radius 10.0 mm and a pulse center frequency of 2.5 MHz. The acoustic pressure is shown in each panel using a bipolar logarithmic scale with a 60 dB dynamic range. The horizontal range of each panel is 360 degrees and the vertical range is 33 μ s. (a) Unsmoothed object; k -space solution, L^2 error 0.1288. (b) Smoothed object; k -space solution, L^2 error 0.1292. (c) Finite-difference solution, L^2 error 0.1794. (d) Exact solution.

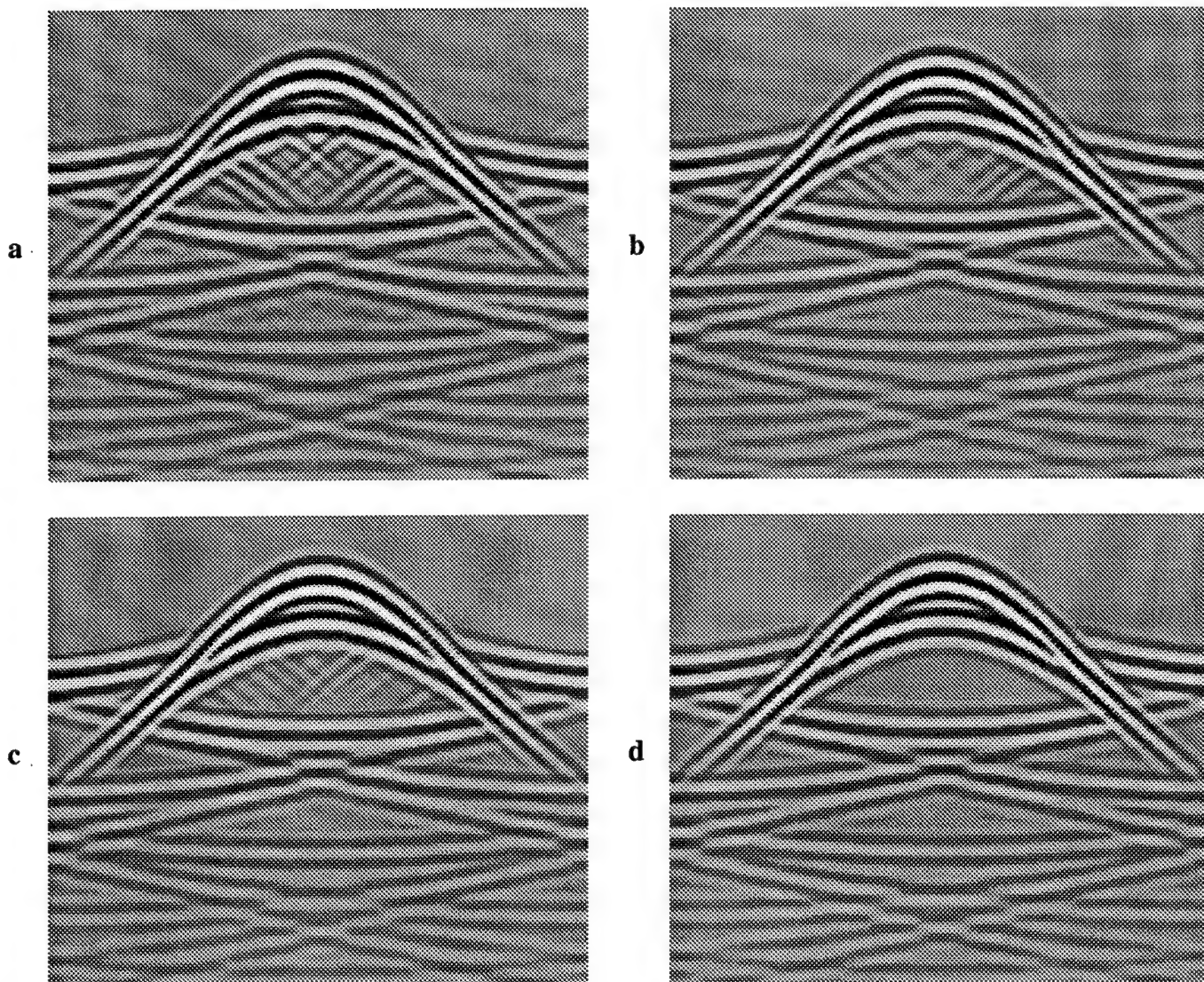


Figure 6: Computed pressure waveforms at a receiver radius of 2.5 mm for a “bone” cylinder of radius 2.0 mm and a pulse center frequency of 2.5 MHz. The format is the same as in Fig. 4. (a) Unsmoothed object; k -space solution, L^2 error 0.3061. (b) Smoothed object; k -space solution, L^2 error 0.2687. (c) Finite-difference solution, L^2 error 0.0380. (d) Exact solution.

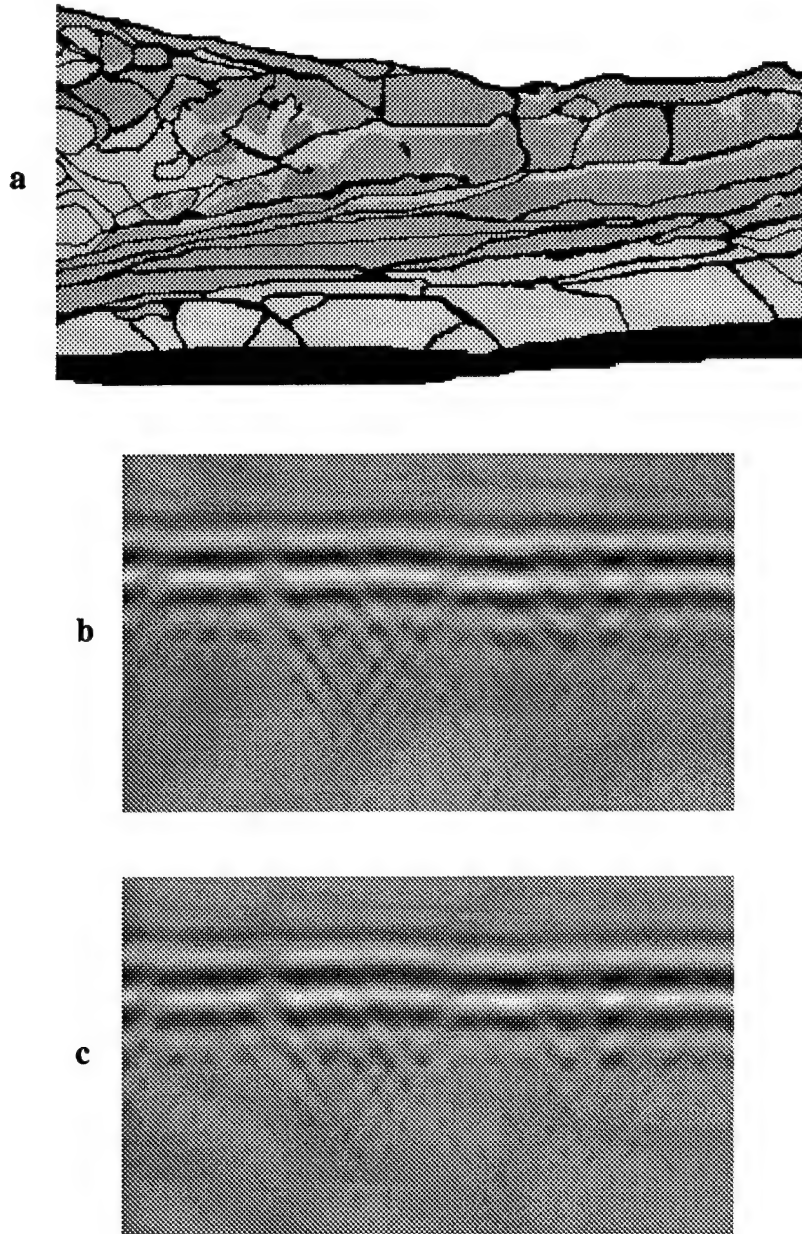


Figure 7: Comparison of k -space and finite-difference methods for a tissue cross-sectional model. (a) Chest wall cross section (taken from Ref. [24]), with black indicating connective tissue, dark gray indicating muscle, and light gray indicating fat. The region is 33.5 mm wide and 17.2 mm high. (b) Transmitted waveforms computed by the k -space method using four points per minimum wavelength and a CFL number of 0.5, shown on a bipolar linear gray scale with white indicating maximum positive pressure and black indicating maximum negative pressure. The horizontal range shown is 27.3 mm and is shown to the same scale as in (a). The vertical range is 3.29 μ s. (c) Transmitted waveforms computed by the finite-difference time-domain method using 10 points per minimum wavelength and a CFL number of 0.25, shown using the same format as in (b).

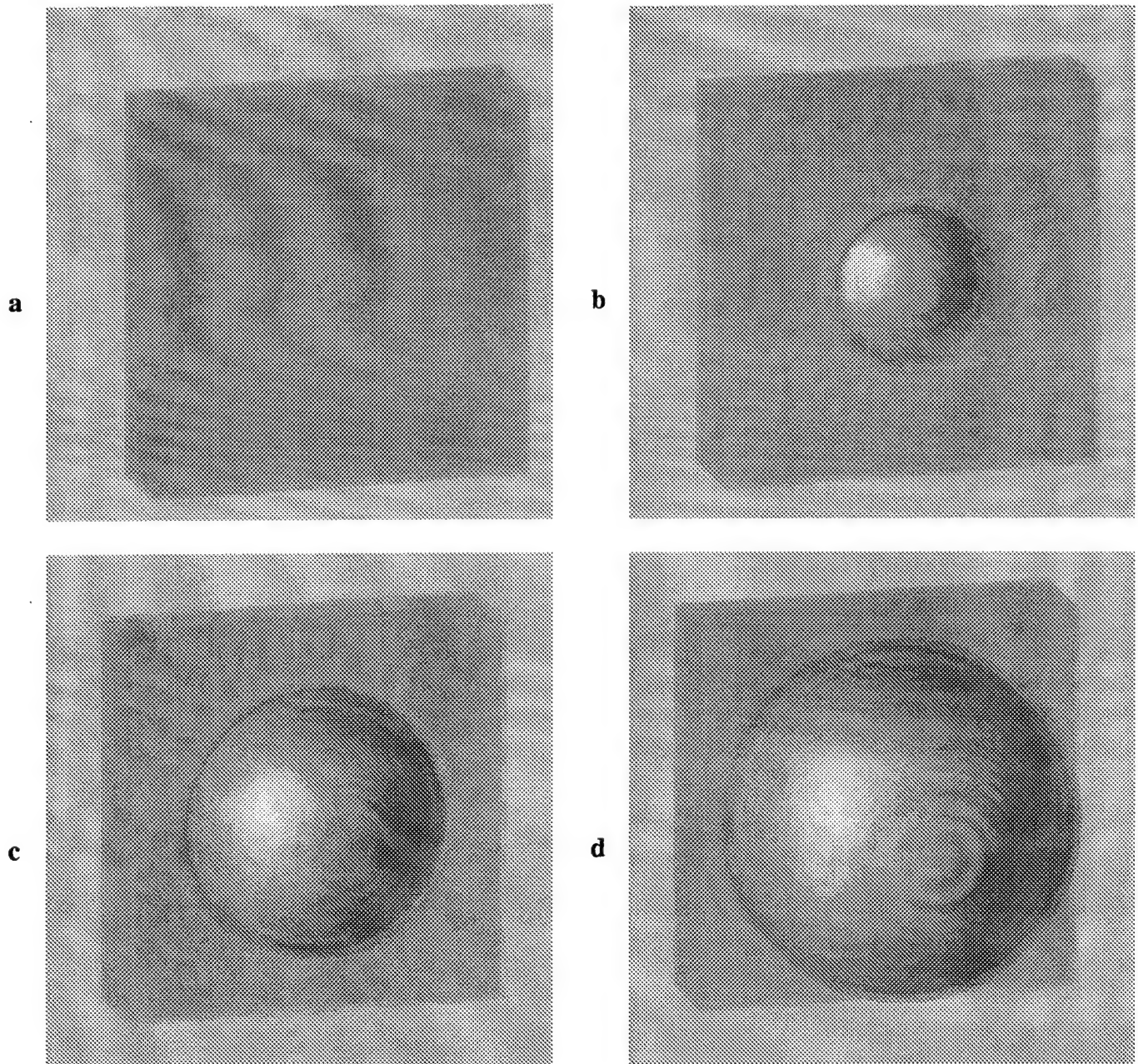


Figure 8: Isosurface renderings of the total (logarithmically scaled) pressure wavefield associated with scattering from a “muscle” sphere of radius 1.5 mm. Incident pulse parameters were the same as in Figs. 4–6. Panels (a)–(d) show the wavefield at four instants separated by $0.79 \mu\text{s}$. The view shown is such that the incident wave is traveling into the page, so that the visible wavefield includes the backscattered component. The lowest-amplitude isosurface shown is 67.5 dB down from the incident-wave amplitude. Each panel shows a rendering of the entire computational domain (10.66 mm on each side). In panel (a); the incident wavefront is just impinging on the sphere; in panel (d), the scattered wavefront has just passed the computational boundary.

Appendix F

Abstracts

1. "A new k -space method for simulation of ultrasonic propagation in tissue," presented at the 138th Meeting of the Acoustical Society of America (p. 88).
2. "Time-domain inverse scattering for quantitative ultrasonic mammography" (Technical Abstract), presented at the DoD Era of Hope Meeting (p. 89).
3. "Time-domain inverse scattering for quantitative ultrasonic mammography" (Lay/Public Abstract), presented at the DoD Era of Hope Meeting (p. 90).

Annual Report for DAMD17-98-1-8141, July 2000

Pages 88–90

2aBB6. A new k -space method for simulation of ultrasonic propagation in tissue. T. Douglas Mast (Appl. Res. Lab., Penn State Univ., University Park, PA 16802, mast@sabine.acs.psu.edu), D.-L. Donald Liu (Siemens Medical Systems, Issaquah, WA 98027), Laurent P. Souriau, Adrian I. Nachman, and Robert C. Waag (Univ. of Rochester, Rochester, NY 14642)

A new k -space method for large-scale computations of ultrasonic propagation is presented. In the new method, spatial derivatives from the second-order acoustic wave equation for inhomogeneous media are evaluated by Fourier transformation. Solutions are advanced in time using a k - t space Green's function. Computational results indicate that the new method shares advantages of both past k -space and pseudospectral methods. For scatterers with properties similar to soft tissue, the k -space method provides much higher accuracy and lower computational cost than a 2-4 finite-difference time domain method. The k -space method also allows high accuracy to be obtained for time steps much larger than those required by a leapfrog pseudospectral method. The low dispersion inherent to the k -space method is illustrated by large-scale quasi-one-dimensional computations, in which pulse waveforms incur negligible shape change for propagation distances as large as 1000 wavelengths. Example applications of the k -space method are demonstrated, including simulation of propagation through a large-scale tissue cross-sectional model and incorporation of a k -space solver into a nonlinear inverse scattering method employing eigenfunctions of the far-field scattering operator.

TIME-DOMAIN INVERSE SCATTERING FOR QUANTITATIVE ULTRASONIC MAMMOGRAPHY

T. Douglas Mast

Applied Research Laboratory
The Pennsylvania State University

mast@sabine.acs.psu.edu

A new method for ultrasonic mammography is presented. This method provides quantitative tomographic images of inhomogeneous tissue using time-domain scattering measurements made on a surrounding surface (for example, on a circle for images of a two-dimensional breast cross section). High-resolution, quantitative images of tissue are reconstructed using coherent combination of far-field scattered ultrasound waveforms, delayed and summed to focus at each image point. The focused image is a reconstruction of the spatially-dependent sound speed variation, and is equivalent to a wideband filtered backpropagation reconstruction weighted by the spectrum of the incident wave. The resulting images are higher in quality than frequency-domain quantitative reconstructions and contain more diagnostic information than conventional B-scans.

Rigorous testing of the new imaging method is carried out using simulated ultrasonic propagation through breast tissue. Breast tissue models are obtained both from segmentation of stained cross sections and from analysis of high-resolution three-dimensional data from the Visible Woman project. Computations of ultrasonic propagation are performed using a new k -space method, in which the spatial differential equations are solved by Fourier transformation and temporal iteration is performed using a k - t space propagator. Numerical results indicate that this method is highly accurate for large-scale soft-tissue computations, with much greater efficiency than that of competing methods. Thus, the k -space method is particularly appropriate for large-scale two-dimensional and three-dimensional computations of propagation through breast tissue.

Quantitative images, obtained using synthetic data for two-dimensional and three-dimensional scattering of wideband pulses as well as measured scattering data from a 2048-element ring transducer, confirm that the time-domain reconstruction method provides superior image quality for objects of size and contrast relevant to ultrasonic mammography. The new method can also be extended to incorporate available image-enhancement techniques, such as time-gain compensation to correct for medium absorption and aberration correction methods to reduce error associated with weak scattering approximations.

The US Army Medical Research and Materiel Command under DAMD17-98-1-8141 supported this work.

TIME-DOMAIN INVERSE SCATTERING FOR QUANTITATIVE ULTRASONIC MAMMOGRAPHY

T. Douglas Mast

Applied Research Laboratory
The Pennsylvania State University

New methods for breast cancer detection and characterization are the focus of this project, supported by the US Army Medical Research and Materiel Command. Major goals are to establish a new high-resolution, quantitative ultrasonic imaging method and to test this method using simulated propagation of ultrasonic pulses through accurately detailed breast tissue models.

Detailed breast tissue models have been obtained both from stained breast cross sections and from analysis of high-resolution three-dimensional data from the Visible Woman project. To accurately compute ultrasonic propagation through these tissue models, a new k -space method for ultrasound simulation has been developed. The k -space method is more accurate, more efficient, and requires less storage than alternative methods, and is thus ideal for computation of large-scale 2D and 3D ultrasonic propagation in breast tissue.

A new time-domain ultrasonic mammography method provides quantitative images of inhomogeneous media including breast tissue. High-resolution maps of the tissue sound speed are obtained from processing of measured ultrasonic scattering. Unlike previous frequency-domain inverse scattering methods, the entire signal bandwidth is used, so that reconstructed images have higher point resolution (ability to detect small structures such as microcalcifications) and contrast resolution (ability to distinguish subtle differences between tissue structures). The new method employs a straightforward time-domain reconstruction algorithm, similar to synthetic-aperture methods used by current clinical scanners, but provides much more diagnostic information than current B-scan devices. The high efficiency of the reconstruction algorithm makes the new method particularly well-suited for three-dimensional quantitative ultrasonic mammography.

Quantitative images, obtained both from synthetic and measured ultrasound data, confirm that the new imaging method provides superior image quality and accurate quantitative information. After further development and clinical implementation, the new ultrasonic mammography method is expected to become competitive with magnetic resonance imaging and x-ray computed tomography as a tool for breast cancer detection and characterization, while maintaining inherent advantages of ultrasound such as lower cost, ability to characterize cystic and solid lesions, and safe, nonionizing radiation.

Appendix G

Curriculum Vitae

T. Douglas Mast

Principal Investigator

Annual Report for DAMD17-98-1-8141, July 1999

Pages 92-94

T. Douglas Mast

**Research Associate and Assistant Professor of Acoustics, Applied Research Laboratory,
The Pennsylvania State University, P.O.B. 30, State College, PA 16804
(814) 863-9998 (tel.), (814) 863-9918 (fax), mast@sabine.acs.psu.edu**

Technical Expertise

Physical acoustics, ultrasonic imaging, wave propagation and scattering in inhomogeneous media, inverse scattering, flow/sound interaction, bioacoustics, nondestructive evaluation.

Education

Ph.D. in Acoustics, The Pennsylvania State University, 1993. Thesis: *Physical Theory of Narrow-Band Sounds Associated with Aneurysms*. Advisor: Allan D. Pierce. GPA: 3.93/4.0.

Certificate (comparable to B.A.) in Music, The Naropa Institute, 1988.

B.A. in Physics and Mathematics, Goshen College, 1987. GPA: 3.89/4.0.

Present and Recent Employment

Research Associate and Assistant Professor of Acoustics, Applied Research Laboratory, The Pennsylvania State University, 1999–present.

Research Associate, Applied Research Laboratory, The Pennsylvania State University, 1997–1999.

Postdoctoral Scholar, Applied Research Laboratory, The Pennsylvania State University, 1996–1997.

Postdoctoral Fellow, Ultrasound Research Laboratory, University of Rochester, 1993–1996.

Research Asst., Graduate Program in Acoustics, Pennsylvania State University, 1988–1993.

Research Asst., Turner Laboratory of Precision X-Ray Measurements, Goshen College, 1986–1987.

Teaching Asst., Department of Physics, Goshen College, 1985–1987.

Honors, Awards and Society Affiliations

President, Central Pennsylvania Chapter of the Acoustical Society of America, 1999–2000.

Vice President, Central Pennsylvania Chapter of the Acoustical Society of America, 1998–1999.

Listed in *Who's Who in Science and Engineering*.

Kenneth E. Simowitz Memorial Award, The Pennsylvania State University, 1996.

F. V. Hunt Fellowship, Acoustical Society of America, 1994–1995.

Kenneth E. Simowitz Memorial Citation, The Pennsylvania State University, 1992.

General Electric Teaching Incentive Loan, 1990.

Turner Laboratory Fellowship, Goshen College, 1986.

Member of Acoustical Society of America.

Member of American Institute of Ultrasound in Medicine.

Member of Institute of Electrical and Electronics Engineers (Ultrasonics, Ferroelectrics, and Frequency Control Society).

Scientific Publications

- Mast, T. D., Lin, F., and Waag, R. C., "Time-domain ultrasound diffraction tomography," *1999 IEEE Ultrasonics Symposium Proceedings*, Vol. 2, pp. 1617-1620.
- Mould, J. C. Wojcik, G. L., Carcione, L. M., Tabei, M., Mast, T. D., and Waag, R. C., "Validation of FFT-based algorithms for large-scale modeling of wave propagation in tissue," *1999 IEEE Ultrasonics Symposium Proceedings*, Vol. 2, pp. 1551-1556.
- Mast, T. D. and Gordon, G. A., "Quantitative flaw reconstruction from ultrasonic surface wavefields measured by electronic speckle pattern interferometry," submitted to *IEEE Trans. Ultrason. Ferroelect. Freq. Control* (1999).
- Souriau, L. P., Mast, T. D., Liu, D.-L. D., Nachman, A. I., and Waag, R. C., "A new k -space method for large-scale models of wave propagation in tissue," to appear in *IEEE Trans. Ultrason. Ferroelect. Freq. Control* (2000).
- Mast, T. D., Swanson, D. C., Mahon, M. P. and Norris, D. E., "Resolution of multipath outdoor sound propagation using spread spectrum signals," submitted to *J. Acoust. Soc. Am.* (1998).
- Mast, T. D., "Wideband quantitative ultrasonic imaging by time-domain diffraction tomography," *J. Acoust. Soc. Am.* **106**, 3061-3071 (1999).
- Mast, T. D., Hinkelman, L. M., Metlay, L. A., Orr, M. J., and Waag, R. C., "Simulation of ultrasonic pulse propagation, distortion, and attenuation in the human chest wall," *J. Acoust. Soc. Am.* **106**, 3665-3677 (1999).
- Gordon, G. A. and Mast, T. D., "Wide-area imaging of ultrasonic Lamb wave fields by electronic speckle pattern interferometry," *Proc. SPIE* **3586**, 297-309 (1999).
- Myers, L. F., Lovette, M., Kilgus, C. C., Giannini, J. A., Swanson, D. C., Reichard, K. M., Mahon, M. P., and Mast, T. D., "Java-based information system for wayside sensing and control," *Proceedings of the IEEE/ASME Joint Railroad Conference*, 135-147 (1998).
- Hinkelman, L. M., Mast, T. D., Metlay, L. A., and Waag, R. C., "The effect of abdominal wall morphology on ultrasonic pulse distortion. Part I: Measurements," *J. Acoust. Soc. Am.* **104**, 3635-3649 (1998).
- Mast, T. D., Hinkelman, L. M., Orr, M. J., and Waag, R. C., "The effect of abdominal wall morphology on ultrasonic pulse distortion. Part II: Simulations," *J. Acoust. Soc. Am.* **104**, 3650-3664 (1998).
- Mast, T. D., Hinkelman, L. M., Orr, M. J., Sparrow, V. W., and Waag, R. C., Erratum: "Simulation of ultrasonic pulse propagation through the abdominal wall," [*J. Acoust. Soc. Am.* **102**, 1177-1190 (1997)], *J. Acoust. Soc. Am.* **104**, 1124-1125 (1998).
- Jansson, T. T., Mast T. D., and Waag, R. C., "Measurements of differential scattering cross-section using a ring transducer," *J. Acoust. Soc. Am.* **103**, 3169-3179 (1998).
- Mast, T. D., Nachman, A. I., Liu, D.-L., and Waag, R. C., "Quantitative imaging with eigenfunctions of the scattering operator," *1997 IEEE Ultrasonics Symposium Proceedings*, Vol. 2, pp. 1507-1510.
- Hinkelman, L. M., Mast, T. D., Orr, M. J., and Waag, R. C., "Effects of abdominal wall morphology on ultrasonic pulses," *1997 IEEE Ultrasonics Symposium Proceedings*, Vol. 2, pp. 1493-1496.
- Mast, T. D., Nachman, A. I., and Waag, R. C., "Focusing and imaging using eigenfunctions of the scattering operator," *J. Acoust. Soc. Am.* **102**, 715-725 (1997).

Mast, T. D., Hinkelman, L. M., Orr, M. J., Sparrow, V. W., and Waag, R. C., "Simulation of ultrasonic pulse propagation through the abdominal wall," *J. Acoust. Soc. Am.* **102**, 1177-1190 (1997).

Mast, T. D. and Waag, R. C., "Wave space resolution in ultrasonic scattering measurements," *J. Acoust. Soc. Am.* **98**, 3050-3058 (1995).

Mast, T. D. and Pierce, A. D., "A theory of aneurysm sounds," *J. Biomech.* **28**, 1045-1053 (1995).

Mast, T. D. and Pierce, A. D., "Describing-function theory for flow excitation of resonators," *J. Acoust. Soc. Am.* **97**, 163-172 (1995).

Mast, T. D., "Limit cycles of flow-excited resonators: a describing-function analysis," in *Structural Acoustics, Scattering, and Propagation: Theoretical and Computational Acoustics—Volume I*, Edited by J. E. Ffowcs Williams, D. Lee, and A. D. Pierce, (River Edge, New Jersey: World Scientific, 1994), pp. 389-403.

Mast, T. D. and Pierce, A. D., "Flow-induced sounds associated with aneurysms," in *Flow Noise Modeling, Measurement, and Control*, edited by T. M. Farabee, W. L. Keith, and R. M. Lueptow (New York: American Society of Mechanical Engineers, 1991), pp. 129-134.